OPTICAL TECHNIQUES FOR ANALYSIS OF PHARMACEUTICAL FORMULATIONS

by

Scott R. Griffin

A Dissertation

Submitted to the Faculty of Purdue University

In Partial Fulfillment of the Requirements for the degree of

Doctor of Philosophy

Department of Chemistry

West Lafayette, Indiana

May 2020

THE PURDUE UNIVERSITY GRADUATE SCHOOL

STATEMENT OF COMMITTEE APPROVAL

Dr. Garth Simpson, Chair

Department of Chemistry

Dr. Corey Thompson

Department of Chemistry

Dr. Julia Laskin

Department of Chemistry

Dr. Lynne Taylor

Department of Industrial and Physical Pharmacy

Approved by:

Dr. Christine Hrycyna

Dedicated to my parents.

Thank you for believing in me.

ACKNOWLEDGMENTS

I have been fortunate enough throughout my life to have been blessed with all of the love and support I have received from both family and friends. First and foremost I have to thank my parents for believing in me and encouraging me to work hard and achieve the goals I set for myself. Without their love and support I would, without a doubt, not be where I am today.

I would like to thank my wonderful teachers and professors who helped shape my love of science throughout my time in high school and college. My interest in the sciences and chemistry specifically started with my fantastic high school chemistry teacher, Mrs. Sharp, who made chemistry a joy to learn. I am thankful for my professors in college who continued to show the fun and interesting sides of chemistry and research.

I'd like to Dr. Demitrios Stamatis who was my mentor during two summers of interning, who helped me realize that I wanted to pursue a PhD. His advise and guidance to conduct research during my time as an intern was invaluable to me making my decision to go into analytical chemistry and to pursue a PhD.

I am grateful for my time working with Garth Simpson. He is the best advisor and boss I could have asked for during my time in graduate school. His enthusiasm for science and work ethic are contagious, and has helped me become a better scientist. I want to thank the previous group members of the Simpson Lab in particular, Paul Schmitt and Ximeng You Dow, for showing me what it is like to be a graduate student and helping me get through the transition to grad life. Casey Smith, James Ulcickas, Chen Li, Hilary Florian, Nita Takanti, and Alex Sherman have been great friends to me and we have shared many good times together throughout our time in the Simpson Lab. I would like to thank Greg Eakins and the rest of the AMY facility for enabling much of the work I have completed for my dissertation. Their help with 3D printing, electronics, and much more was a huge help.

TABLE OF CONTENTS

LIST OF FIGURES 7
LIST OF ABBREVIATIONS 10
ABSTRACT 11
CHAPTER 1. INTRODUCTION 12
1.1 Measurement challenges in the pharmaceutical industry 12
1.2 Nonlinear optical techniques for crystal detection 14
1.2.1 Second harmonic generation 14
1.2.2 Triboluminescence 15
1.3 Dissertation overview 16
CHAPTER 2. TRIBOLUMINESCENCE FROM PHARMACEUTICAL FORMULATIONS 19
2.1 Introduction 19
2.2 Experimental 21
2.3 Results and Discussion 23
2.4 Conclusions 28
CHAPTER 3. SLURRIES ANALYSIS USING TRIBOLUMINESCENCE 30
3.1 Introduction 30
3.2 Experimental Methods 32
3.3 Results and Discussion 33
3.4 Summary 35
3.5 Future Work 36
CHAPTER 4. ITERATIVE NON-NEGATIVE MATRIX FACTORIZATION FILTER FOR BLIND DECONVOLUTION IN PHOTON/ION COUNTING 37
4.1 Introduction 37
4.2 Methodology 40
4.2.1 Algorithm 43
Baseline Correction 44
Matrix Factorization 45
Initialization 45
Solving for the $\boldsymbol{dfit, i}$ Element of the $\boldsymbol{dfit}$ Vector 46

Solving for the IRF 46
Iterate to Convergence 46
Autocorrelation 46
4.3 Experimental 47
4.4 Results and Discussion 49
4.5 Conclusions 55
CHAPTER 5. SINGLE PARTICLE GROWTH RATE DISTRIBUTIONS BY IN SITU SINGLE PARTICLE TRACKING 57
5.1 Introduction 57
5.2 Experimental Methods 59
5.3 Results and Discussion 61
5.4 Conclusions 68
CHAPTER 6. DISPARITIES IN CRYSTAL GROWTH AND NUCLEATION KINETICS IN EXPOSED VERSUS BURIED CRYSTALS 70
6.1 Introduction (need to fix citations) 70
6.2 Methods 74
6.3 Results and Discussion 75
6.4 Conclusions 80
CHAPTER 7. HIGH THROUGHPUT IN SITU STABILITY TESTING 82
7.1 Introduction 82
7.2 Experimental Methods 84
7.3 Results and Discussion 86
7.4 Summary 88
7.5 Future Work 88
REFERENCES 89
VITA 97

LIST OF FIGURES

Figure 1.1. Illustration of the drug product pipeline. 12

Figure 1.2. The biopharmaceutics classification system of drugs. 13

Figure 1.3. Jablonski diagram for SHG. 15

Figure 2.1 A schematic depiction of the TL instrument. 21

Figure 2.2. A) Representative trace from a 0.05% by weight griseo-fulvin sample. B) 11 impact events concatenated togeth-er into a single graph are shown to illustrate the shot to shot variability. The green (lower), offset data trace is pure PEG, shown to demonstrate the baseline response in the absence of crystalline griseofulvin. 23

Figure 2.3. Average integrated signal for 4 different particle sizes of sucrose crystals. The error bars represent the standard deviation of the mean slide value. 26

Figure 2.4. A) Shows the SHG (blue, horizontal lines) and TL (red, verti-cal lines) signals from two polymorphic forms of clopidogrel bisulphate, which are indistinguishable by bright field imaging. Both data sets were normalized to Form I. Both the Form II and the PEG data were rescaled by 100 to allow meaningful comparisons with the Form I results. B) Two representative images from SHG microscopy to demonstrate the difference in image contrast. The SHG results for Form II are rescaled by 5, showing only diffuse, low signal to noise, SHG signal. The bright punctum in the Form II image is attributed to an impurity and was excluded in the analysis 27

Figure 2.5. A) Shows the crystallinity content of the griseofulvin and HPMC-AS ASD after being exposed to heat and constant humidity for 48 hours. B) The upper trace (blue) shows the TL signal from the stressed sample while the lower trace (green) shows the signal from the unstressed sample, offset for clarity 28

Figure 3.1. A schematic depiction of the TL instrumentation with a flow cell and piston 32

Figure 3.2. Representative images of 100 concatenated piston fires summing to a total digitized time of 1 second. A) is the result from using a 0.4 mg/mL samples and B) is the result from using a 0.1 mg/mL sample. 33

Figure 3.3. Calibration curve using known concentrations of griseofulvin in water. 34

Figure 3.4. Representative images of 500 nm $BaTiO_3$ in water in a flow cell using 50 mW laser power and ~500 μs exposure. 35

Figure 4.1. Illustration of the NMF-F algorithm 42

Figure 4.2. An example of the NMF-F algorithm working on a smaller subset of the entire data trace to recover a photon event at position *i*. 45

Figure 4.3. Example signal transient pulled from a larger set of TL measurements which illustrate the complexity and difficulty in distinguishing individual photon events. Transients on a μs time scale appear as impulses over the ms time scale of the emission even 49

Figure 4.4. Using simulated data zoomed in to microsecond time scales and normalized results for ease of comparison with the ground truth. (a) The recovered transient (blue-top) compared to the original simulated transient (black-bottom), where the black trace is displayed with negative amplitude for ease of comparison. (b) The ground truth (black-top, offset by 1 Norm.U.), recovered (blue dashed, offset by 0.5 Norm.U.), and initial guess (red-bottom) IRFs are compared and show good agreement. (c) The recovered photon events (blue-top) are compared with the ground truth events (black-bottom) and show nearly complete recovery with minimal error. The digital filter's accuracy and ability to recover photons in high density data is highlighted in (d), by the ROC plots made with the same data and analyzed using NMF-F (blue), Wiener deconvolution (black), and BRL (red). Both the Wiener deconvolution and BRL were performed using the true IRF, while the NMF-F analysis was performed with a good guess from previous experiments. The AUC for NMF-F is 0.987 and 0.998 for the Wiener deconvolution. While the NMF-F performed better at lower false positive rates, it performs worse as the false positive rate increases. 51

Figure 4.5. An example of the algorithm's ability to recover an IRF similar to the ground truth. (a) Representative initial random guess used in the NMF-F and the BRL algorithm. (b) Recovered IRFs for the NMF-F (blue-middle) and BRL (red-bottom) algorithms are compared with the ground truth (black-top), which are offset for ease of comparison. (c) Bar chart highlighting the difference in ability to recover an IRF similar to the ground truth of the NMF-F and BRL algorithms. NMF-F converged to a similar IRF to the ground truth 82.5% of 1000 attempts, while BRL failed in all attempts. 52

Figure 4.6. Same TL signal transient from Figure 4.3 (black-upper) with the recovered photon events (blue-lower). The inset illustrates how many photons are within the initial rise caused by a TL burst event. 53

Figure 4.7. Amorphous solid dispersion of griseofulvin in HPMCAS stressed to induce crystallinity (black trace-upper) and the recovered photon events (blue trace-lower). 53

Figure 4.8. Results of autocorrelation on the raw TL data (red-top), the deconvolved photon events (green-bottom), and the measured IRF (blue-middle), where the *x*-axis is on a log scale. 54

Figure 5.1. (A,B) CEiST design, (C) IR thermal image of CEiST for validation of set temperature at 40^{O}C. 60

Figure 5.2. SHG images for time-dependent crystal growth of 15% HME ritonavir in (A) standard chamber, and in (B) CEiST. (C) The plot for average particle areas shows good agreement between the two different methods. 62

Figure 5.3. Time dependent SHG micrographs of 15% ritonavir ASDs stressed in CEiST at 50^{O}C/75%RH. 63

Figure 5.4. Individual crystal growth distribution in the CEiST for (A) HME with surfactant, (B) SDD with surfactant, (C) HME without surfactant, and (D) SDD without surfactant. Each plot has 20 different crystals tracked along the entire time trace and selected from different FOVs. The inset in each plot shows the dispersion in growth rates with the average growth rates shown in each plot as dashed line. 64

Figure 5.5. Average nucleation rates and single FoV trajectories in the CEiST for (A) HME with surfactant, (B) SDD with surfactant, (C) HME without surfactant, and (D) SDD without surfactant. 65

Figure 5.6. In a), the anticipated signal to noise ratio of nucleation rate for *in situ* vs conventional stability testing based on the Poisson statistics of crystal counting. I: nucleation rate, σ: uncertainty of nucleation rate based on Poisson statistics, N_t: number of crystals at time t. In b) A comparison between the results from a standard chamber and the CEiST. The different FOV represents the standard chamber where 4 time points were taken from 4 different repititions of the same experiment, and the single FOV is from a single experiment in the CEiST. 66

Figure 6.1. Images over time of seeded crystals pressed within bulk pharmaceutical formulation and seeded crystals on top of pressed pharmaceutical formulation. 76

Figure 6.2. Individual crystal growth distributions for A) Single crystals on the surface, B) radiating crystal growth on the surface, C) bulk crystal growth, and D) crystals in a low RH environment. Each plot has 14+ different crystals selected from different fields of view, and the inset in each plot shows the crystal growth rate distributions with the average shown as a dashed line..... 77

Figure 6.3. Illustration of the geometric effects on diffusion limited crystal growth. 79

Figure 7.1. Illustration of the TRHA platform. 84

Figure 7.2. Infrared image of the TRHA. 85

Figure 7.3. Preliminary data collected using the TRHA and model ritonavir containing ASD samples stressed at 75% RH in all wells and using the temperature profile from Figure 7.2. Each image is an extended focus image made by adding multiple z-plane images together. The left side of the images is the hot side and the right is the cool side. The bottom left corner of the images corresponds to the opening where the heat cartridge is inserted into the TRHA. A) Shows the initial time point of the accelerated stability test and the signal observed is expected to be contaminants from sample preparation or residual crystallinity within the ASD. B) Shows the TRHA after 12 hours at elevated conditions. C) Shows the TRHA after 48 hours at elevated conditions. 87

LIST OF ABBREVIATIONS

API	Active Pharmaceutical Ingredient
ASD	Amorphous Solid Dispersion
BCS	Biopharmaceutics Classification System
CEiST	Controlled Environment for *in situ* Stability Testing
DSC	Differential Scanning Calorimetry
FDA	Food and Drug Administration
FTIR	Fourier Transform Infrared
HME	Hot Melt Extrusion
HPMC-AS	Hydroxypropyl Methylcellulose Acetyl Succinate
IR	Infrared
NMF	Non-Negative Matrix Factorization
NMF-F	Non-Negative Matrix Factorization Filter
PEG	Polyethylene Glycol
PLM	Polarized Light Microscopy
ppm	Parts per Million
ppt	Parts per Trillion
PVP	Polyvinyl Pyrrolidone
PXRD	Powder X-Ray Diffraction
RH	Relative Humidity
SDD	Spray Dried Dispersion
SHG	Second Harmonic Generation
SONICC	Second Order Nonlinear Imaging of Chiral Crystals
ssNMR	Solid State Nuclear Magnetic Resosnance
TL	Triboluminescence
TRHA	Temperature and Relative Humidity Array

ABSTRACT

The symmetry requirements of both second harmonic generation (SHG) and triboluminescence (TL) provide outstanding selectivity to noncentrosymmetric crystals, leading to high signal to noise measurements of crystal growth and nucleation of active pharmaceutical ingredients (API) within amorphous solid dispersions (ASD) during accelerated stability testing. ASD formulations are becoming increasingly popular in the pharmaceutical industry due to their ability to address challenges associated with APIs that suffer from poor dissolution kinetics and low bioavailability as a result of low aqueous solubility. ASDs kinetically trap APIs into an amorphous state by dispersing the API molecules within a polymer matrix. The amorphous state of the API leads to an increase in apparent solubility, faster dissolution kinetics, and an increase in bioavailability. Both SHG and TL are used to quantitatively and qualitatively detect the crystal growth and nucleation within ASD formulations at the parts per million (ppm) regime. TL is the emission of light upon mechanical disruption of a piezoelectrically active crystal. Instrumentation was developed to rapidly determine the qualitative presence of crystals within nominally amorphous pharmaceutical materials in both powders and slurries. SHG was coupled with a controlled environment for *in situ* stability testing (CEiST) to enable *in situ* accelerated stability testing of ASDs. Single particle tracking enabled by the CEiST measurements provided insights into crystal growth rate distributions present due to local differences within the material. Accelerated stability testing monitored by *in situ* measurements increased the signal to noise in recovered nucleation and crystal growth rates by suppressing the Poisson noise normally present within conventional accelerated stability tests. The disparities between crystal growth and nucleation kinetics on the surface versus within bulk material were also investigated by single particle tracking and *in situ* measurements. Crystals were found to grow faster in the bulk compared to single crystals growing on the surface while total crystallinity was found to be higher on the surface due to radial growth habits of crystals on the surface compared to columnar growth within the bulk. To increase the throughput of the *in situ* measurements, a temperature and relative humidity array (TRHA) was developed. The TRHA utilizes a temperature gradient and many individual liquid wells to enable the use of a multitude of different conditions at the same time which can reduce time required to inform formulations design of stability information.

CHAPTER 1. INTRODUCTION

1.1 Measurement challenges in the pharmaceutical industry

To bring a new drug product to market from discovery through clinical trials, a pharmaceutical company invests on average 11 years and $2.87 billion.[1] Figure 1.1 illustrates the

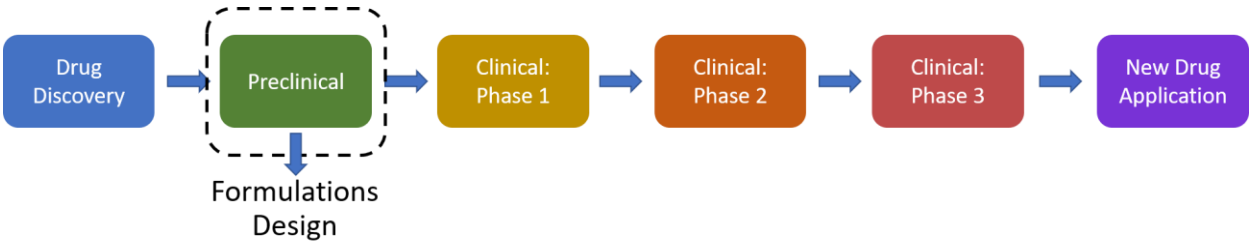

Figure 1.1. Illustration of the drug product pipeline.

overall drug product pipeline. The long timeframe and high cost are due in large part to the many steps within the process. The preclinical phase is on average responsible for roughly $450 million of out of pocket costs to the pharmaceutical company.[1] The use of advanced analytical techniques to solve crucial measurement challenges within the preclinical phase can reduce the time and cost associated with the design of effective formulations that can be used in clinical trials.

The most common dosage form for small molecule drug products is the oral dosage form, since patients can easily take the prescribed doses themselves without specialized training or equipment.[2] Two key factors in deciding bioavailability of an active pharmaceutical ingredient (API) used as a drug product are the aqueous solubility and permeability of its solid-state form. The widely known biopharmaceutics classification system (BCS)[3] uses these criteria to classify a potential drug candidate into one of four classes, shown in Figure 1.2. Class 1 drugs with high solubility and permeability correspond to an oral dosage form with desirable release within the body which leads to high bioavailability. As an API travels further down the BCS with lower permeability and aqueous solubility, it is less likely to be used in an oral dosage form.[4]

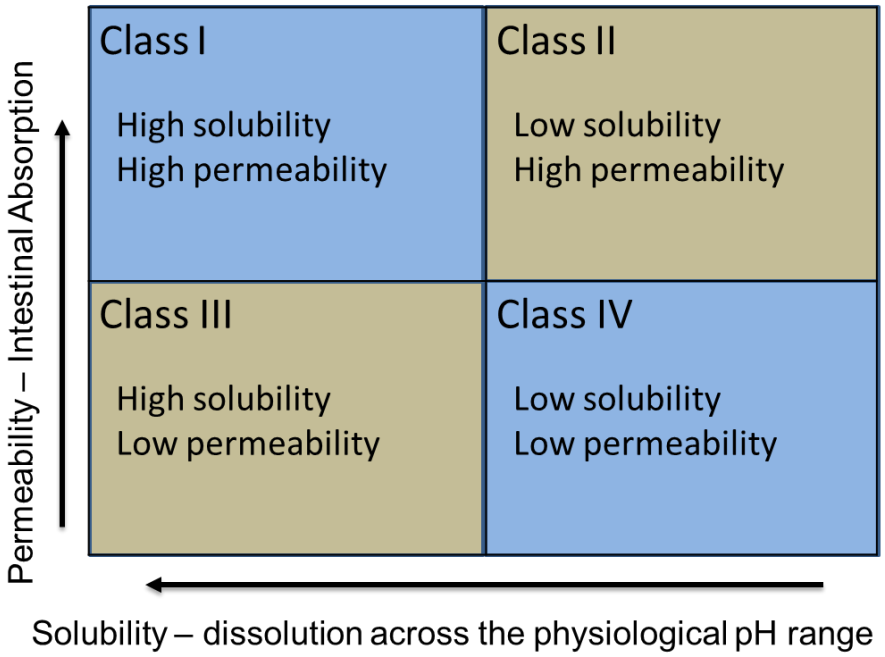

Figure 1.2. The biopharmaceutics classification system of drugs.

The desire within the pharmaceutical industry to produce more potent drug products with fewer side effects has led to an increase in molecular complexity and correspondingly lower aqueous solubility.[5] A recent study found that as much as 80% of new small molecules in the drug pipeline suffer from low aqueous solubility and fall into or near class II or IV within the BCS.[6] In order to address this issue, various formulation strategies have been explored, including co-crystal formulations[7-8], metastable crystal forms[9], and amorphous formulations[4]. Co-crystals provide an increase in dissolution kinetics for an increase in bioavailability, but it can be difficult and time-consuming to find an appropriate molecule to form a co-crystal with an API. Metastable crystal forms can provide a route to increased bioavailability, but suffer from stability concerns during manufacturing and storage by transitioning to more stable crystal forms with lower solubility. Amorphous formulations such as amorphous solid dispersions (ASD) have gained popularity for their ability to significantly increase apparent solubility and corresponding bioavailability.

In an ASD, the API is dispersed throughout a polymer carrier matrix that kinetically traps the API molecules in the amorphous state. Since the amorphous form will commonly reside in a metastable state due to the higher free energy relative to the more ordered crystalline form, there is a significant thermodynamic driving force to transform back into the crystalline state. The

factors affecting the stability of the API within the ASD include temperature, relative humidity (RH), preparation method, and preparation conditions.[10] The transformation of the API from the amorphous to crystalline state can profoundly affect the overall bioavailability of the ASD.[11] Consequently, it is important to be able to measure trace amounts of crystalline content to aid in the design of ASDs capable of preventing crystal formation or residual crystallinity from manufacturing.[12-13]

There are many analytical techniques used to measure crystallinity within the pharmaceutical industry. Polarized light microscopy (PLM)[14] is commonly used during stability studies to determine the presence of residual crystals as well as to determine crystal growth and nucleation kinetics. However, PLM is limited to optically transparent samples and can be severely limited in use within automated analysis by complications with occlusions, contaminants, and crystalline excipients. Powder X-ray diffraction (PXRD)[15-17] is arguably the "gold standard" trace crystal detection method within the pharmaceutical industry. PXRD is limited in its ability to quantify trace crystalline content and can be labor intensive for sample preparation and operation. Other common techniques includeRaman spectroscopy[18], Fourier transform infrared spectroscopy (FTIR),[19] and solid state nuclear magnetic resonance (ssNMR)[20]. Many of these techniques have detection limits of approximately1-5% (w/w percentage), which can be on the order of the entire drug loading in some formulations. For this reason, a technique with lower limits of detection is needed.

1.2 Nonlinear optical techniques for crystal detection

Nonlinear optics (NLO) has recently gained traction in the pharmaceutical industry for sensitive detection and quantification of trace crystalline content within amorphous formulations.[21-26] NLO imaging has the potential to provide the low limits of detection required to aid in the early detection of crystal nucleation and growth and detection of trace residual crystals within ASDs.

1.2.1 Second harmonic generation

Second harmonic generation (SHG) describes the coherent conversion of light to twice the frequency, as shown in Figure 1.3. Coherent SHG is symmetry-forbidden in centrosymmetric

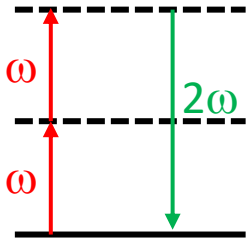

Figure 1.3. Jablonski diagram for SHG.

media but is allowed in materials with a lower degree of symmetry, including noncentrosymmetric crystals. The majority of APIs are chiral molecules which might crystallize into noncentrosymmetric space groups, meaning most are symmetry-allowed for SHG. SHG provides a near background free measurement of the crystalline fraction of an ASD as the amorphous material will produce no coherent SHG signalleading to detection limits as low as parts per trillion (ppt) for ideal conditions and parts per million (ppm) for routine measurements.[27] The low limits of detection of SHG microscopy enabled quantification of crystallization kinetics in ASDs spanning a four-order of magnitude range in crystallinity.[28-29]

Stability testing is routinely performed by pharmaceutical companies to meet the requirements that the food and drug administration (FDA) has imposed for the characterization of drug products.[30] In ASD formulations, stability tests are particularly important in understanding the crystal growth and nucleation kinetics that will govern the long-term stability and shelf life of the drug product. Stability tests can require months to years to complete, which can be costly to store material for that long. Accelerated stability tests are commonly used to speed up the process by elevating the temperature and RH conditions that the ASD is stressed under. With the four orders of magnitude measurement range of SHG, accelerated stability tests have the potential to be completed faster as well as to inform predictive modeling through increased information content.

1.2.2 Triboluminescence

Triboluminescence (TL) is the emission of light upon the mechanical disruption of a crystal lattice. This phenomenon is commonly seen by rubbing two quartz crystals together or biting down on a wintergreen Life Saver™ in a dark room. The common mechanism attributed to TL generation is the piezoelectric effect,[31-33] where charge across a piezoelectrically active crystal adiabatically accommodates slow changes in lattice deformation. During rapid deformation of the crystal lattice

(i.e. crystal fracturing), highly non-equilibrium charged states occur that can result in relaxation by dielectric breakdown of the surrounding atmosphere and subsequent arcing. The requirement for piezoelectricity gives TL a similar symmetry requirement to SHG, where noncentrosymmetry is required for piezoelectricity. However, a further limitation is present for TL; a permanent dipole within the crystal lattice is also required. Similar to SHG, these symmetry requirements make TL detection a highly selective measurement. TL detection of crystalline content within pharmaceutical materials has been shown to reach detection limits of 140 ppm.[34] While TL may not be as sensitive as SHG for crystal detection, TL still shows an order of magnitude lower detection limits compared to more common techniques such as PXRD, making TL an option for the qualitative detection of residual crystals within an ASD through the use of relatively simple instrumentation.

The usefulness of TL within the pharmaceutical industry has just begun to be explored. TL has shown promise in use within slurry samples which can be used in monitoring processes where crystal formation or disappearance is important. TL also has potential as a process analytical technique for process monitoring or quality control applications as well as determining the difference between crystal forms, depending on the presence of TL or the intensity of the TL signal.

1.3 Dissertation overview

The dissertation will focus on nonlinear optical techniques for the qualitative and quantitative detection of crystallinity within pharmaceutical formulations. For qualitative analysis, TL prototype instrumentation was developed and optimized.SHG microscopy was the main focus for quantitative analysis. TL was shown to be a sensitive and selective technique for the rapid determination of the presence of trace crystalline content within ASDs powders and slurries. A novel algorithm was developed to deconvolve information about the fundamental mechanism of TL from TL measurements. Custom-built devices were designed to increase the efficiency and information content from accelerated stability testing within a commercial SHG microscope by allowing for *in situ* measurements.

The contents of chapter 2 focus on the development of the TL instrumentation for use with powdered samples. The limits of detection were determined to be 140 ppm using a calibration curve of griseofulvin doped into polyethylene glycol (PEG). The effect of particle size was explored and TL relative signals were compared with SHG signals for polymorph discrimination.

A model ASD containing griseofulvin (20% w/w) and HPMCAS-MF (80% w/w) was analyzed using the TL instrument before and after stressing at 50 ^{o}C and 75% RH in order to show a potential application of the technique.

The focus of chapter 3 was on the development of flow cells for use in a commercial SHG microscope and TL instrumentation to detect trace crystalline content within slurry samples. Limits of detection were determined to be 0.20 ± 0.08 mg/mL using a calibration curve of griseofulvin in deionized water for the TL instrumentation. SHG imaging of slurry samples showed the potential for the technique to be used in dissolution testing without the need for aliquots of sample to be taken from a mother liquor.

Chapter 4 introduces a novel iterative non-negative factorization filter (NMF-F) for the deconvolution of photon events from complex signals. Conventional non-negative factorization (NMF) methods can be prohibited by large data sets due to memory and time requirements of the computer doing the computation. The NMF-F algorithm developed performs NMF on subsets of large data sets as a rolling filter, allowing for the blind deconvolution of photon events from the highly convoluted time traces obtained from the TLexperiments. Autocorrelation analysis of the deconvolved time traces provided the characteristic time scale of a TL event, which was comparable to the time scale of an arcing event, supporting the piezoelectric mechanism of TL.

Chapter 5 details the development of a chamber that controls temperature and RH of samples for *in situ* measurements during accelerated stability testing. The *in situ* measurements allow for single particle tracking as API crystals nucleate and grow during the test. Eliminating the need for conventional stability chambers and aliquots of sample for each measurement significantly increased the signal to noise ratio of recovered nucleation rates by suppressing the Poisson noise present when a new sample is imaged at each time point. Single particle tracking allowed for the measurement of a growth rate distribution on a per particle basis. The growth rate distribution is explained by local differences within the material.

Chapter 6 illustrates the differences of crystal growth and nucleation kinetics at surfaces versus within bulk material. *In situ* measurements support a crystal growth rate distribution at both the surface and within bulk material and allow for the direct comparison of individual crystal growth rates at the surface and in bulk. Crystals at the surface were found to grow slower than within bulk material which was explained through geometric effects where crystals surrounded by material have diffusion of the API molecules in twice the area than crystals on the surface. SHG

coupled with *in situ* measurements also allowed for the discovery of a bimodal growth rate distribution at the surface where it is suggested that two different crystal forms are present. It is also seen that the crystal growth habit is primarily radial at the surface, with a small subset of columnar due to a higher defect density in the crystals caused by the elevated RH leaving a thin water layer on the sample. Crystals within the bulk material showed a columnar growth habit.

Chapter 7 builds upon the *in situ* stability chamber developed in Chapter 5 by adding more sample wells and a temperature gradient across the device to support Arrhenius analysis in accelerated stability assessments for extrapolation to ambient conditions. The temperature gradient and increase in liquid wells on the device allows for a large range of conditions to be interrogated at the same time. The high throughput design of this new device has the potential for reducing the timeline for providing information to inform on formulations design.

CHAPTER 2. TRIBOLUMINESCENCE FROM PHARMACEUTICAL FORMULATIONS

Reprinted (adapted) with permission from Casey J. S.*, Scott R. G.*, Gregory S. E., Fengyuan D., Julia K. W., Satyanarayana T., Srividya R., Atanu S., Si-Wei Z., Julie N., Zhen L., Timothy R., Garth J. S., Triboluminescence from pharmaceutical formulations, *Analytical Chemistry* **2018** 90 (11), 6893-6898. (*equal contribution).

2.1 Introduction

The solid state form of an active pharmaceutical ingredient (API) can profoundly influence bioavailability and efficacy.[6, 35-36] The desire for more potent drugs with fewer negative side effects has driven the pharmaceutical industry towards APIs with greater molecular complexity, with a corresponding drop in aqueous solubility. A study published in 2011 estimated 80-90% of all new small molecules in the pharmaceutical pipeline suffer from poor aqueous solubility.[6] Drugs with low solubility in their crystalline form generally exhibit slow dissolution kinetics, with correspondingly low bioavailability. Several strategies have been adopted to address this problem, including co-crystal formulations[7-8], the use of metastable crystal forms with faster dissolution kinetics[9], and preparing the API in an amorphous solid dispersion (ASD)[4].

While co-crystals and meta-stable crystal forms have advantages in stability and processability, their use can still introduce complications. Metastable crystal forms suffer from the possibility of transitioning to the more stable, but typically less soluble, crystal form during manufacturing or storage. Alternatively, co-crystals generally do not suffer from the same stability issues since they are often in their most thermodynamically stable state. However, the difficulty of finding appropriate molecules to form co-crystals with APIs has prevented the widespread adoption of the technique.

Amorphous solid dispersions are gaining rapid acceptance and widespread use. An ASD is prepared by casting the amorphous API in a compatible polymer matrix. The polymer matrix typically maintains the amorphous API in a metastable glassy state prior to dissolution (e.g., in the GI tract for an oral formulation).[37] ASD formulations are metastable, in which crystallization is suppressed through kinetic rather than thermodynamic control.[37-38] As such, even trace residual crystallinity in ASDs can negatively impact bioavailability and shelf-life by removing kinetic

barriers for nucleation. The possibility of trace crystallinity impacting stability and dissociation leads to extensive stability testing of ASD dosage forms.

The most commonly used analytical techniques to quantify crystalline content within APIs and API formulations include the use of differential scanning calorimetry (DSC),[39-40] powder X-Ray diffractometry (PXRD),[15-17] spectrochemical techniques including Raman,[41-45] and solid state nuclear magnetic resonance (ssNMR).[20] Unfortunately, these methods have detection limits around 1-2% crystallinity under routine conditions, which can be particularly problematic when drug loadings are low within a formulation.

Recently, second harmonic generation (SHG) has been shown to rapidly quantify trace crystallinity within ASDs.[46] The symmetry requirements of SHG, in which coherent signal is only generated from noncentrosymmetric crystals, allows for a selective measurement with detection limits as low as parts per trillion under favorable conditions and routinely achieves ppm limits in powders.[28] Trace crystallinity measurements that take advantage of particle counting techniques enable quantification of trace crystallinity content with high statistical certainty.[21] SHG has been shown to exhibit limits of detection greater than 3 orders of magnitude lower than conventional benchtop methods. Advances in the advent of ultrafast fiber lasers have further improved access to affordable turn-key laser sources for SHG microscopy.[47-49] However, the expense and complexity of ultrafast optical methods complicates applications of SHG microscopy for routine and rapid on-line and at-line reaction monitoring. In addition, optical analysis of powders is often limited by a penetration depth on the order of the mean particle size,[21] potentially introducing sample bias if the crystallinity is heterogeneously distributed throughout the powder. Alternative methods based on simpler and more robust measurement platforms would facilitate on-line reaction monitoring and process analytical technologies (PAT).

In this work, impact driven triboluminescence (TL) enables rapid assessment of crystalline content within pharmaceutical powders. TL is the emission of light upon mechanical disruption of a crystal. The piezoelectric effect greatly enhances TL activity in crystals that are symmetry-allowed for piezoelectricity.[31] In conventional TL of piezoelectric materials, pressure to the point of fracturing is applied over a short time period. The rapid change in potential across the crystal results in a large transient current associated with the lattice displacement. For sufficiently large potential changes, plasma from dielectric breakdown can produce light emission in the form of TL. Evidence supporting dielectric breakdown as a mechanism for TL emission can be found in studies

demonstrating plasma-generated electron impact excitation of molecular N2 which is the most commonly seen line spectra associated with TL.[31-33] In the present study, the presence of TL is used as a sensitive and selective indicator for the presence of residual noncentrosymmetric crystals in model ASDs comprised of trace crystalline active pharmaceutical ingredients (APIs) cast within an amorphous polymer matrix. Given the close similarities in the symmetry properties of both piezoelectricity and SHG, TL arising from the piezoelectric mechanism is anticipated to exhibit similar selectivity for chiral API crystals in a much simpler measurement platform.

2.2 Experimental

Triboluminescence was induced in the powdered samples using mechanical force delivered from a solenoid as depicted in Figure 1. Light from TL was collected by a photomultiplier tube (PMT) and recorded with a digital oscilloscope card. The oscilloscope card was intentionally impedance mismatched with a 1MΩ input impedance to increase the voltage and the time-constant of single photon events. After each impact, the sample was translated to provide an unperturbed area for the next impact. Including sample translation time, each TL measurement took ~40s for 36 impact events.

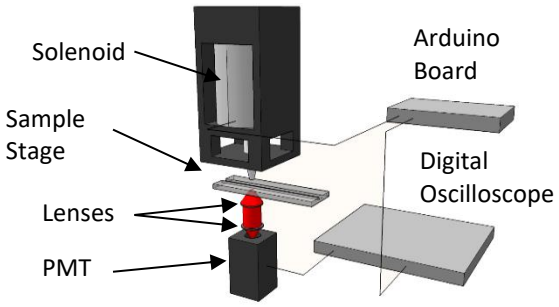

Figure 2.1 A schematic depiction of the TL instrument.

The energy imparted by the solenoid in a single impact was 0.5 Joules over a 7 mm2 area, this was calibrated based on the response obtained from striking a similarly prepared control slide with a brass weight dropped from different known heights. Characterization of the solenoid found that maximum force was applied when samples were located 1-2 mm above its maximum stroke length.

For consistency in density and packing, sample slides built to include a channel for powder packing were made from UVT Acrylic (Ted Pella, Inc.) and polystyrene microscope slides (Fisher Scientific, S67112A). Channel dimensions were 75 x 5 x 1 mm. A single slide allowed for 36 impact events without sample overlap. UVT acrylic slides were found to produce a negligible

background TL response. Additional information about the preparation of the slides can be found in supplemental information

Complementary second harmonic generation (SHG) microscopy results were performed using a SONICC microscope from Formulatrix (Bedford MA), modified in-house for powders analysis. Laser power was set to 150 mW at the sample (170 fs, 50 MHz) and the signal was integrated for 500 ms over 512×512 pixels in a 2.0 mm2 field of view. Modifications to the instrument as described previously allowed SHG to be collected back through the same objective used for delivery of the fundamental (i.e., in the epi direction) to facilitate measurements of powders.[50]

Samples for analysis were acquired and prepared according to the following procedures. Sucrose purchased from Sigma-Aldrich was ground with a mortar and pestle and then sieved to obtain 63-125 μm, 125-250 μm, 250-500 μm, and >500 μm diameter particle fractions. Polyethylene glycol (PEG), BioUltra 1,000, purchased from Fluka Analytical was ground with a mortar and pestle and then sieved to obtain 125-250 micron particles. Griseofulvin purchased from Sigma-Aldrich was sieved to isolate particle sizes between 63 μm and 125 μm, and physically mixed by stirring with appropriate amounts of the sieved PEG to make mixtures with concentrations of 10, 5, 2, 1, 0.5, 0.1, and 0.05% by weight. Mixtures were prepared by serial dilution and stirred for 2 minutes with a spatula between additions. Two different polymorphic forms of clopidogrel bisulphate were prepared in-house at Dr. Reddy's Laboratory (Hyderabad, India). Formulation protocols for clopidogrel bisulphate were followed to produce ~60 μm diameter spheroidal particles with a narrow size distribution. The polymorphs of clopidogrel bisulphate were identical in their preparation with the exception of a single step in the reaction, in which the Form II particles were controllably produced from the Form I particles through a polymorph transition.

To prepare the Griseofulvin HPMCAS-MF ASD samples, Griseofulvin was obtained from Sigma-Aldrich (St. Louis, MO), and HPMCAS-MF was purchased as AQOAT from Shin Etsu (Tokyo, Japan). The spray dry formulation comprised of Griseofulvin (20% w/w) and HPMCAS-MF (80% w/w). The solid components were dissolved in Acetone (4% w/v). The solution was spray dried on a 4M8-TriX spray dryer (ProCepT NV, Zelzate, Belgium) with a two-fluid nozzle diameter of 0.6 mm. The dried particles were carried by air into a cyclone and then into a collection vessel. Three processing rates were controlled and monitored: 1) solution feed rate, 2) processing

air flow rate, and 3) atomizing air flow rate. The processing air flow rate was set to be 0.40 m3/min. The atomization air and the solution feed flow rates were taken to be 3.0 L/min and 6 mL/min, respectively. The spray drying conditions were set to reach inlet temperature of 91 °C and outlet temperature of 50 °C. The cyclone differential pressure was set at 30 mbar and tangential air flow rate was chosen to be 0.1 m3/min while the cooling air was shut off. The spray dried products were further dried under vacuum at ambient temperature overnight. The Griseofulvin ASD was confirmed to be amorphous using PXRD following preparation. See SI Figure 2 for PXRD data.

2.3 Results and Discussion

Representative time-traces of the PMT sensor outputs during impact events are shown in Figure 2. A number of features are noteworthy. First, relatively long decay times arose from the intentional impedance mismatch of the PMT inputs to the oscilloscope cards to facilitate detection. Impedance matching resulted in transients from single-photon events only a few ns in duration and too short for digital capture at the sampling rates used. In addition, the time-traces do not correspond to a simple single-exponential decay impulsively initiated, but often present multiple peaks within a single impact event (Figure 2B). Multiple origins for the observations of distributions in emission times were considered: i) emission from multiple sources with slight differences in timing, ii) acoustic recurrences from reflection, and iii) multiple impacts from recoil

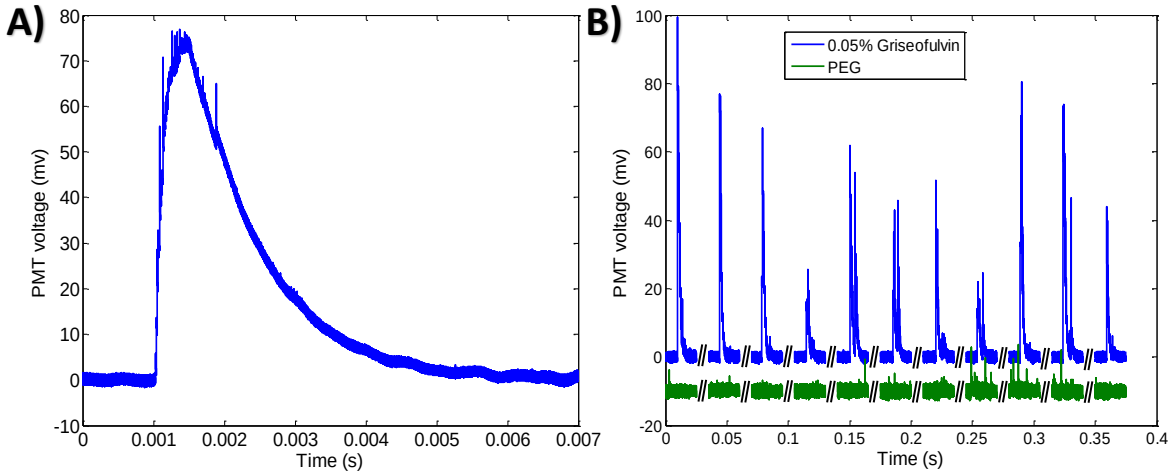

Figure 2.2. A) Representative trace from a 0.05% by weight griseo-fulvin sample. B) 11 impact events concatenated togeth-er into a single graph are shown to illustrate the shot to shot variability. The green (lower), offset data trace is pure PEG, shown to demonstrate the baseline response in the absence of crystalline griseofulvin.

of the impactor. Emission from multiple sources is consistent with the time for which the impactor translates through the powdered sample, 0.5 ms, determined by slow motion analysis of the impact event. Consideration of the speed of sound in the polyacrylic substrate of >2500 m/s[51] suggests a recurrence time of <400 ns, which was much shorter than the observations. The presence of multiple impacts from recoil and bouncing of the impacting piston were characterized by complementing the optical measurements with recordings of the acoustic response upon impact. These measurements revealed evidence for multiple collision events from recoil over the timeframe of the transients shown in Figure 2. Consequently, the temporal trends are tentatively attributed to the presence of multiple sources stochastically producing light emission at different time points during the primary impact event and the occasional presence of a secondary recoil hit.

A significant shot-to-shot variability in the emission intensity was observed in Figure 2B. Two sources of variance were considered: i) variability in impact force, and ii) variability in the number, sizes, and orientations of impacted crystals. Measurements performed to assess the first of the two possible sources were obtained by recording the variance in acoustic amplitude on a lead-zirconate titanate (PZT) piezoelectric transducer (not shown). In brief, the relative standard deviation in shot-to-shot acoustic amplitude upon impaction was 6%, which was significantly lower than the relative standard deviation in detected intensity of 53%. Consequently, the major source of shot-to-shot variance was attributed to the stochastic nature of the sample coupled with the limited volume (~7 mm2) of material sampled.

Calibration of the instrument was performed to provide an estimate of the limits of detection, shown in the supplemental information. All calibration measurements shown were acquired for powdered blends of crystalline griseofulvin in polyethylene glycol (PEG), chosen as a simple model for an amorphous solid dispersion. PEG was chosen as an amorphous substrate due to the considerable interest in it for use in ASDs.[52-54] Despite its semi crystalline nature, PEG was found to yield little to no detectable background as shown in Figure 2. The absence of significant background TL activity is consistent with the symmetry expectations of the measurements; centrosymmetric crystalline content does not support the piezoelectric response that drives the observed TL. Lower limits of detection (LoD) were found to be 140 ppm (calculation in supplementary information), with the low values arising primarily from the low background TL observed within the API-free polymer blanks.

The results from TL detecti on are compared with measurements probed by SHG microscopy, figure in supplementary information. The SHG results were produced by integrating the SHG intensity over a field of view of ~ 2 mm.2 Although significant improvements in the LoD by SHG have been reported by image analysis approaches[21, 27, 46], the integrated intensity provided the most direct side-by-side comparison with the TL results. The LoD for similarly prepared samples was found to be 17 ppm by SHG microscopy (calculation in supplementary information), which is roughly comparable to the LoD reported in previous measurements of the integrated SHG intensity of powdered blends.[21, 23, 25, 55-59] As in the case of TL, the low LoD of SHG in powdered samples arose primarily by the absence of significant background in the API-free blank samples. The higher limits of detection from TL are attributed to the presence of some weak TL emission from the pure polymer samples.

Based on previous reports suggesting several possible mechanisms underlying TL, a suite of studies was designed to assess the dominant contributions to the measurements of the model ASD. Two dominant mechanisms have emerged depending on the symmetry of the sample. The first mechanism considered is symmetry independent and is related to electroluminescence (EL). EL is understood to arise from the radiative recombination of electrons and holes, typically within a semiconductor or in localized trap states, caused by an applied current. In the case of TL, it has been conjectured that TL can also arise from electron-hole recombination, with the electrons and holes produced at defect sites upon lattice disruption. Evidence supporting this mechanism can be found from the large variety of materials capable of producing TL under ambient conditions and in vacuum, and from the similarities between the TL and EL spectra of some TL active crystals.[60] The second mechanism is selective to piezoelectric materials. In brief, the rapid mechanical action arising upon physical disruption of the crystal results in large and rapid lattice displacements. In piezoelectric materials, these displacements correspond to fast changes in capacitance, which if large enough, can produce electrical breakdown and plasma generation. While EL has been noted to contribute to the TL signal of some low band gap piezoelectric crystals (i.e., doped zinc sulfide),[61] crystals with a high band gap in the UV are expected to have little to no contribution from EL. Two separate sets of experiments were performed to assess the dominant mechanism underlying the observations of TL in the ASD model systems investigated in this study, with the results from the first set shown in Figure 3.

In Figure 2.3, the TL intensity significantly increased with increasing crystal size in sieved, powdered samples. The total volume and chemical composition of the material was identical in all the samples investigated in Figure 3, differing only in the crystal size distribution. The trends in the figure are in good qualitative agreement with the piezoelectric mechanism, as increases in crystal size correspond to increases in both the standing potential across the crystal (for dipolar materials, consistent with the P21 space group of sucrose used in Figure 2.3) and the capacitance from the increase in area. As such, TL is expected to increase monotonically with increases in crystal size, as the entire crystal contributes to the potential change from the rapid displacements associated with crystal collapse. In contrast, similar effects should not be expected in the strain-based mechanism that is independent of piezoelectricity. If the light-producing strain is highly localized relative to the size of the crystal, it is not clear that a change in crystal size would significantly impact the resulting light emission.

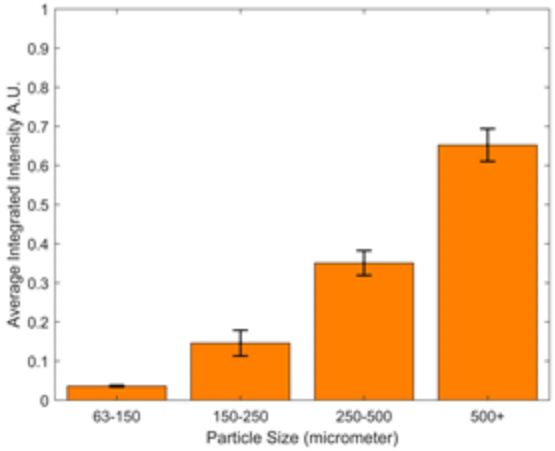

Figure 2.3. Average integrated signal for 4 different particle sizes of sucrose crystals. The error bars represent the standard deviation of the mean slide value.

In addition to the size-dependent studies, both TL and SHG microscopy measurements were performed on powders of two polymorphs of clopidogrel bisulphate with different anticipated piezoelectric properties to assess the role of crystal form. Form I and Form II of clopidogrel bisulphate have identical chemical composition, differing only in the packing arrangements within the lattice. The lower symmetry (P21) Form I particles produce significantly brighter SHG than the Form II (P212121) particles, generally consistent with expectations from previous quantum chemical calculations, which suggest brighter SHG with lower symmetry.[62] Because of the close

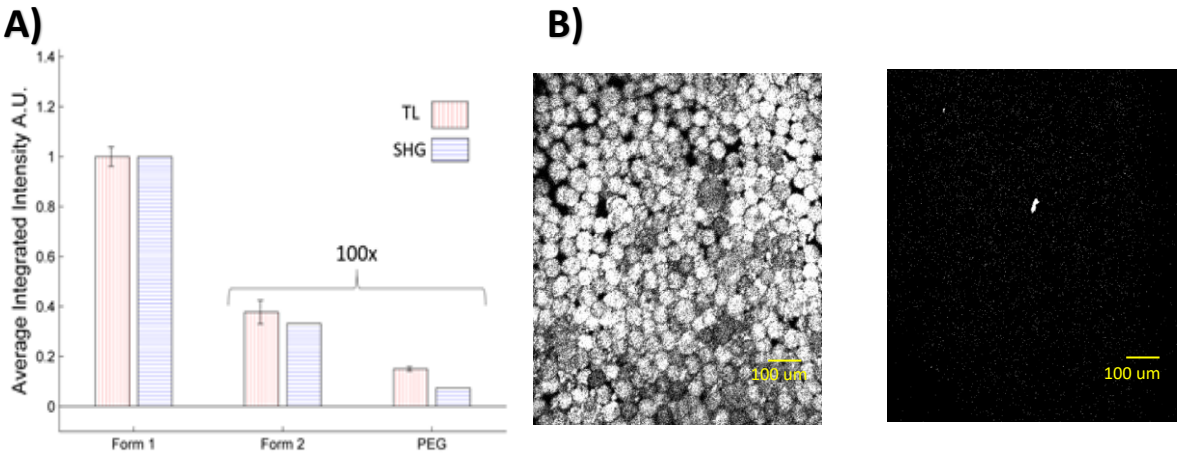

Figure 2.4. A) Shows the SHG (blue, horizontal lines) and TL (red, verti-cal lines) signals from two polymorphic forms of clopidogrel bisulphate, which are indistinguishable by bright field imag-ing. Both data sets were normalized to Form I. Both the Form II and the PEG data were rescaled by 100 to allow meaningful comparisons with the Form I results. B) Two representative images from SHG microscopy to demonstrate the difference in image contrast. The SHG results for Form II are rescaled by 5, showing only diffuse, low signal to noise, SHG signal. The bright punctum in the Form II image is attributed to an impurity and was excluded in the analysis.

symmetry similarities between SHG and piezoelectricity, it is reasonable to expect similar trends to arise in TL produced from the piezoelectric mechanism. In Figure 2.4, a comparison of the SHG and TL activities from the two powders differing only in crystal forms indicates close correlation between the SHG and TL, consistent with this expectation. The Form II and PEG signals were multiplied by 100 to show the difference in intensity between Form II and PEG. Overall, in combination with the size-dependent results, these measurements collectively suggest that the detected TL is dominated by piezoelectric contributions, which also explains the origins of the specificity to the chiral crystalline content based on the arguments in the Introduction.

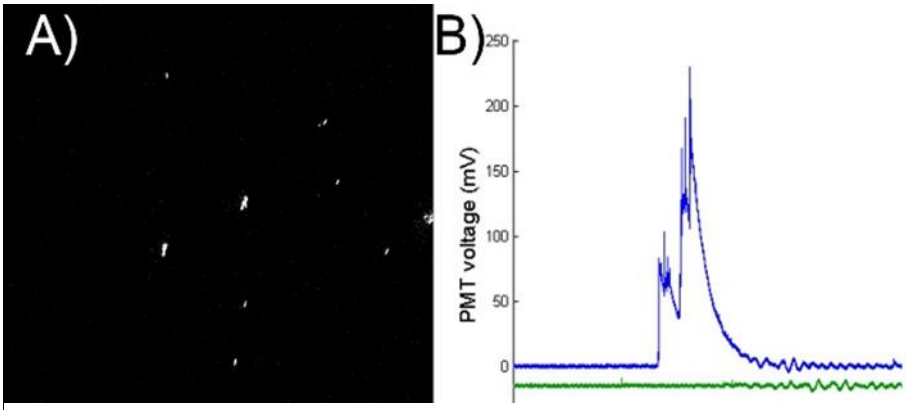

Figure 2.5. A) Shows the crystallinity content of the griseofulvin and HPMC-AS ASD after being exposed to heat and constant humidity for 48 hours. B) The upper trace (blue) shows the TL signal from the stressed sample while the lower trace (green) shows the signal from the unstressed sample, offset for clarity.

In order to evaluation the differences in the preparation procedures, additional experiments were performed for griseofulvin in HPMC-AS prepared as an ASD via spray drying. Figure 2.5A and 2.5B shows the SHG and TL signal of the prepared ASD as received from Merck. The ASD was found to be amorphous via PXRD, SHG, and TL. The spray dried ASD was heated at 65° C and constant humidity (used a saturated NaCl solution) for 48 hours at which point SHG and TL measurements were performed on the material. SHG image analysis allowed for quantitation of the crystalline content, which was determined to be 0.11%. TL analysis showed detectable signal with large shot-to-shot variability.

2.4 Conclusions

From these combined results, TL may be well-suited for rapid screening during on-line reaction monitoring of amorphous solid dispersions. In practice, ASD's are designed to contain only amorphous content, such that any residual trace crystallinity is generally considered disadvantageous. TL is able to detect low levels of crystallinity (140 ppm demonstrated in this work), making it appropriate for detecting crystallinity in nominally amorphous materials. While the large measurement variance from sample stochastics complicates quantitative powders analysis by TL as conceived herein, the high selectivity still suggests a role for outlier detection. In such cases, rapid measurements of TL signals greater than the background may serve as an

initial indicator for subsequent more detailed analysis (e.g., by SHG microscopy or spectrochemical characterization).

Triboluminescence has been shown to enable detection of crystallinity in amorphous solid dispersions with detection limits of 140 ppm. The speed of the measurements and simplicity of the instrument make it applicable to process analytical technologies. The crystal size and polymorphic form dependence of TL parallel SHG measurements and are both consistent with a mechanism dominated by the piezoelectric properties of the crystallites within the powder. The symmetry demands of piezoelectricity also underpin the origin of the selectivity of TL to the crystalline API fraction. The capabilities of TL suggest applications for outlier detection during process monitoring of amorphous solid dispersions. Studies are currently underway to characterize a diverse portfolio of different API and excipient materials to better assess the breadth applications that are potentially compatible with TL analyses.

CHAPTER 3. SLURRIES ANALYSIS USING TRIBOLUMINESCENCE

3.1 Introduction

Metastable pharmaceutical formulations are becoming increasingly common due to the trend of increasing size and molecular complexity of new drug molecules which consequently have low aqueous solubility in the crystalline state.[5] Amorphous solid dispersions (ASDs) are one formulation method that has gained popularity recently for the increase in apparent solubility and faster dissolution kinetics that it enables. An ASD kinetically traps the active pharmaceutical ingredient (API) in an amorphous state by dispersing the API into a polymer matrix. One mechanism of increased apparent solubility due to an ASD formulation is that as the polymer matrix dissolves in the gastrointestinal tract of the body, the API is essentially dragged into solution to create a supersaturated solution of the API that can then be absorbed into the body.[37] This mechanism works as long as the API doesn't crystalize before the formulation is taken by the patient or if the API crystallizes too quickly out of the supersaturated solution. The efficacy of an ASD is then directly related to the solid state form of the API which is typically in a metastable state within the ASD.[6, 35-36] Consequently, rigorous stability and dissolution testing is performed to characterize the crystal growth and nucleation kinetics and help provide a shelf life time for the formulation.

Common methods for measuring crystallinity within pharmaceutical materials are polarized light microscopy (PLM),[14] powder X-ray diffraction (PXRD),[15-17] infrared (IR) spectroscopy,[19] Raman spectroscopy,[18] and differential scanning calorimetry (DSC).[10, 63] PXRD is considered the "gold standard" for trace crystallinity determination of solids within the pharmaceutical industry but has challenges in its use on solids within a liquid. PLM is another common method used in stability tests but requires a stationary transparent sample. Most of these techniques also suffer from detection limits of around 1-5% crystallinity which could be on the order of the entire drug loading of an ASD.[64]

Nonlinear optical imaging is one technique which can address the limitations of the more common analytical methods. Second harmonic generation (SHG) describes the nonlinear scattering process of the coherent frequency doubling of light which is symmetry-forbidden in centrosymmetric media but allowed in assemblies of lower symmetry, including the large majority

of noncentrosymmetric crystals. Many pharmaceutically relevant molecules are chiral which might crystallize into noncentrosymmetric space groups. SHG can provide a near background free measurement of the crystalline fraction of an ASD since the amorphous material will not produce a coherent SHG signal. The downside to using SHG is the complexity and cost of the instrumentation, which requires a femtosecond laser and many optical components.

Triboluminescence (TL) is another technique which can provide lower limits of detection of the crystalline fraction of an ASD. TL is the emission of light upon rapid mechanical disruption of a crystal. The piezoelectric effect is commonly believed to be the driving force behind TL,[31-33] where the crystal is forced into non-equilibrium charge states as it is rapidly deformed upon fracture. These non-equilibrium charge states can lead to dielectric breakdown of the surrounding atmosphere and subsequent arcing between the surfaces of the fractured crystal. The symmetry requirements of a crystal to produce TL are similar to SHG since to produce the piezoelectric effect, a crystal is required to be noncentrosymmetric. Previous studies have shown TL to have detection limits as low as 140 ppm within powder samples.[65] This study utilizes the presence of TL to determine the presence of residual crystals within an ASD slurry to determine the point at which crystal growth occurs in dissolution experiments. A custom-built flow cell is coupled with the TL instrument described in more detail previously to introduce a slurry for analysis by TL. A similar flow cell is used for analogous SHG measurements of the same slurry for comparison. The use of a flow cell allows for continuous monitoring of the dissolution experiment as opposed to taking aliquots out for analysis.

3.2 Experimental Methods

TL was induced in slurry samples by a piston architecture coupled to a flow cell depicted in Figure 3.1. A photomultiplier card was used to collect the photons from the TL events caused

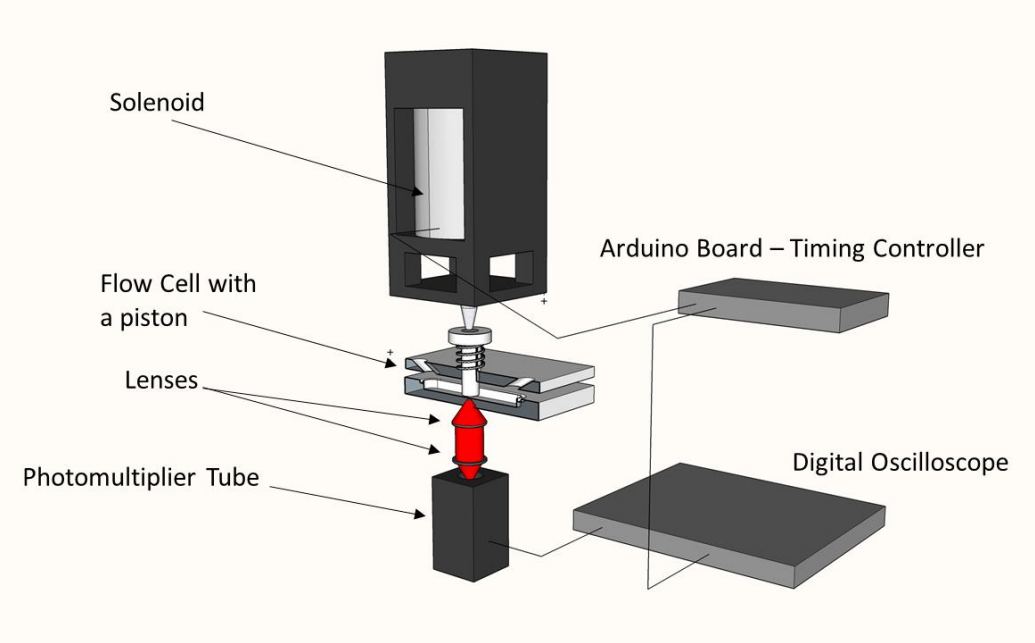

Figure 3.1. A schematic depiction of the TL instrumentation with a flow cell and piston.

by the piston impacting the crystals as they flow by. The signal was recorded on a digital oscilloscope card from Alazar Technologies Inc. The timing was controlled by an Arduino card to gate data collection to when the piston fires. The piston was controlled by a solenoid that was driven by custom electronics designed by the Jonathan Amy Facility at Purdue University.

All chemicals were obtained from Sigma Aldrich and used as received. Griseofulvin samples were prepared in 100 mL of deionized water and a weighed out amount of Griseofulvin mixed in. The sample was put on a magnetic stirrer and pumped through the flow cell by a peristaltic pump at a flow rate of about 3 mL per second leading to a fresh interrogated volume in a fraction of a second. The piston was fired once every second for the experiments over a completely new volume of the carrier liquid. The high flow rate was used in order to ensure the griseofulvin was pulled into the flow of the pump.

Complementary second harmonic generation (SHG) microscopy results were performed using a SONICC microscope from Formulatrix (Bedford MA), modified in-house for powders

analysis. The laser power was set to 50 mW at the sample (170 fs, 50 MHz) and the signal was integrated for 500 ms over 512×512 pixels in a 2.0 mm^2 field of view. Modifications to the instrument as described previously allowed SHG to be collected back through the same objective used for delivery of the fundamental (i.e., in the epi direction) to facilitate measurements of powders.[50] A flow cell similar to the cell used in the TL instrument butwithout the piston was installed into the SONICC instrument to allow for measurements of slurries. Similar conditions for the flow of the carrier liquid were used.

3.3 Results and Discussion

The TL instrument was characterized by running a calibration plot of known concentrations of griseofulvin within water. Representative time traces are shown in Figure 3.2. Each representative time trace is a concatenation of 100 fires of the piston. Figure 3.2A shows the results of 100 fires using a sample with aconcentration of 0.4 mg/mL, while Figure 3.2B shows a sample of 0.1 mg/mL. The calibration curve is shown in Figure 3.3, where each data point is the total

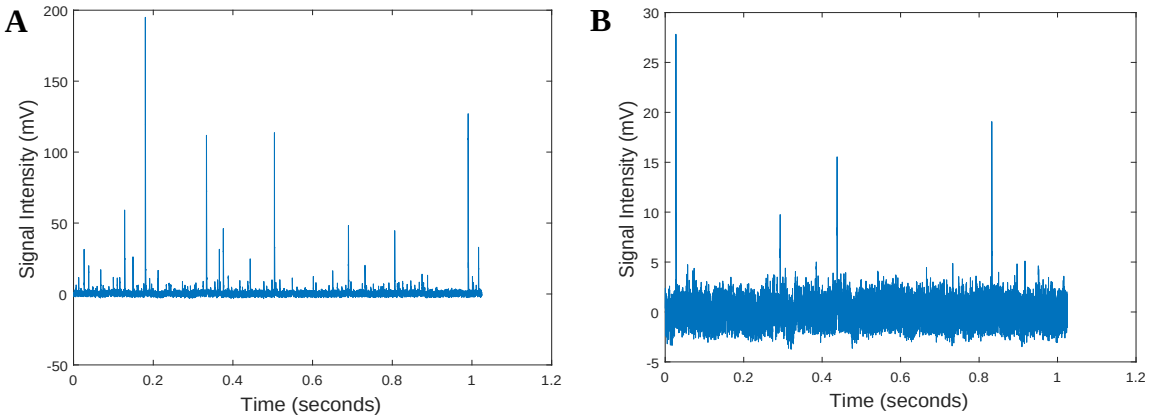

Figure 3.2. Representative images of 100 concatenated piston fires summing to a total digitized time of 1 second. A) is the result from using a 0.4 mg/mL samples and B) is the result from using a 0.1 mg/mL sample.

number of TL events that were calculated to be above the noise threshold. The noise threshold was determined by the maximum integrated value of 100 fires using only deionized water within the

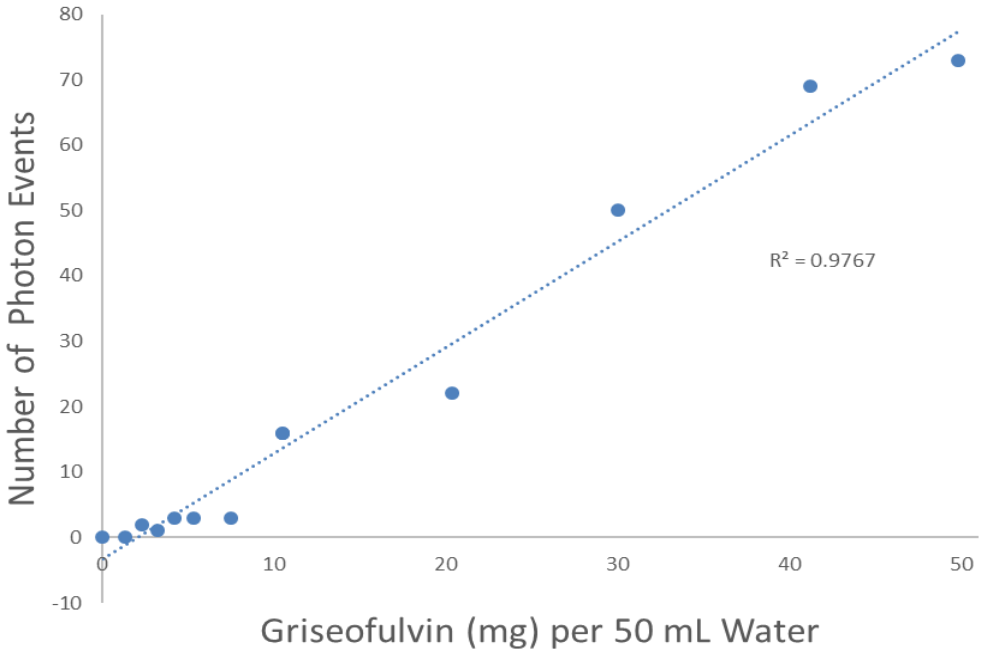

Figure 3.3. Calibration curve using known concentrations of griseofulvin in water.

flow cell. The lower limits of detection were determined to be 0.2 ± 0.08 mg/mL by using the calibration plot and the measured background signal in the absence of a sample.

The relatively high noise is due in large part to the stochastic nature of the measurement where fewer and fewer numbers of positive TL events can be seen at the lower concentration values. The higher limit of detection compared to the powder-based TL instrumentation is expected since the mechanism of TL is understood to be through dielectric breakdown of the surrounding atmosphere. In a slurry the crystal is surrounded by a liquid that is significantly harder to induce dielectric breakdown within, and is expected to quench the TL process.[60] It is more likely that the adsorbed nitrogen to the griseofulvin is what allows the TL process to occur even in a slurry.[66] There is a short amount of time where the crystal fracturing can produce TL before the water quenches the process. Past studies of TL within liquids have shown that using different liquids can quench the TL more quickly or slowly depending on the viscosity of the liquid.[60] One possibility to lower the detection limits of TL within slurries is to use more force in the piston to make sure crystals present are fractured and the potential for more photons to be released. Another possibility is to better collect the photons that are produced. Currently, the window in the flow cell is made of plexiglass, which has low transparency for UV wavelengths. It is expected that much

of the light given off from TL is from the N_2 spectra which has a significant portion in the near UV. It is difficult to obtain a durable material with significantly higher UV transmission properties.

Representative images from the SHG measurements are shown in Figure 3.4. The sample used was 500 nm $BaTiO_3$ particles in water with an unknown concentration of the $BaTiO_3$ as these

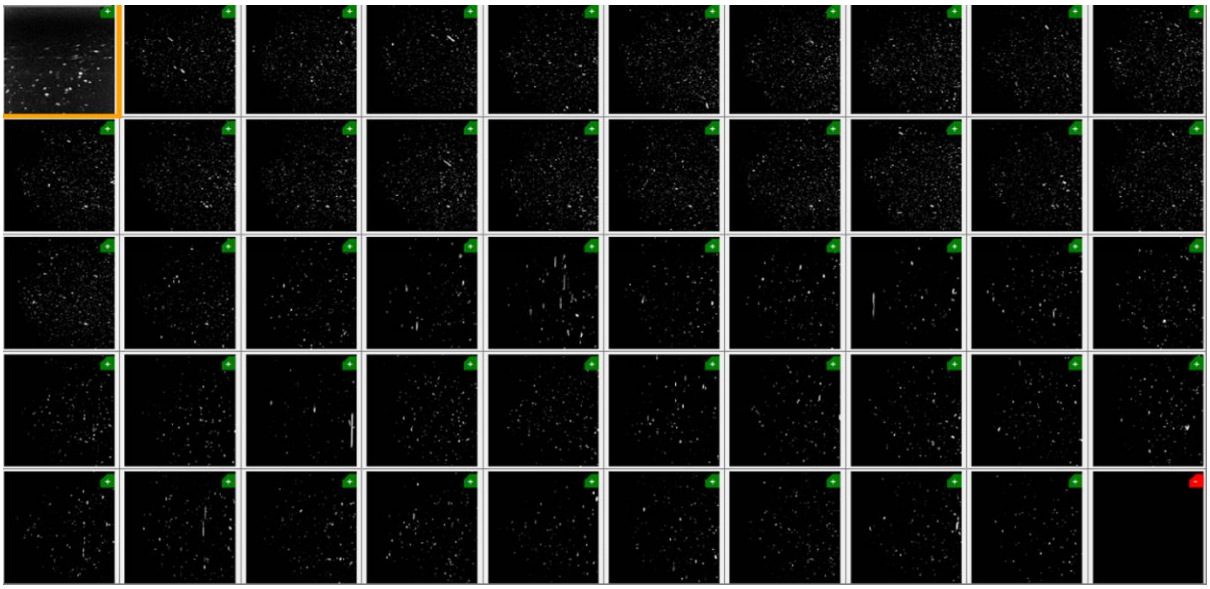

Figure 3.4. Representative images of 500 nm $BaTiO_3$ in water in a flow cell using 50 mW laser power and ~500 μs exposure.

images were collected as a test of the system. The streaking of the particles than can be seen is expected since the particles couldbe moving during imaging. The nature of the peristaltic pump used in this experiment allows for some time when the flow is stopped, explaining why some images do not show streaking while others do. It is also possible that some of the images are focused onto a plane of the flow cell where the flow is slower or non-existent (i.e. on the window surface). These proof of concept measurements illustrate the potential for the use of SONICC with a flow cell.

3.4 Summary

In this work, TL measurements were performed using a flow cell architecture for detection of trace crystallinity within slurries. A calibration curve was generated using early results from known concentrations of griseofulvin within deionized water and a detection limit of 0.2 ± 0.08

mg/mL was calculated. The higher limit of detection was expected compared to the TL from powders due to the mechanism for TL generation, and the high error is due to the stochastic nature of the measurements. From these results, dissolution and stability tests can be performed within slurries with TL measurements. The proof of concept images from the flow cell within the SONICC system provide promise for its use with a flow cell.

3.5 Future Work

Further work is required to optimize the flow cell design. The results shown were collected using an early version of the flow cell with several flaws. A major flaw isthe fragile nature of the optically transparent windows that are also potentially blocking a significant portion of the light generated during the TL events. A redesign of the flow cell that allows for more force from the piston and more light to be collected will increase the signal to noise and lower the detection limits of the instrument. Dissolution tests with the API posaconazole are in the process of being performed. Additional experiments are underway with the flow cell in the SONICC system with posaconazole for a dissolution test and griseofulvin for a calibration curve.

CHAPTER 4. ITERATIVE NON-NEGATIVE MATRIX FACTORIZATION FILTER FOR BLIND DECONVOLUTION IN PHOTON/ION COUNTING

Reprinted (adapted) with permission from Scott R. G., John A. B., Casey J. S., Ximeng Y., Julia K. W., Si-Wei Z., Julie N., Zhen L., Garth J. S., Iterative non-negative matrix factorization filter for blind deconvolution in photon/ion counting, *Analytical Chemistry* **2019** 91 (8), 5286-5294.

4.1 Introduction

Deconvolution of complex waveforms is a common problem in measurement science of digital signals, with applications spanning super-resolution microscopy, fluorescence lifetime analysis, spectroscopy, and image generation from single-photon/particle counting measurements.[67] In these applications, deconvolution substantially improves resolution in space, time, and frequency. As such, a diverse portfolio of algorithms exists to enable routine deconvolution of digital signals. One common strategy is to perform a digital convolution with a modified form of an inverse function to undo the impact of the original instrumental convolution. The Wiener filter is a common example in which the inverse filter is weighted by the frequency-dependent signal-to-noise in the Fourier domain.[68] Richardson-Lucy deconvolution is another common iterative method for deblurring an image from a known point spread function.[69] Other techniques used for deconvolution include system identification,[70-71] constrained optimization,[70, 72] the use of cubic spline basis functions,[70, 73] maximum entropy,[70, 74] and genetic algorithms.[70] More recently, digital filters derived from linear discriminant analysis (LDA) have been shown to enable digital deconvolution without explicit need for independently assessing the noise characteristics of the instrument.[75] While generally successful, this previous suite of techniques is collectively only applicable for systems in which the impulse response function (IRF) of the instrument is known a priori. Unfortunately, this foreknowledge is not always trivial to obtain. Independent measurements from model systems of single photons/particles/wavelengths may not be available or easily accessible. Furthermore, drift in instrumental parameters can result in time-dependent changes in the IRF between the calibration and the measurement steps, potentially invalidating deconvolution approaches requiring foreknowledge of the IRF.

To address this limitation, there is a clear need in developing blind deconvolution strategies, in which the measurements themselves provide sufficient information to support recovery of both the IRF and the deconvolved output in a single integrated analysis. Blind Richardson-Lucy (BRL) deconvolution, commonly used in image analysis, assumes a general functional form of the convolution kernel (i.e., point spread function) and relies on an iterative maximum-likelihood approach for deconvolution.[76] Alternatively, a method for using least-squares deconvolution with Laguerre expansions can be applied to deconvolution of exponentially decaying functions by interepreting the time-dependent evolution as a linear combination of Laguerre polynomial functions.[77] While the Laguerre expansion method is well suited to fluorescence lifetime recovery by the nature of the exponential components within the Laguerre polynomials, both Laguerre and Richardson-Lucy approaches are still relatively sensitive to the particular selection of inputs used to form the basis set for the deconvolution. As such, significant assumptions regarding the general functional form for the IRF are typically required prior to implementation, limiting extension to broader classes of unsupervised deconvolution challenges in which substantial a priori information on the IRF is not available. Furthermore, the degree to which the results accurately converge to recover the underlying IRF and deconvolved data hinge on the similarity between the IRF and the generating basis set functions.

The challenges and potential benefits associated with blind deconvolution are particularly prominent in single particle measurements with complex IRFs, such as often arise in ion and photon counting. The interplay between optics and electronics can result in nontrivial IRFs that are difficult to predict a priori and correspondingly difficult to universally describe by the approaches in the preceding paragraph. However, the rewards for success in deconvolution are numerous. Photon counting (PC) is well established as a successful strategy for sensitive detection of low intensity light and is widely used in applications ranging from time-resolved fluorescence measurements to quantum computing at wavelengths spanning the infrared through the X-ray.[78-79] PC typically operates in Geiger mode, in which a photon-induced voltage transient exceeds some critical threshold and registers as a digital count. The principle advantage of photon counting is the elimination of electronic white noise and noise contributions from the shot to shot variance in the detector gain. However, PC generally exhibits a limited dynamic range stemming from pulse-pile-up, in which the time frame for adjacent photon events arises fast relative to the duration of the single-photon IRF. Conceptually, this dynamic range limitation arises from the convolution of

the instantaneous photon arrival event with the IRF.[80] As a result, the nature of the IRF and the ability to successfully perform deconvolution directly impact the temporal resolution, sensitivity, and dynamic range of photon counting.

Complications from a complex IRF in photon counting are clearly illustrated in a recent work based on triboluminescence (TL) detection of crystalline drugs within nominally amorphous pharmaceutical materials, such as amorphous solid dispersions (ASDs).[34] TL describes the emission of light during mechanical action on the crystalline fraction of an ASD. ASDs are samples of interest, as they are most commonly used as pharmaceutical formulations where the active pharmaceutical ingredient (API) is kinetically trapped in an amorphous state by a polymer matrix, most commonly via hot melt extrusion or spray drying. Residual crystallinity has the potential to decrease the stability of ASDs. Therefore, a sensitive, crystal selective method, such as TL, is desirable for early detection of drug crystallization to identify quality concerns during the early stage of formulation exploration. While previous studies have demonstrated the utility of TL in this application-space, fundamental understanding of the origin of the TL signal production will provide a foundation for assessing the potential broader scope of use.[34, 81-83] Deconvolution of the TL signal will allow for a greater fundamental understanding of the mechanism underpinning TL measurements.

The temporal duration of these bursts complicates studies to elucidate the fundamental dominant mechanisms driving signal production; the detection electronics must be slow enough to capture the entire burst envelope, but fast enough to enable meaningful recovery of the characteristic time scales of the individual single crystal TL bursts. Two likely mechanisms were proposed for TL production from organic crystals: (i) TL production from piezoelectric activity within the crystal, resulting in dielectric breakdown and plasma luminescence and (ii) solid-state electron/hole recombination resulting in light emission. In principle, the characteristic time frame for light emission should be quite different for these two mechanisms, providing a means for discriminating between them. In practice, this analysis is complicated by practical considerations associated with experimental constraints. A single TL burst envelope often contains emission of hundreds of photons generated by many crystals over a few microseconds to milliseconds. Detection of single-photon events arising within a burst envelope was promoted through intentional impedance mismatch, in which the terminal impedance at the oscilloscope card was set to a value higher than the impedance of the transmission line. While this approach greatly improves

the signal-to-noise for quantification courtesy of Ohms Law and extends the temporal envelope of single photon events for ease in digital detection, it also resulted in a complex IRF containing substantial ringing from electronic reflections arising from the mismatched impedance.

In the work described herein, a digital filtering approach integrating non-negative matrix factorization (NMF) for blind deconvolution is developed theoretically and subsequently applied to deconvolve the time-trace of TL events. The use of NMF exploits the fundamental physics associated with the signal production. The number of photons arriving at a given position in time must strictly be a positive integer. Similarly, photon absorption at the detector results in a cascade of electrons producing dominant voltage transients identical in sign each time. This strategy builds on an alternating least-squares formulation of NMF, in which conventionally a data matrix $\boldsymbol{V}$ is expressed as the product of two matrices $\boldsymbol{WH}$ containing only non-negative entries. Using an initial guess for one matrix ($\boldsymbol{W}$) allows identification of the entries of the second ($\boldsymbol{H}$), which minimize the sum of squared deviations between the data and the matrix product. Using only the non-negative entries for $\boldsymbol{H}$, the process is repeated to solve for the entries of ($\boldsymbol{W}$). In this manner, $\boldsymbol{H}$ and $\boldsymbol{W}$ are solved iteratively until non-negativity in each is achieved. In order to perform deconvolution of single-photon events from a time-trace, this general strategy of NMF was modified in two notable ways: (i) the NMF mathematical framework was adapted to explicitly incorporate convolution and deconvolution operations, and (ii) NMF analysis was performed over only small sections of data as a rolling filter to greatly reduce computation cost in the analysis of large data sets. This non-negative matrix factorization filter (NMF-F) approach was evaluated on test data with known ground-truth results, then implemented to provide insights into the fundamental origins of the light-emitting processes underpinning TL measurements of the model pharmaceutical materials doxycycline hyclate, an antibiotic of the tetracycline class, and griseofulvin, an antifungal agent.

4.2 Methodology

The NMF algorithm and related multivariate curve resolution methods[84] are founded on both the alternating least-squares approach originally proposed by Paatero and Tapper (1994)[85] and an adaptation of a convolution model originally proposed by Chambers et al.[86] The objective function in this case corresponds to a maximum likelihood estimate (MLE) based on minimizing the sum of squared deviations between the measured time-trace and the recovered fit. Implicit in

MLE is the assumption of normally distributed, uncorrelated instrument noise, consistent with the experimental expectations of our measurements. In the present case, the intensity of the detected light must be a positive number, serving to constrain a fit to recover the intensity.

In convolutional NMF applied to a time-trace, the detected voltage is represented by the vector $\vec{\boldsymbol{d}}_{meas}$ (m×1), which is the convolution of the ground truth impulse train, $\vec{\boldsymbol{d}}_{true}$ (m×1), with the $\overrightarrow{\boldsymbol{irf}}$ (n×1) and addition of noise. The convolution operation was recast as a product with an $m \times m$ matrix $\boldsymbol{P}$ by convolving the IRF with a identity matrix. Additional noise is indicated by the vector $\vec{e}$, m is the number of digitization events, and n is size of the $\overrightarrow{\boldsymbol{irf}}$. It may appear counterintuitive to expand the initial (n×1) $\overrightarrow{\boldsymbol{irf}}$ to a (m×m) matrix $\boldsymbol{P}=\overrightarrow{\boldsymbol{irf}}\otimes\boldsymbol{I}_m$ through a convolution with an (m×m) identity matrix, considering NMF typically is used to reduce the inherent dimensionality of the data set. However, this expansion was performed for mathematical convenience in casting the convolution operation into a form directly compatible with matrix evaluation and inversion.

$$\begin{aligned}\vec{\boldsymbol{d}}_{meas} &= \overrightarrow{\boldsymbol{irf}} \otimes \vec{\boldsymbol{d}}_{true} + \vec{e} = \overrightarrow{\boldsymbol{irf}} \otimes \left(\boldsymbol{I}_m \vec{\boldsymbol{d}}_{true}\right) + \vec{e} \\ &= \boldsymbol{P} \cdot \vec{\boldsymbol{d}}_{true} + \vec{e}\end{aligned} \tag{4.1}$$

If the IRF were known a priori, the data trace $\vec{\boldsymbol{d}}_{meas}$ could be fit assuming (incorrectly) a photon arrival at each position in time through Equation 4.2. Such a fit recovers the amplitude of the impulse at each position in $\vec{\boldsymbol{d}}_{fit}$, which will initially exactly recover the time-trace $\vec{\boldsymbol{d}}_{meas}$, including errors from noise as the number of equations and parameters are exactly matched. Assuming the rate of photon arrivals is significantly less than the digitization rate, roughly half of the amplitudes of the initial fit will be positive and half negative. All amplitudes less than zero (or more generally, less than a prespecified threshold) can be considered nonphysical and removed (by removing a column from the fitting parameters in $\boldsymbol{P}$) in the evaluation by the nonnegativity criterion, as illustrated in Figure 4.1. This process can be repeated until only positive (above threshold) amplitudes are recovered.

$$\vec{\boldsymbol{d}}_{fit} = (\boldsymbol{P}^T\boldsymbol{P})^{-1}\boldsymbol{P}^T\vec{\boldsymbol{d}}_{meas} \tag{4.2}$$

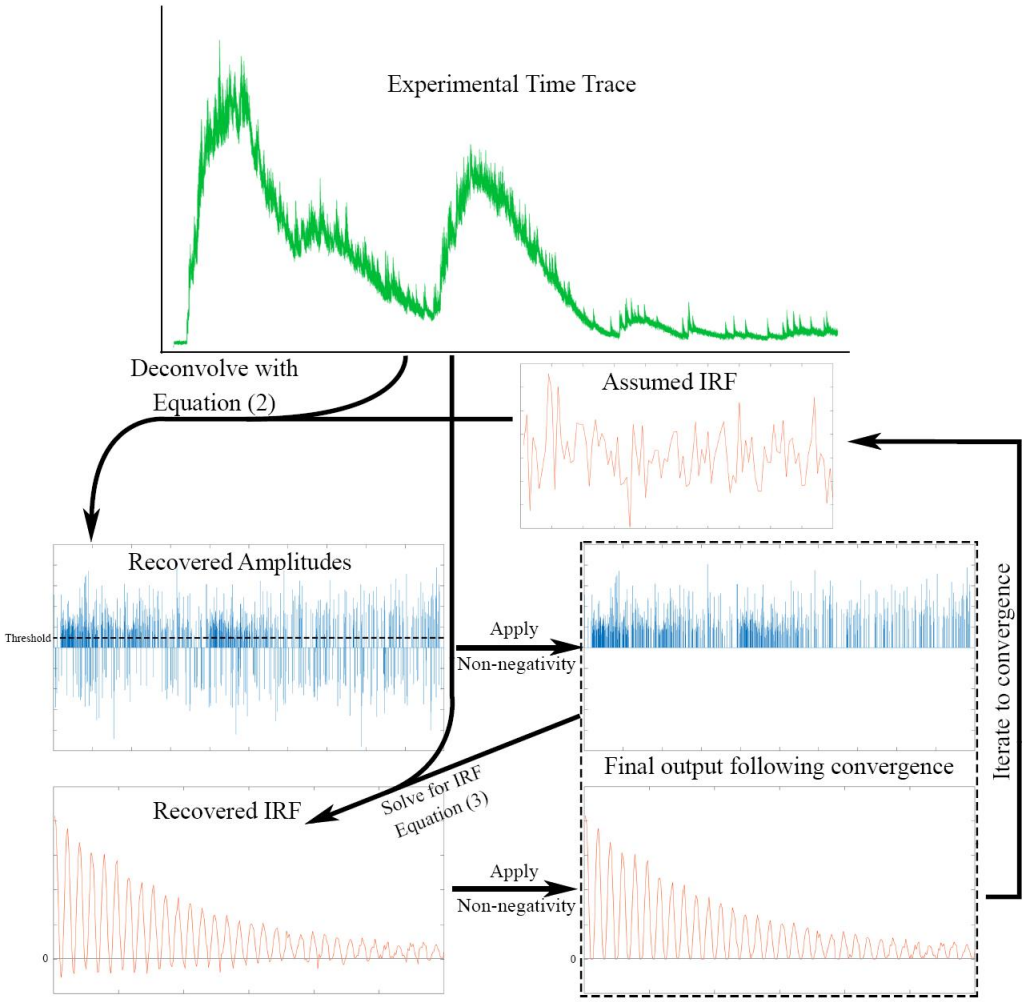

Figure 4.1. Illustration of the NMF-F algorithm.

In practice, this approach requires foreknowledge of the IRF. If, instead, we could somehow know a priori the positions of all the impulses corresponding to photon arrivals given by $\vec{d}_{ex}$ but not the IRF, the problem could be inverted to solve instead for the IRF. This process is illustrated in Equation 4.3. In the absence of measurement noise, the measured data trace can be recovered by the convolution (illustrated by the symbol $\otimes$) of the impulse train with the IRF. Introducing an identity matrix (I) in the convolution allows for matrix inversion and recovery of the best-fit of the IRF based on analysis of the entire time-trace, as shown in Equation 4.3.

$$\overrightarrow{\boldsymbol{irf}} = \left[\left(\vec{\boldsymbol{d}}_{\boldsymbol{fit}} \otimes \boldsymbol{I}_n\right)^T \left(\vec{\boldsymbol{d}}_{fit} \otimes \mathbf{I}_n\right)\right]^{-1} \left(\vec{\boldsymbol{d}}_{fit} \otimes \boldsymbol{I}_n\right)^T \vec{\boldsymbol{d}}_{meas} \quad 4.3$$

In this work, the algorithm is made to iterate through both the recovery of the photon events in $\vec{\boldsymbol{d}}_{\boldsymbol{fit}}$ and the IRF. First, the IRF is set to a guess value that we assume is true for the initial recovery of the photon events. Then, the parameters recovered from the first half of the iteration are used in a second least-squares minimization for recovery of the IRF, which is then reused iteratively in the recovery of $\vec{\boldsymbol{d}}_{\boldsymbol{fit}}$ until convergence is achieved. After convergence with non-negativity imposed on the IRF, another round of iterative optimization is performed to allow the recovery of weak but nonzero ringing features by relaxing the non-negativity constraint on the final IRF. The overall workflow of the NMF algorithm is illustrated in Figure 4.1.

In principle, the expressions in Equations 4.2 and 4.3 and can be evaluated on the complete data set as indicated in the equations. In practice, the dimensionality of long data-traces complicates direct inversion in Equation 4.2. Inversion of large data sets belongs to the class of NP-Hard problems in most cases.[87] To help alleviate this problem, NMF was implemented as a rolling filter (NMF-F) on a small subset (n×1) of the data, with the analysis performed over a sliding window across the data vector. The $\vec{\boldsymbol{d}}_{\boldsymbol{meas}}$ vector mentioned in Equation 4.1 was defined to be a 100 point window of the data, which was on the order of the length of the IRF. NMF analysis was performed using Equation 4.2 to identify the locations within the window corresponding to initiation of photon events (assuming a known IRF). This approach is qualitatively similar to a linear fitting digital filter (e.g., Savitsky-Golay), but with the NMF constraints imposed.[88] Following this rolling analysis, the entire data set was used in evaluating the optimal IRF using Equation 4.3, followed by iteration between these two steps until convergence was achieved.

4.2.1 Algorithm

The NMF-F algorithm used in this publication integrates capabilities from both MLE NMF and convolutional NMF to perform a rolling NMF on a convolution operation rather than multiplication. To integrate these disparate approaches, we use the identity operation in matrix

multiplication, combined with the associative property of convolution and multiplication to generate the final expression shown in Equation 4.4.

$$\vec{\boldsymbol{d}}_{meas} = \vec{\boldsymbol{d}}_{true} \otimes \overrightarrow{\boldsymbol{\imath rf}} = \left(\vec{\boldsymbol{d}}_{true} \otimes \boldsymbol{I}\right)\overrightarrow{\boldsymbol{\imath rf}} \qquad 4.4$$

Introduction of the IRF to the convolution in Equation 4.4 allows for the recovery of the best fit of the IRF through Equation 4.3. Convolution of $\vec{\boldsymbol{d}}_{\boldsymbol{fit}}$ with the identity matrix in this manner enables isolation of the IRF for mathematical inversion. Once the IRF is determined, local implementation on short sections of data as a digital filter greatly reduces the computational time. Where a smaller section of the data, $\left[\vec{\boldsymbol{d}}_{\boldsymbol{i}}{:}\,\vec{\boldsymbol{d}}_{i+n}\right]$, which is now n×1, where n is now the desired filter size. This new $\left[\vec{\boldsymbol{d}}_{\boldsymbol{i}}{:}\,\vec{\boldsymbol{d}}_{i+n}\right]$ vector is then evaluated iteratively through the entire data set. Performing the analysis as a rolling filter in this way substantially reduces the time and computational resources required, enabling implementation on simple benchtop computers.

Baseline Correction

1. Convolve data with a high pass filter.

Matrix Factorization

The general strategy for implementing NMF-F is illustrated in Figure 4.2. The NMF-F is evaluated for the i^{th} element over a range of data equal to the length of the IRF, n. A photon event is allowed to arise in every position within that range when evaluating the amplitude of the i^{th} element. This

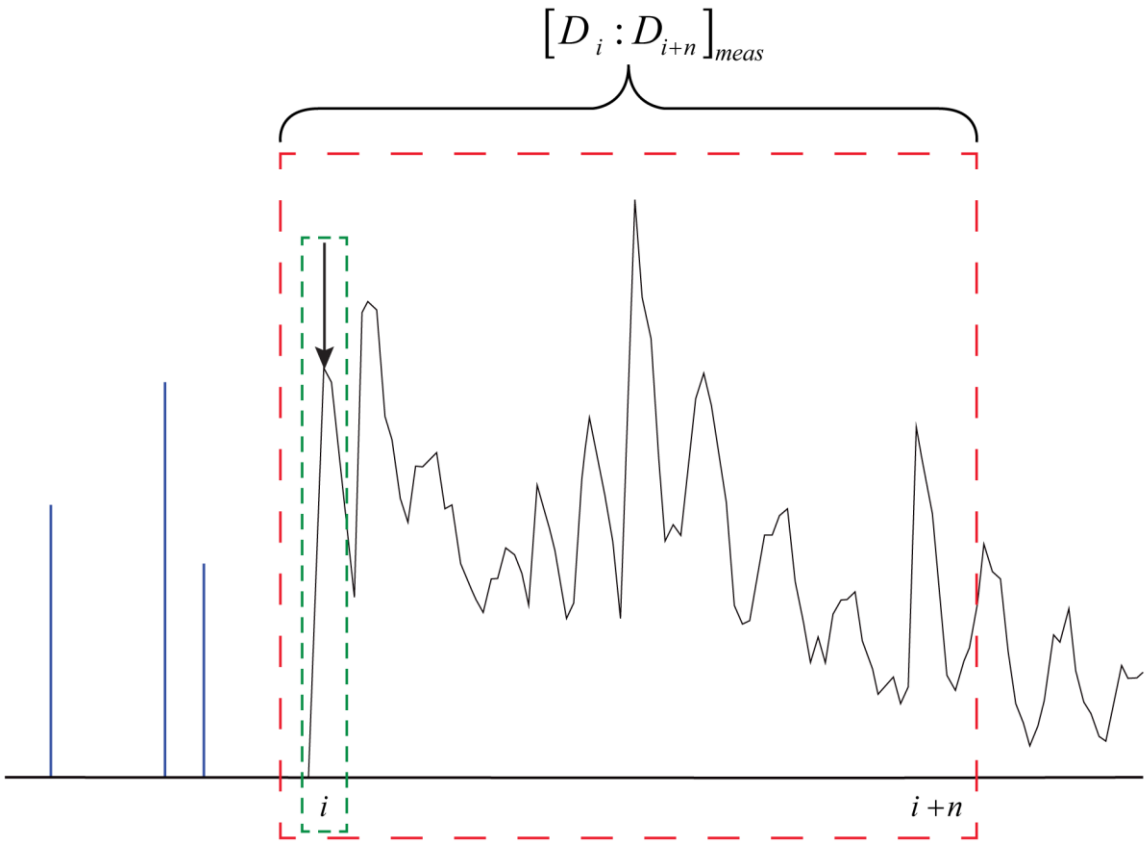

Figure 4.2. An example of the NMF-F algorithm working on a smaller subset of the entire data trace to recover a photon event at position i.

process is repeated for every i^{th} element of the measured data to generate the deconvolved output and recover the IRF.

Initialization

1. Set threshold for negativity constraint (accounting for noise).
2. Generate initial IRF guess (e.g., uniformly distributed random numbers; n = 100).

Solving for the $\vec{\boldsymbol{d}}_{fit,i}$ Element of the $\vec{\boldsymbol{d}}_{fit}$ Vector

1. Generate the matrix $\boldsymbol{P}(n \times n)$by $\boldsymbol{P} = \boldsymbol{I}_n \otimes \overrightarrow{\boldsymbol{irf}}$, where $\boldsymbol{P}$ is initially the convolution of an identity matrix of dimension *n* with the IRF, truncated to produce an *n* × *n* matrix.
2. For the *i*th element of $\boldsymbol{d}_{meas,i}$ select a section of data of length *n* and invert the equation $[\boldsymbol{d_i}: \boldsymbol{d}_{i+n}]_{meas} = [\boldsymbol{d_i}: \boldsymbol{d}_{i+n}]_{fit}\boldsymbol{P}_{(\boldsymbol{n}\times\boldsymbol{n})}$to determine the best fit values of $[\boldsymbol{d_i}: \boldsymbol{d}_{i+n}]_{fit}$.
3. Identify the elements of $[\boldsymbol{d_i}: \boldsymbol{d}_{i+n}]_{fit}$ below threshold and remove the corresponding columns of $\boldsymbol{P}$ to generate $\boldsymbol{P'}_{(\boldsymbol{n}\times\boldsymbol{m})}$, where *m* < *n*.
4. Express $[\boldsymbol{d_i}: \boldsymbol{d}_{i+n}]_{meas} = [\boldsymbol{d_i}: \boldsymbol{d}_{i+n}]_{fit}\boldsymbol{P'}_{(n\times m)}$ and invert to recover an updated $[\boldsymbol{d_i}: \boldsymbol{d}_{i+n}]_{fit}$.
5. Iterate until no below threshold events are recovered for the amplitudes in $[\boldsymbol{d_i}: \boldsymbol{d}_{i+n}]_{fit}$.
6. Retain the value of $\boldsymbol{d}_{fit,i}$. If $\boldsymbol{d}_{fit,i}$ is nonzero, subtract $\boldsymbol{d}_{fit,i} \otimes \overrightarrow{\boldsymbol{irf}}$ from $[\boldsymbol{d_i}: \boldsymbol{d}_{i+n}]_{meas}$.
7. Repeat for all *I* positions of the measured data.

Solving for the IRF

1. Express $\boldsymbol{d}_{meas}$ in the following form:$\boldsymbol{d}_{meas} = \boldsymbol{d}_{fit} \otimes \overrightarrow{\boldsymbol{irf}} = \left(\boldsymbol{d}_{fit} \otimes \boldsymbol{I}_{n\times n}\right)\overrightarrow{\boldsymbol{irf}}$.
2. Multiply by the transpose and invert $\left(\boldsymbol{d}_{fit} \otimes \boldsymbol{I}\right)$ to recover the least-squares best fit values for $\overrightarrow{\boldsymbol{irf}}$.
3. If imposing non-negativity to the IRF, set below threshold entries to zero.

Iterate to Convergence

1. Using the updated IRF, solve for $\boldsymbol{d}_{fit}$ and update.
2. Using the updated $\boldsymbol{d}_{fit}$, solve for the IRF and update.

Autocorrelation

1. Take the fast Fourier transform (FFT) of $\boldsymbol{d}_{fit}$, such that $\phi = FFT(\boldsymbol{d}_{fit})$.
2. Mulitply $\phi\phi^*$ element-wise.
3. Take the inverse FFT of $\phi\phi^*$.

4.3 Experimental

Triboluminescence measurements of the antibiotic doxycycline hyclate in powder form were obtained using an instrument described in detail in a preceding publication.[34] In brief, kinetic energy impulses were delivered to the sample via a solenoid driven impactor, which mechanically compressed the sample to induce triboluminescence. A single impact delivered ~0.5 J over a 7 mm^2 area. The light emitted by the sample was collected and focused onto a photomultiplier tube (PMT, H12310-40, Hamamatsu, Japan) that was connected to a PCI-express digital oscilloscope card (ATS-9350, AlazarTech, Pointe-Claire, QC, Canada) to record the temporal response of the detector. An Arduino microcontroller was used to trigger data collection and control movement of the sample stage. An impedance mismatch was intentionally introduced between the transmission line (50Ω) and the digitizing electronics (1MΩ). This mismatch provided a signal-to-noise advantage through two independent mechanisms: (i) increasing the integrated voltage through the increased resistance of the digitizer according to Ohms Law, V = IR, and (ii) simplifying digitization of the transients by increasing the temporal duration of each voltage transient according to the RC time constant associated with discharge of the transmission line capacitance through the resister. The increase in voltage manifested as a series of reflections separated by the round-trip transit time through the transmission line of ~100 ns, followed by eventual decoherence to a constant baseline offset. The resulting complex waveform produced by an impulsive photon absorption event still retains essentially the same high frequency information content of the original current transient from the detector, but with different frequencies shifted in phase to produce the observed impulse response function.

Simulations were conducted to quantitatively evaluate the performance of the NMF-F for systems with known ground truth results. A Poisson probability density function (pdf) was used for describing the probability of detecting a photon during an individual impact event. Because the duration of the burst was much longer than the digitization rate, the maximum mean of the Poisson distribution was still less than one at all time-points within the burst profile. For each detected photon, the amplitude was determined by a log-normal pdf describing the variance in gain within the dynode string of the PMT used.[89] Once the ground truth was established for the locations and amplitudes of the voltage transients, each voltage transient was then convolved with an impulse response function measured for a single photon event. Finally, normally distributed white noise with a mean of 0 and a standard deviation an order of magnitude lower than the maximum photon

amplitude was added to make the simulated time trace. These data were used to evaluate the algorithm's ability to accurately recover photon events with increasing probabilities of pulse pile-up, in which a new photon event is initiated within the temporal envelope of a preceding IRF.

Comparisons were performed between the NMF-F approach and conventional NMF of the entire data set en masse. In conventional NMF, computational time generally increases nonpolynomially with data size (is an NP-hard problem in most cases), which results in large computational time savings from any reduction in the set size. As a consequence of this scaling, attempts to perform conventional NMF on the nearly 2.5 million data points from a single impact event resulted in impractically long computational times, despite performing calculations with sparsity constraints on the Purdue Radon Supercomputing Cluster (45 nodes, One Hyper-Threaded Quad-Core Xeon E3-1284*L*/8 cores/32 GB RAM per node). By comparison, use of the sliding filter design in NMF-F enabled analysis in ~18 min for pooled analysis of 35 impact events (87.5 million data points) on a Dell XP15 laptop with a 2.6 GHz processor and 16 GB of RAM.

TL measurements were performed on griseofulvin amorphous solid dispersion (ASD) samples. Griseofulvin was obtained from Sigma-Aldrich (St. Louis, MO), and hydroxypropylmethylcellulose acetate succinate (HPMCAS) was purchased as AQOAT from Shin Etsu (Tokyo, Japan). The spray dry formulation comprised of griseofulvin (20% w/w) and HPMCAS-MF (80% w/w). The solid components were dissolved in acetone (4% w/v). The solution was spray dried on a 4M8-TriX spray dryer (ProCepT NV, Zelzate, Belgium) with a two-fluid nozzle diameter of 0.6 mm. The dried particles were carried by air into a cyclone and then into a collection vessel. The processing air flow rate was set to be 0.40 m^3/min. The atomization air and the solution feed flow rates were taken to be 3.0 L/min and 6 mL/min, respectively. The spray drying conditions were set to reach inlet temperature of 91 °C and outlet temperature of 50 °C. The cyclone differential pressure was set at 30 mbar and tangential air flow rate was chosen to be 0.1 m^3/min, while the cooling air was shut off. The spray dried products were further dried under vacuum at ambient temperature overnight. The griseofulvin ASD was confirmed to be amorphous using powder X-ray diffraction (PXRD), second harmonic generation (SHG) microscopy, and TL following preparation. The ASD was then stressed for 48 h at 65 °C and at elevated relative humidity using a saturated NaCl solution to induce crystallization.

4.4 Results and Discussion

A representative time-trace for a TL measurement is shown in Figure 4.3. Several key aspects of the measurement are noteworthy. First, at least three separate burst events are detectable from the time-trace, the first of which at ~0.1 ms being the largest. Second, the intentional impedance mismatch introduces a relatively long exponential decay on the detected signals arising from burst events. Third and less obviously at this scale, the time-trace includes high-frequency spikes arising from the absorption of individual photons. While the impedance mismatch was advantageous for detection of the individual transients, the resulting temporal convolution substantially complicated efforts to characterize the intrinsic burst profile of individual TL events and inform models for describing the mechanisms of TL production.

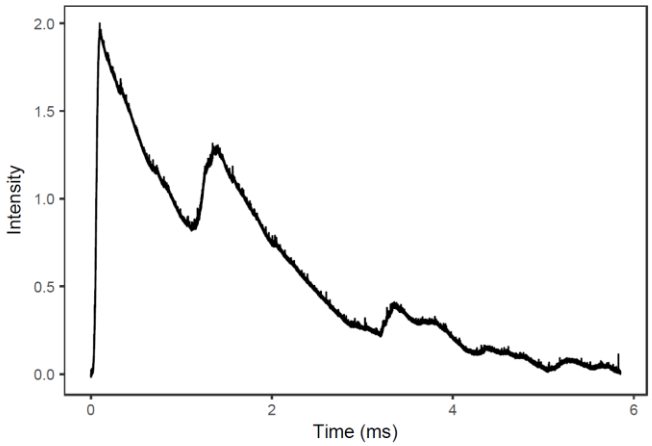

Figure 4.3. Example signal transient pulled from a larger set of TL measurements which illustrate the complexity and difficulty in distinguishing individual photon events. Transients on a μs time scale appear as impulses over the ms time scale of the emission even

The merits and limitations of the NMF-F were initially evaluated using the simulated data as shown in Figure 4.4, for which ground-truth results were known a priori for algorithm evaluation. NMF-F was compared to standard blind Richardson-Lucy (BRL) deconvolution and to deconvolution using a Wiener filter, which requires advanced foreknowledge of the IRF. The Wiener deconvolution performed with a noise-free exact IRF approaches the theoretical limiting behavior expected by any blind deconvolution algorithm, including NMF-F. The signal transients recovered by NMF-F analysis are shown in Figure 4.4a (blue trace-top) along with a comparison with the simulations (black trace-bottom). The IRF recovered using the NMF-F algorithm is shown in Figure 4.4b (blue dashed-middle), together with the initial guess (red-bottom) used for the IRF to initiate the NMF-F. While the NMF-F algorithm converges well for random initial guess inputs for the IRF (vide infra), the BRL algorithm used as a comparator required initial guesses for the IRF with significant similarities to the ground truth result for computational convergence. The

recovered photon events (blue-top) by NMF-F were compared with the ground truth positions (black-bottom) in Figure 4.4c, in which the ground truth results were plotted as negative transients to help visualize peak positions. Receiver operating characteristic (ROC) plots were calculated in Figure 4.4d to assess the ability of the algorithm for reliable recovery of single-photon events relative to blind deconvolution by BRL and by the Weiner filter using the exact IRF. This process was performed for a mean number of photons per digitization time point, $\lambda = 0.1$, which is the Poisson distribution mean value. For example, $\lambda = 0.1$ corresponds to a photon originating every 10th digitization event on average. As shown in the ROC plot in Figure 4.4d, the area under the curve is close to unity for NMF-F, suggesting the potential for low false positive and false negative rates following NMF-F deconvolution. Most significantly, blind NMF-F substantially outperforms

the comparator BRL algorithm, approaching behaviors anticipated by algorithms with exact foreknowledge of the IRF.

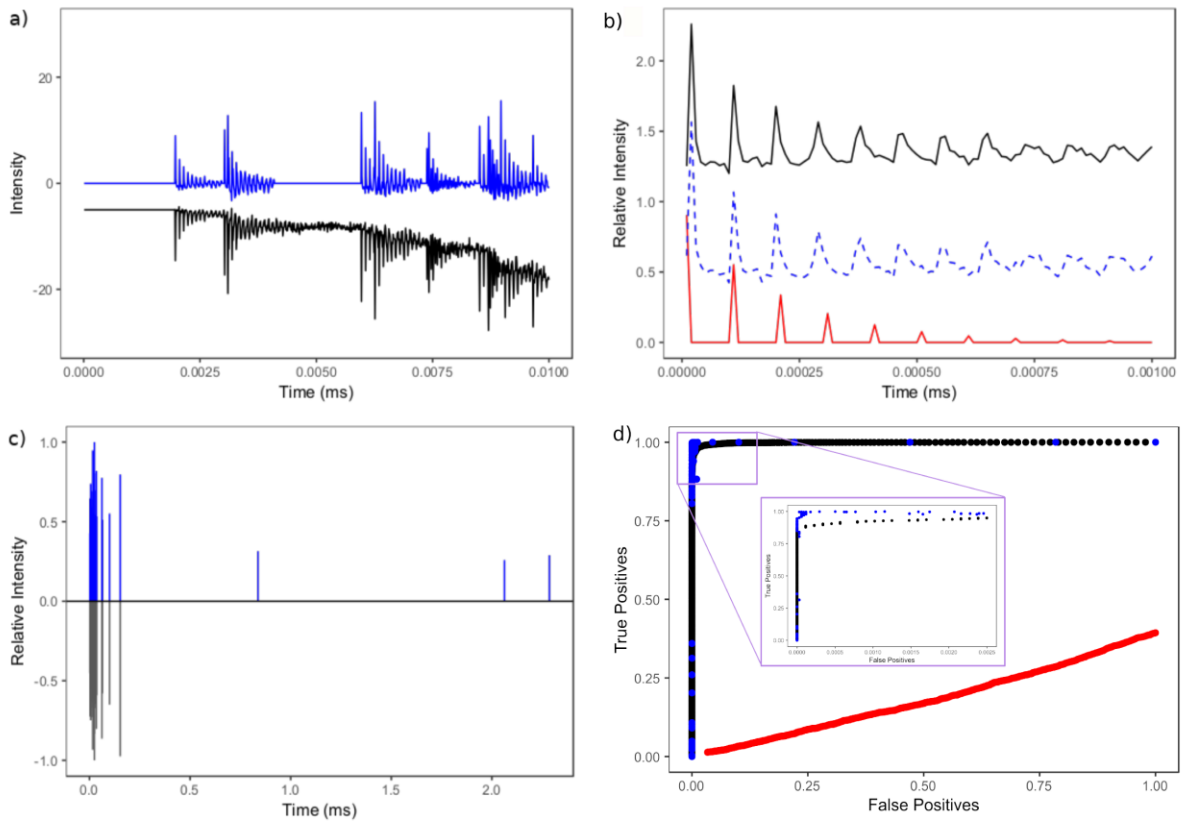

Figure 4.4. Using simulated data zoomed in to microsecond time scales and normalized results for ease of comparison with the ground truth. (a) The recovered transient (blue-top) compared to the original simulated transient (black-bottom), where the black trace is displayed with negative amplitude for ease of comparison. (b) The ground truth (black-top, offset by 1 Norm.U.), recovered (blue dashed, offset by 0.5 Norm.U.), and initial guess (red-bottom) IRFs are compared and show good agreement. (c) The recovered photon events (blue-top) are compared with the ground truth events (black-bottom) and show nearly complete recovery with minimal error. The digital filter's accuracy and ability to recover photons in high density data is highlighted in (d), by the ROC plots made with the same data and analyzed using NMF-F (blue), Wiener deconvolution (black), and BRL (red). Both the Wiener deconvolution and BRL were performed using the true IRF, while the NMF-F analysis was performed with a good guess from previous experiments. The AUC for NMF-F is 0.987 and 0.998 for the Wiener deconvolution. While the NMF-F performed better at lower false positive rates, it performs worse as the false positive rate increases.

The insensitivity of the NMF-F approach to the initial guess for the impulse response function was assessed by repeating the analysis for a host of different initial IRF guesses. Initial waveforms for the assumed IRF included single impulses, pulse trains with incorrect periods, and random normally distributed waveforms. Each individual implementation of NMF-F blind deconvolution with the most challenged case of fully randomized input, results in convergence recovering both the IRF and the deconvolved time-trace with a success rate of 82.5%, the remainder of which converges to IRFs containing many impulses that more resemble the Gaussian noise. As such, implementation with just five initial random guesses results in a 99.92% chance for successful convergence with no a priori knowledge. Of course, this success rate of individual implementations can approach unity with initial guesses based on prior knowledge. Fortunately, identification of the outliers was straightforward, as they greatly overestimated/underestimated the total number of detected photons relative to the set closely matching the ground truth IRF or produces an IRF that is not realistic. An example with a random guess for the IRF is shown in Figure 4.5, indicating both the initial IRF, the final convergent solution for the IRF generated by the NMF-F and BRL, the ground truth IRF, and the fraction of single photon events properly

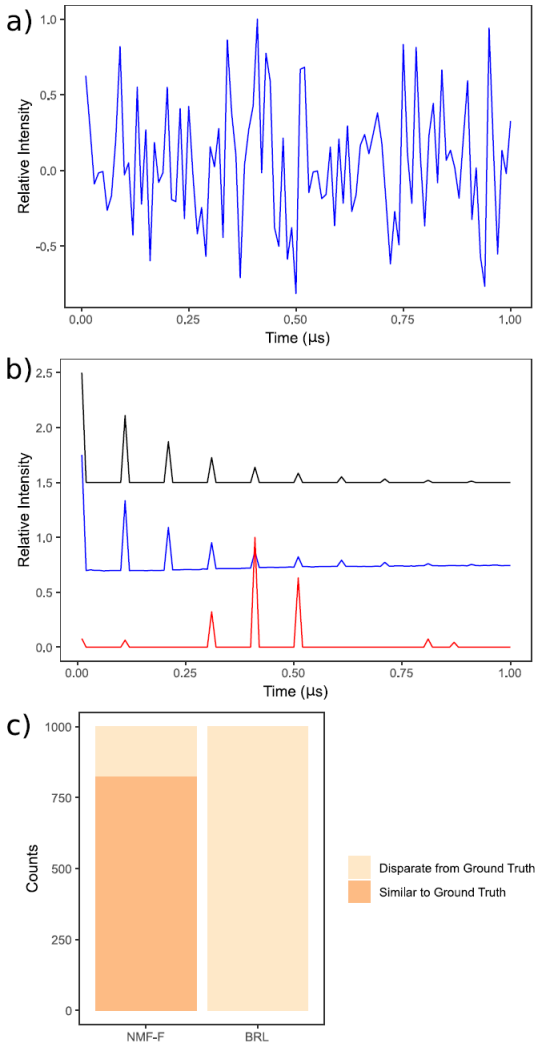

Figure 4.5. An example of the algorithm's ability to recover an IRF similar to the ground truth. (a) Representative initial random guess used in the NMF-F and the BRL algorithm. (b) Recovered IRFs for the NMF-F (blue-middle) and BRL (red-bottom) algorithms are compared with the ground truth (black-top), which are offset for ease of comparison. (c) Bar chart highlighting the difference in ability to recover an IRF similar to the ground truth of the NMF-F and BRL algorithms. NMF-F converged to a similar IRF to the ground truth 82.5% of 1000 attempts, while BRL failed in all attempts.

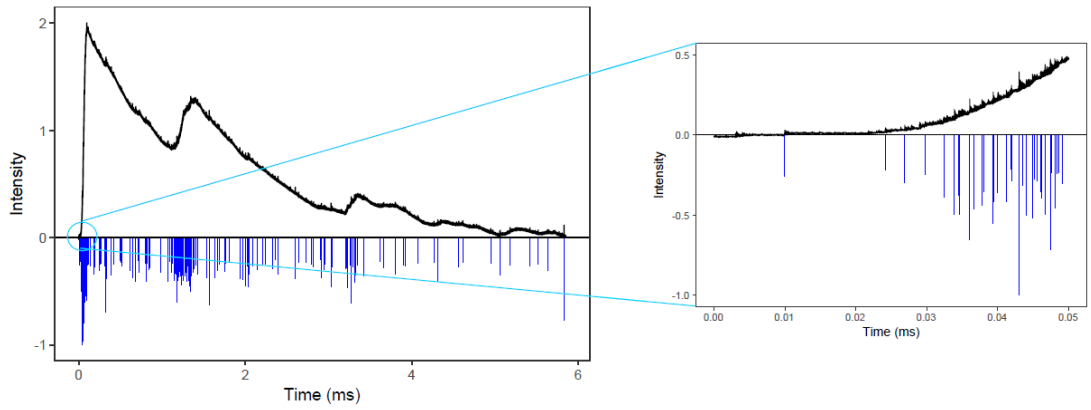

Figure 4.6. Same TL signal transient from Figure 4.3 (black-upper) with the recovered photon events (blue-lower). The inset illustrates how many photons are within the initial rise caused by a TL burst event.

identified by the NMF-F (~97%). Given the complexity and high frequency content of the ground truth IRF, the recovery of reasonable results for random initial guess values is quite remarkable and attests to the overall stability of the NMF-F computational method. No comparable convergence could be achieved using the BRL algorithm. It is worth emphasizing that analysis with a random guess requires no significant prior knowledge or assumptions of either the photon positions or the instrumental IRF.

Next, the NMF-F was applied to the measured triboluminescence signal shown in Figure 4.3. The results of the deconvolution are shown in Figure 4.6, in which the photon arrival times are compared with the original data. The expanded portion of Figure 4.6 allows identification of individual photon events at the beginning of a burst generated from a triboluminescence event. From inspection of the results, the deconvolution algorithm notably increases the localization of photon events and suppresses noise from convolution with the IRF, from the baseline offset, and from the

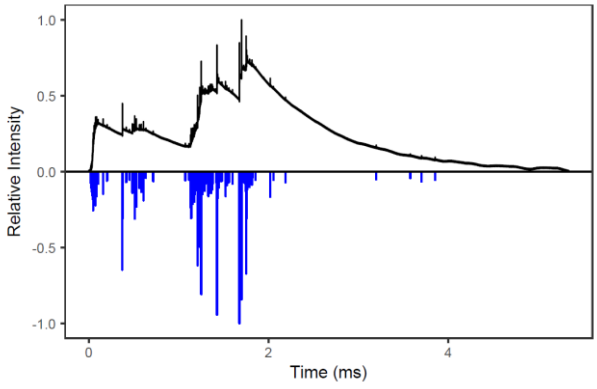

Figure 4.7. Amorphous solid dispersion of griseofulvin in HPMCAS stressed to induce crystallinity (black trace-upper) and the recovered photon events (blue trace-lower).

white electronic noise. In Figure 4.7, the NMF-F algorithm was applied to the ASD sample, where crystals were grown in elevated humidity and temperature.

Following deconvolution, autocorrelation analysis of the measured TL time-traces was performed to yield information on the characteristic time-scale for the individual burst events, and in turn insights into the mechanisms of TL in pharmaceutical powders.[90] The results of the autocorrelation analysis are shown in Figure 4.8, revealing a characteristic time scale for the burst events on the order of ~50 µs. The importance of deconvolution is also illustrated in Figure 4.8, in which the autocorrelation analysis of the raw time-trace as received produced bias by a factor of ~10 in the evaluation of the characteristic time scale. The bias seen in the autocorrelation of the raw data $\vec{c}_{meas}(\tau)$ can be explained by Equation 4.5. The autocorrelation is affected by both the inherent characteristics of the TL process $\vec{c}_s(\tau)$ and the IRF $\vec{c}_{IRF}(\tau)$, where in this case the IRF influence dominates.

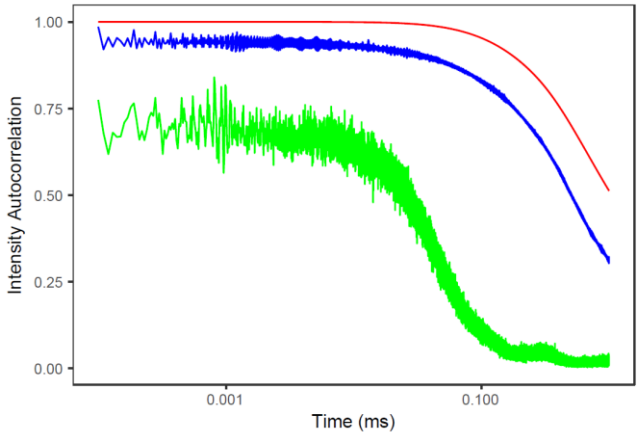

Figure 4.8. Results of autocorrelation on the raw TL data (red-top), the deconvolved photon events (green-bottom), and the measured IRF (blue-middle), where the *x*-axis is on a log scale.

$$\vec{c}_{meas}(\tau) = \vec{c}_s(\tau) \otimes \vec{c}_{IRF}(\tau) \quad 4.5$$

Inspection of the deconvolved autocorrelogram for TL bursts provides several insights into the possible mechanisms driving the observed signal production. Notably, temporally longer recurrences in the autocorrelogram that might arise from ringing events were not observed, consistent with TL arising stochastically in ~50 µs bursts. High-speed imaging was performed to assess the piston speed at the point of impact and from that the time scale for traversal through the sample. The maximum piston speed was ~2 m/s corresponding to the piston taking ~0.5 ms to travel though the 1 mm thick sample. This time scale is significantly longer than the individual burst events from autocorrelation analysis, but comparable to the entire envelope of bursts

produced by a single impact event. The 50 μs time scale is in qualitative agreement with the ~20 μs temporal envelopes reported in laser-induced breakdown spectroscopy experiments, where emission of excited gas-phase AlO caused by a spark created by a laser pulse was measured over time in different bath gases.[91]

Consistent with this collective set of results, we can propose the following mechanism for the observed TL. During the ~500 μs traversal of the piston through the powdered sample, individual crystalline particles independently produced TL. The temporal profiles of these individual TL bursts were consistent with localized plasma production from dielectric breakdown, presumably from rapid changes in capacitance upon lattice collapse. In some TL events, multiple bursts were observed, consistent with the collapse of several different independent particles during the ~500 μs impact event. The routine observation of the most pronounced TL burst amplitudes relatively early in the impact window is consistent with the larger particles collapsing at earlier times, subsequently followed by bursts associated with smaller crystals, as shown by the secondary peaks in Figure 4.2.[34]

If individual TL bursts arise from the stochastic collapse of individual particles, as suggested by these measurements, a TL mechanism based on capacitive discharge should enable quantitative connections to be drawn between the crystal size and the amplitude of the individual TL burst events. Such connections would raise the intriguing possibility of probing the crystal size distribution from the histogram of intensities for the individual TL bursts. This histogram would be dependent on the size distribution of individual crystals, which is distinct and complementary to the conglomerate particle size distribution most easily accessible from alternative analysis approaches.

4.5 Conclusions

An NMF-F digital deconvolution algorithm was developed to support blind deconvolution in photon counting and subsequently used for the analysis of TL observations. In addition to reliably recovering arrival times in simulations with known ground-truth results, the NMF-F algorithm simultaneously recovered reliable estimates for the ground-truth impulse response function. Adaptation of NMF as a digital filter enabled analysis of high-density data traces that were prohibitively time-consuming for conventional NMF analysis. Random initial guesses for the

IRF converged to results similar to the ground truth 82.5% of the time, recovering 97% of the impulse events with a false positive rate of 0.06%, with no required prior knowledge of the IRF.

Autocorrelation analysis was performed on the deconvolved impulse train to evaluate several hypotheses regarding the fundamental mechanism of triboluminescence.[92] The result provided the characteristic time scales of triboluminescence emission events, which was obscured in the original data transients from convolution by the impulse response function. The recovered time scale for TL bursts was consistent with a mechanism for TL arising from single crystals fracturing and producing plasma discharge as they were impacted by the piston. This proposed mechanism leads to the possibility of probing crystal size distribution through TL measurements.

CHAPTER 5. SINGLE PARTICLE GROWTH RATE DISTRIBUTIONS BY IN SITU SINGLE PARTICLE TRACKING

Reprinted (adapted) with permission from Sreya S.,*, Zhengtian S.,*, Scott R. G., Nita T., Andrew D. V., Alexander R., Gerald D. D., Garth J. S., *Molecular Pharmaceutics* **2020** 17 (3), 769-776.

5.1 Introduction

Production of amorphous solid dispersions (ASDs) offers a broadly applicable approach for kinetically circumventing solubility limitations of poorly soluble active pharmaceutical ingredients (APIs). In an ASD, the API is cast in a glassy polymer matrix with relatively high aqueous solubility, such that the API is forced into solution upon dissolution of the matrix.[93-96] When optimizing a polymer/excipient/API cocktail for preparing final dosage forms, one critical consideration is the long-term stability of the API within the ASD. Concentrating the API in the ASD to minimize the total mass load of the final dosage form is balanced by a desire to also reduce the chances of API nucleation and crystallization during storage of the ASD. For poorly soluble APIs, the crystalline form often exhibits negligible bioavailability, passing through the digestive tract for oral final dosage forms. In intravital formulations, residual insoluble API particulates can pose additional risks from inducing foreign body embolism.[46, 86, 97-98] For these reasons, stability testing is widely used to inform the optimization of final dosage forms. High throughput testing requires a host of different test materials, multiple replicates of which at multiple time points are required for stability assessment over long timeframes (up to year-long timeframes). The high throughput, high sampling rate, and long incubation times (weeks to months) can significantly complicate sample preparation and storage capacities even when using accelerated conditions.

The duration of stability testing is ultimately dictated by the sensitivity with which crystal formation can be quantified for informing kinetic modeling, with a suite of methods currently brought to bear to address this measurement challenge. These include polarized light microscopy (PLM)[14, 99], X-ray powder diffraction (PXRD)[15, 22], differential scanning calorimetry (DSC)[14, 63, 100], Raman spectroscopy[44-45], Fourier transform infrared spectroscopy (FTIR)[41-42, 44], and solid state nuclear magnetic resonance (sNMR)[20, 44]. PLM is one of the most common methods used for

determining the presence of crystalline content in stability testing. Despite its widespread use, PLM can only provide qualitative information on optically transparent samples and is commonly complicated by interference from occlusions, contaminants, and crystalline excipients.[99] As a consequence, PLM is challenging to integrate into fully automated quantitative analyses of crystallinity. PXRD is arguably the current "gold standard" for detecting trace crystallinity within the pharmaceutical industry but generally does not enable quantification at low crystallinity, takes several minutes for sample preparation/analysis, and requires several mg of material for analysis. A large dynamic range with correspondingly low limits of detection has multiple benefits in accelerated stability testing, including: i) improved statistical confidence in kinetics parameters, ii) simplified kinetic modeling without the need to account for depletion effects, iii) compatibility with low API-load ASDs, iv) reduced volumes for sample storage during testing, and v) reduction in the timeframe necessary for decision-making in stability assessments. For the majority of the methods routinely used for API analysis, limits of detection are on the order of a fraction of a percent, providing a relatively narrow dynamic range in crystalline API detection; in some cases, the total drug loading may only be on the order of a few percent.

In addition to the limited dynamic range, the majority of these common analysis tools probe only ensemble-average behaviors, masking possible intrinsic heterogeneity in crystal nucleation and growth kinetics. For example, it is well established that the nucleation and growth kinetics can differ substantially for crystals generated on the surfaces of ASD particles relative to the bulk.[41, 101] Even in homogeneous media, subtle differences in local environment can produce variance in crystal growth rates.[102] The impact of this variance in growth kinetics on subsequent performance remains unresolved, due in part to the dearth of methods currently available to quantitatively inform the inherent variation in single-particle growth kinetics.

Nonlinear optical imaging has the potential to provide the limits of detection required for investigating single-particle growth kinetics and fill this knowledge gap. Nonlinear optics has recently gained traction in the pharmaceutical industry for sensitive detection and quantification of trace crystalline content within amorphous formulations.[21-26] Second harmonic generation (SHG) describes the coherent conversion of light to twice the frequency, which is symmetry-forbidden in centrosymmetric media but allowed in assemblies of lower symmetry, including the large majority of noncentrosymmetric crystals. SHG provides a near background free measurement of the crystalline fraction of an ASD since the disordered, amorphous material will not produce coherent

SHG. Due to the sensitivity and selectivity of SHG, routine measurements can be made with a limit of detection in the ppm regime.[28] Utilizing the sensitivity of SHG to crystalline content for identification of regions of interest, the detection limits for Raman[46, 103] and XRD[27] have been lowered into the ppm regime as well. The low limits of detection of SHG microscopy enabled quantification of crystallization kinetics in ASDs spanning a 4 order of magnitude range in crystallinity.[28-29]

In this work, the quantitative capabilities of SHG analysis are substantially improved further while simultaneously dramatically reducing the total sample volume and storage burden through *in situ* analysis. A controlled environment for *in situ* stability testing (CEiST) was developed to leverage the sensitive, non-destructive analysis capabilities of SHG for continuous monitoring of individual crystallites during nucleogenesis and growth. The CEiST platform allowed for single particle tracking over hours to days under accelerated stability conditions typical for ASD analysis. Monitoring the same fields of view over time lowered noise in determinations of the nucleation rates and crystal growth rates obtained from accelerated stability tests while simultaneously lowering the amount of sample required.

5.2 Experimental Methods

ASD samples of ritonavir (15%), sorbitan monolaurate (10%), copovidone (74%), and colloidal silicon dioxide (1%) were prepared by AbbVie, prepared as spray dried dispersions (SDDs) and hot melt extrudates (HMEs). Samples without the sorbitan monolaurate were also made in which the copovidone weight percent was increased to 84%. HME samples were milled prior to use. The extrudates were made using a lab scale Thermo Scientific® Process 11 Hygienic Parallel twin-screw extruder fed gravimetrically at 0.750 kg/h with a screw speed of 250 rpm. Temperatures in the heating zones ranged from 15 to 150 ºC. The extrudates were milled using a Fitzmill L1A at 6000 rpm and a screen size of 0.033 in round hole. The ASDs by SDD were made using a Büchi® B-290 spray dryer with an inert loop using methanol as the solvent. The feed solution flow rate into the two-fluid nozzle (1.4 mm diameter) was 20 g/min, with nitrogen atomizing gas. The nitrogen process gas was set to 30 kg/h. The inlet and outlet temperatures were 90 ºC and ~ 50 ºC, respectively, while the condenser was held at -20 ºC. All powder samples were placed into the CEiST chamber or into a standard stability chamber as thin layers (~300 µm).

The CEiST's design is shown in Figure 5.1. The CEiST consists of an aluminum block machined to house two sections separated by greased O-rings. Each compartment was kept at different RHs depending on the saturated salt solution put into the two reservoirs within each compartment and being sealed by a plexiglass window and aluminum sleeve held in place by screws. The aluminum sleeve was machined to allow imaging through each well in the main body of the CEiST, while providing heat to the outside of the plexiglass to prevent condensation. Both compartments of the device were kept at an elevated RH of 75% through all experiments by using a saturated NaCl solution. The RH in each compartment of the CEiST was validated using reversible Moisture Indicator strips (Indigo Instruments, 33813-2080). Once each compartment was validated, the indicator strips were no longer used during experiments. The temperature was controlled by using two Tempco low density cartridge heaters (LDC00003) placed at different locations on the CEiST and a thermocouple in the center for feedback control by a custom controller built by the Johnathan Amy Facility at Purdue, depicted in Figure 5.1A. An IR thermal image of the CEiST in Figure 5.1C confirmed uniform temperature within ± 2^{O}C of the set point temperature. Samples were placed onto cover slips and then onto one of the ten wells within the CEiST. For comparative purpose, a standard stability chamber was made by placing saturated sodium chloride solution into the bottom of a desiccator wrapped in heat tape. The temperature of the entire chamber was monitored by thermocouple feedback.

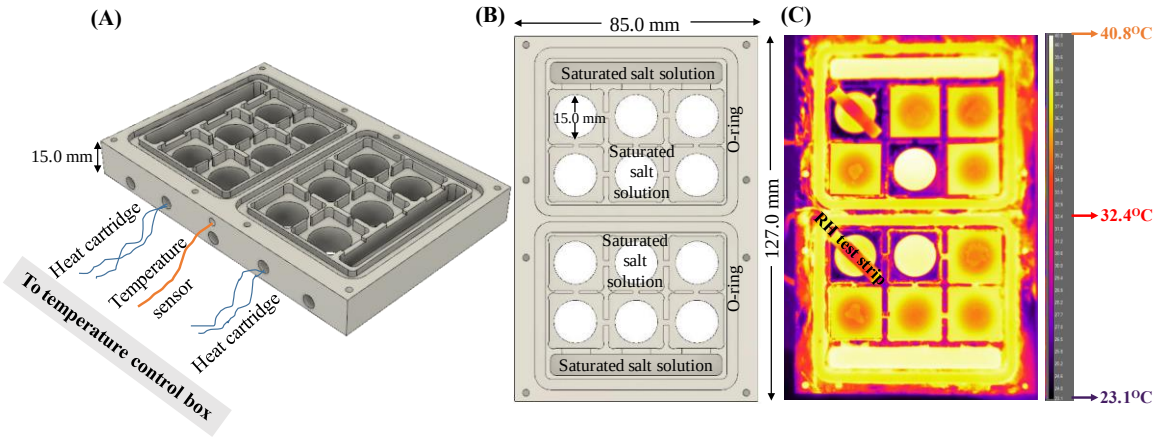

Figure 5.1. (A,B) CEiST design, (C) IR thermal image of CEiST for validation of set temperature at 40^{O}C.

Accelerated stability tests were performed using a SONICC microscope from Formulatrix (Bedford MA) for SHG imaging that was modified in house for epi detection.[29] For the *in situ* stability testing, samples in the CEiST chamber were maintained at an elevated temperature and humidity during SHG imaging. For samples maintained in the standard stability chamber, aliquots were sampled at select time points, analyzed by SHG under ambient conditions, and then discarded. The time from stability chamber removal through testing was about 10 minutes. Experiments were performed using ~200 mW excitation laser power at the sample and 890 ms exposure time, repeated every hour (duty cycle of 2.8×10^{-4}). SHG was measured in the transmission direction due to the high transparency of samples in the CEiST through deliquescence of the ASD. SHG was collected in the epi direction for powdered samples before being subjected to elevated temperature and humidity. For samples within the standard chamber, three fields of view were used for each time point. For samples within the CEiST, several fields of view were selected from each of 3 wells prepared for each ASD.

5.3 Results and Discussion

The performance of the CEiST was evaluated relative to a conventional temperature and humidity controlled chamber through side-by-side comparisons of accelerated stability testing of 15% DL (w/w) ritonavir ASDs with HME at 50°C/75%RH, the results of which are summarized in Figure 5.2. The amorphous excipients present in the HME ASDs did not produce significant coherent SHG signal. In contrast, ritonavir crystals adopted an SHG-active non-centrosymmetric lattice upon crystallization, enabling selective detection of crystalline ritonavir in HME ASDs using a particle counting algorithm.[104] SHG images at four representative time points are shown in Figure 5.2A for ASDs stored in a standard chamber at elevated temperature and humidity, and Figure 5.2B for ASDs stored in the CEiST under identical target conditions. For quantitative comparison of ritonavir crystallization between the two platforms, the average crystal area at each time point was recovered by particle counting, shown in Figure 5.2C. The error bars in Figure 5.2C represent the standard deviations of three fields of view for each time point. The SHG micrographs and the average crystal areas observed for both the standard chamber and the CEiST platform were in excellent agreement, suggesting that the conditions produced in the CEiST platform are representative of those experienced in conventional temperature and humidity controlled chambers.

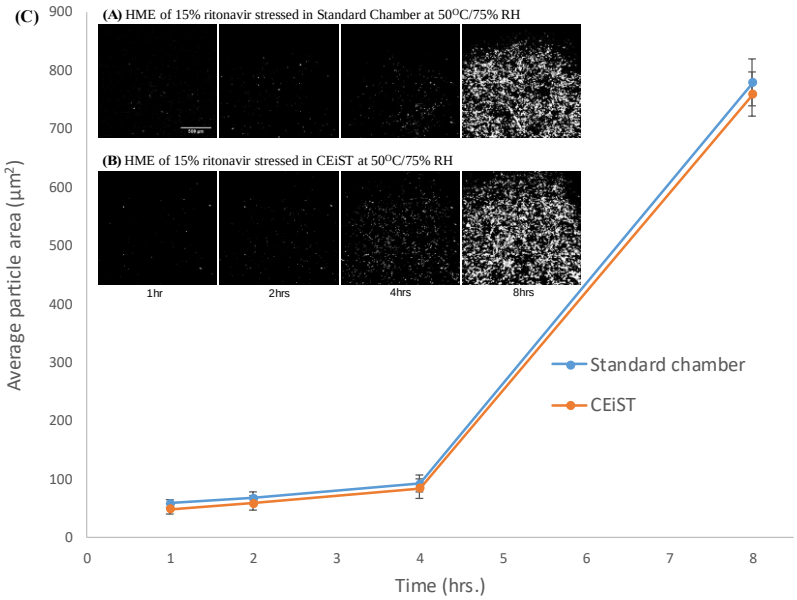

Figure 5.2. SHG images for time-dependent crystal growth of 15% HME ritonavir in (A) standard chamber, and in (B) CEiST. (C) The plot for average particle areas shows good agreement between the two different methods.

Using the CEiST platform, 10 trials of *in situ* accelerated stability testing were run in parallel for ritonavir crystallization in different ASDs at 50°C and 75% RH. The ASDs were prepared with different components and different manufacturing techniques (see Experimental Methods). The ASD powder samples were examined by SHG microscopy and initially showed no detectable epi-SHG signal (i.e., no continuous regions of interest with at least 3 contiguous pixels of at least 3 counts). From previous studies using SHG to interrogate ASDs, this criterion corresponds to a lower limit of detection of 10 ppm crystallinity[29], indicating that the initial crystallinity in all cases was less than this lower limit of detection.

The SHG images and corresponding bright field images were automatically collected every hour starting from 0 to 48 hours. Four sets of representative SHG images at five different time points are shown in Figure 5.3. All of the images are shown with the same brightness scale for comparison. Based on the time-dependent SHG images, the incorporation of surfactant (span 20) increased the ritonavir nucleation rate and crystal growth rate in ASDs. In this case, the addition of span 20 resulted in more crystals and larger crystal size in accelerated stability testing, consistent with the presence of span 20 significantly reducing the stability of ritonavir against crystal formation in both hot melt extruded and spray dried ASDs. Compared with SDD ASDs, HME

samples showed a greater number of crystals and lower induction times in the accelerated stability testing.

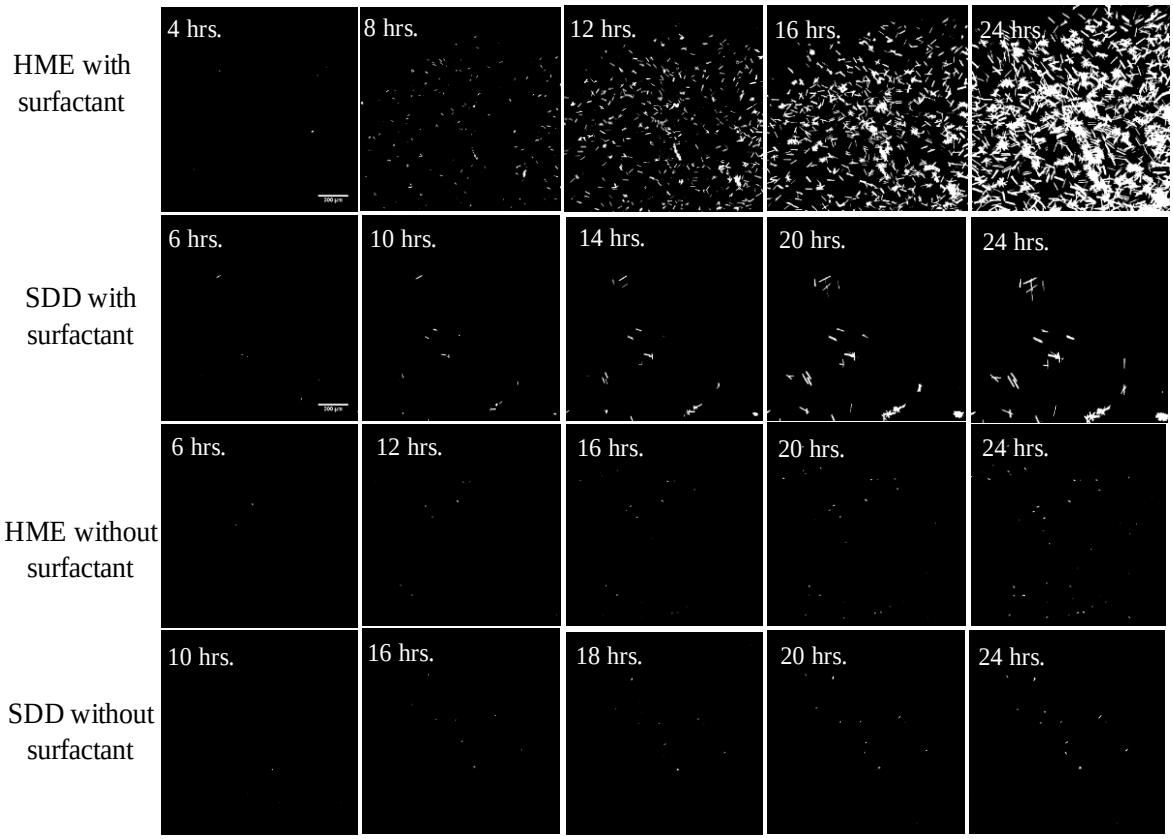

Figure 5.3. Time dependent SHG micrographs of 15% ritonavir ASDs stressed in CEiST at 50^{O}C/75%RH.

When accelerated stability testing was performed by using the standard temperature and humidity control chamber, the sample aliquots were taken out of the controlled environment to enable SHG imaging under ambient conditions. Since temperature and humidity cycling can significantly change the crystallization kinetics, all the samples using the standard chamber were discarded following SHG imaging. The perturbations associated with temperature cycling are attributed to a two-step process: i) increase in supersaturation upon cooling to room temperature, resulting in increased nucleation rate, followed by ii) increased diffusion upon return to elevated temperature and humidity, resulting in increased crystal growth rates. Multiple aliquots of sample were therefore required to collect images at different time points using conventional stability chambers to avoid kinetic artifacts from temperature cycling. This practice was in stark contrast to

measurements performed using the CEiST system, which supported continuous monitoring of the same fields of view within a sample under controlled conditions.

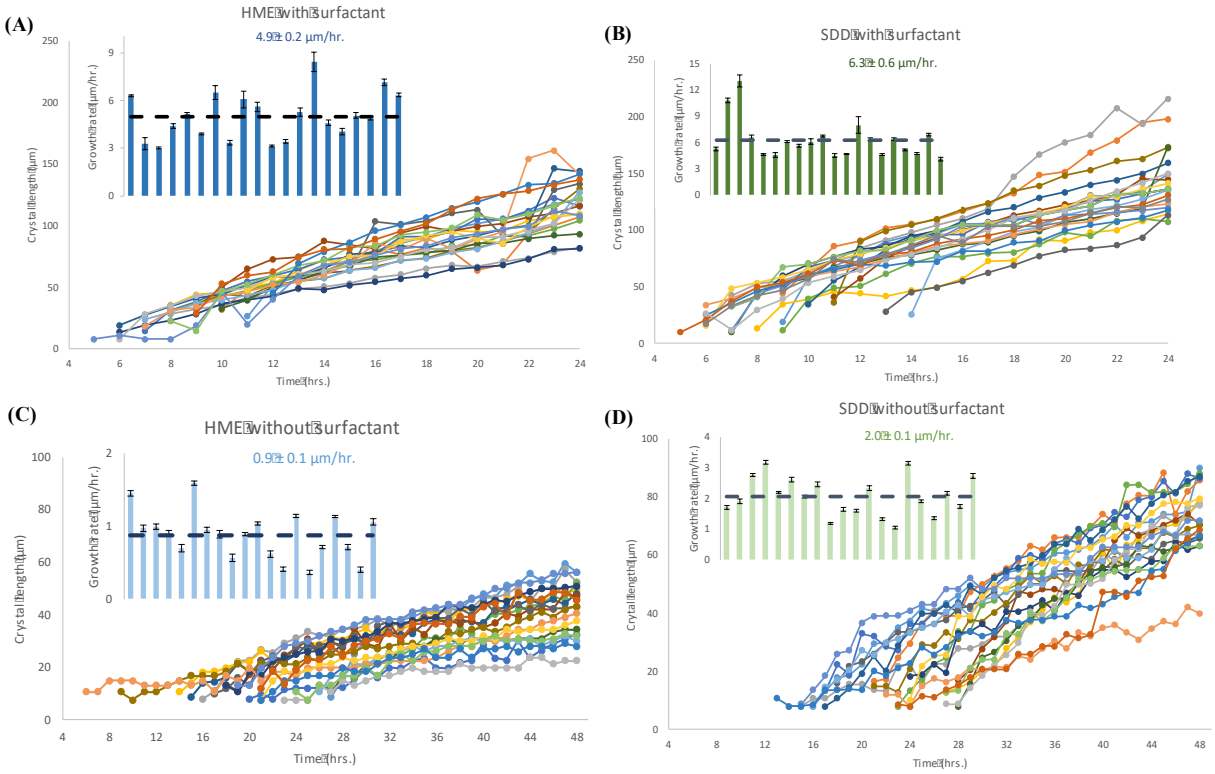

Figure 5.4. Individual crystal growth distribution in the CEiST for (A) HME with surfactant, (B) SDD with surfactant, (C) HME without surfactant, and (D) SDD without surfactant. Each plot has 20 different crystals tracked along the entire time trace and selected from different FOVs. The inset in each plot shows the dispersion in growth rates with the average growth rates shown in each plot as dashed line.

For each sample in the CEiST system, single-particle tracking was performed to monitor the growth rates of individual particles, representative results of which are shown in Figure 5.4A, B, C and D, selected from 4-6 different fields of view. The long axes of the needle-like ritonavir crystals (Form II) were used to quantify crystal size. The dispersion in crystal growth rates is shown in the inset plots of Figure 5.4. For individual crystals, error bars in the growth rates were assessed from the standard error of the slope of crystal size versus time. From inspection of the histograms of single crystal growth rates and the standard errors, it is clear that the dispersion in growth rates exceeds experimental uncertainties, and therefore reflects an intrinsic diversity in single crystal growth kinetics within the samples.

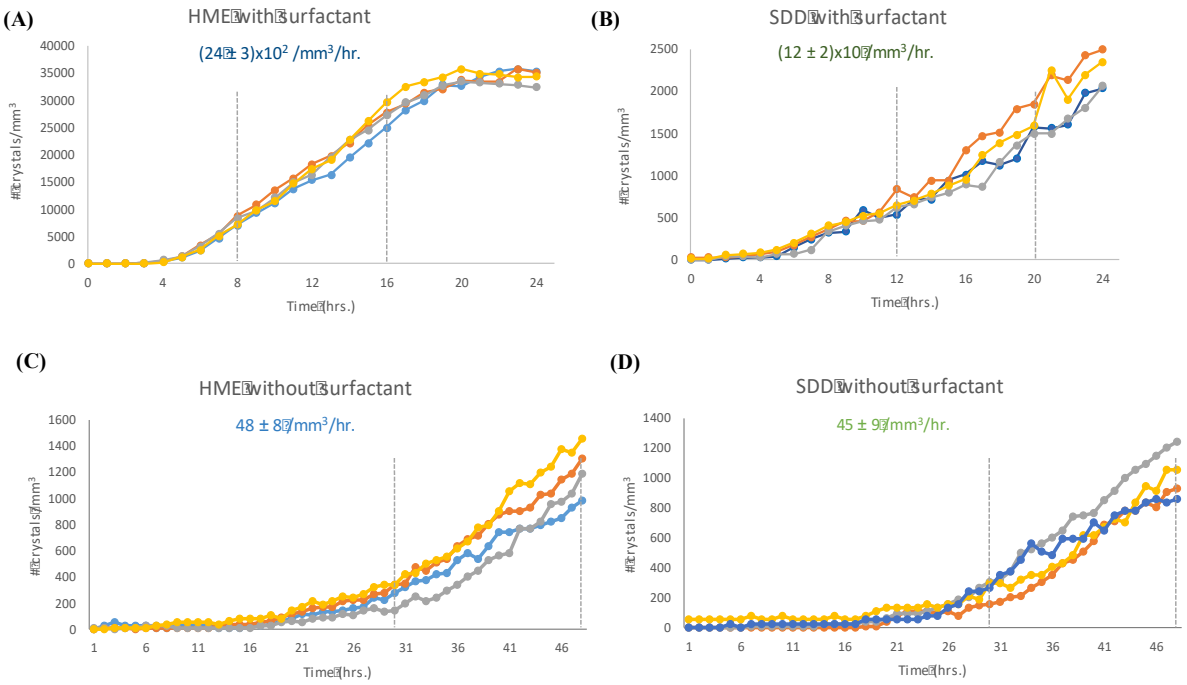

Figure 5.5. Average nucleation rates and single FoV trajectories in the CEiST for (A) HME with surfactant, (B) SDD with surfactant, (C) HME without surfactant, and (D) SDD without surfactant.

Single-particle tracking enabled by the CEiST platform provided substantial signal to noise benefits in nucleation kinetics as well. The average nucleation rates were found from the linear growth regime shown in Figure 5.5 A, B, C and D by linear fitting of nucleation events from four different fields of view. The uncertainties reported in each plot arise from the variabilities of the fields of view. The linear region for fitting was marked by the dashed line. The nucleation rate in HME ASDs in Figure 5.5A is one order of magnitude higher than in SDD shown in Figure 5.5B, in the presence of 10% span 20 in the ASDs. The residual nuclei present in HME ASDs might be responsible for producing this higher nucleation rate. However, without the presence of span 20, the ritonavir nucleation rates are similar in both HME and SDD at the RH and temperatures evaluated.

The substantial improvement in signal to noise for nucleation rate determination in CEiST can be understood considering the Poisson statistics associated with crystal genesis in combination with the sensitivity of SHG imaging to support single particle tracking. Nucleation rates using a standard stability chamber were calculated from the differences in the number of crystals between multiple independent samples analyzed at different time-points. Because each sample is

statistically independent, the number of crystals in any given field of view is given by a Poisson-distribution. As a result, the nucleation rate is generated from the difference between two Poisson-distributed numbers acquired at different time-points. In the linear kinetics regime, the number of previously nucleated crystals contributes to the uncertainty in the number of new particles, rapidly degrading the precision to which the number of new particles can be determined based on Poisson statistics. In contrast, the nucleation rates in the CEiST chamber were calculated from the differences in the numbers of new crystals *within the same single FoV*, removing all statistical uncertainties regarding the number of pre-existing crystals. As such, uncertainty in the nucleation rate is defined only by the Poisson statistics for the number of new particles within a given FoV. The signal to noise advantage associated with nucleation rates determined from analysis of single samples versus stochastic sampling is shown in Figure 5.6. Following the initial onset of nucleation, Poisson-distributed uncertainties in the differences in particle numbers between independent samples rapidly degrade the precision to which nucleation rates can be determined. However, no such statistical loss in SNR is expected from repeated analysis of a single FoV.

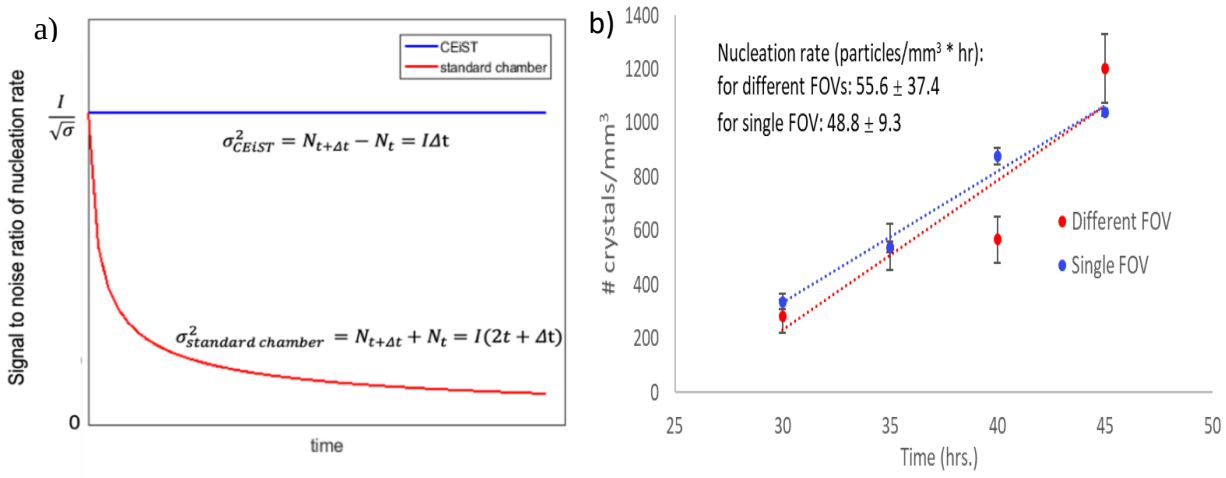

Figure 5.6. In a), the anticipated signal to noise ratio of nucleation rate for *in situ* vs conventional stability testing based on the Poisson statistics of crystal counting. I: nucleation rate, σ: uncertainty of nucleation rate based on Poisson statistics, N_t: number of crystals at time t. In b) A comparison between the results from a standard chamber and the CEiST. The different FOV represents the standard chamber where 4 time points were taken from 4 different repititions of the same experiment, and the single FOV is from a single experiment in the CEiST.

Interestingly, the SNR improvement afforded by single particle tracking pairing SHG microscopy with the CEiST platform provides a simultaneous advantage in reducing sample volume requirements. Stability testing of pharmaceutical formulations can extend over several weeks, or months, or even years, for each of potentially many different formulation candidates.[30, 105] The temperature cycling complication coupled with the Poisson statistics limitations associated with crystal analysis pose cost challenges associated with archiving large volumes of identical replicate samples in controlled environments for testing times spanning multiple months or years. Continuous *in situ* monitoring of a single field of view over the entire time-course of a stability assessment (e.g., by SHG microscopy) provides reduction in sample volume requirements proportional to the number of time-points used for kinetics assessments. For example, in the present study with up to 48 time-points recorded for a given sample, the total assay volume is correspondingly reduced up to 48-fold.

The collective results of the single-particle tracking experiments provide insights into the molecular connections between stability, method of preparation, and composition of ASDs. The higher observed crystal growth rate in SDD relative to HME ASDs suggests a fundamental difference in the molecular diffusion coefficient within the matrices, as the ritonavir growth rate is diffusion limited in this regime. The origin of this disparity in diffusion coefficients may potentially be attributed to the desolvation step in SDD generation, which may potentially produce a higher density of microscopic voids in the final products and higher molecular diffusion. Presence of Span 20 in ASD formulations of ritonavir contributes to processability, but dramatically increases molecular diffusion, with corresponding increases in single crystal growth rates. Specifically, the surfactant Span 20 increased the crystal growth rate by ~5 times for HME and ~3 times for SDD.

The surfactant Span 20 induced ~50-fold and ~20-fold changes in nucleation rates for HME (2400 ± 300 to 48 ± 8 particles/mm^3*hr) and SDD (120 ± 20 to 45 ± 9 particles/mm^3*hr), respectively. The nucleation kinetics are also distinctly different between SDD and HME ASDs in the presence of span 20, with nucleation rates about an order of magnitude higher in HME. This difference in nucleation rate may potentially arise from the presence of residual nuclei within the melt in the HME materials from incomplete melting.[106] Optimization of conditions for HME preparation strikes a balance between the competing desires for higher temperatures to remove residual nuclei and lower temperatures to minimize pyrolysis. As such, the presence of trace

residual nuclei within the HME is arguably more likely than in the SDD materials, consistent with the observations made by single particle tracking by SHG microscopy.

Recovery of the crystal growth rate distribution from single particle tracking suggests the presence of subtle but significant heterogeneity within the samples at microscopic scales. From inspection of the individual single particle growth curves in Figures 4, it is clear that the particle-to-particle differences in growth rates exceed experimental uncertainties of the fits, indicating that the differences are statistically significant. Several mechanisms were considered for potentially explaining the observed variance in crystal growth rates. Ritonavir is well known to adopt multiple crystal polymorphs, each of which would presumably adopt unique growth kinetics. However, previous studies of similarly prepared ritonavir samples confirmed by IR and XRD the exclusive presence of Form II.[30] Furthermore, the ritonavir crystals all exhibited similar aspect ratios and crystal habits, consistent with expectations for the presence of a single crystal form. As an alternative explanation for the variance in single particle growth kinetics, the influence of crystal orientation was considered. Experiments were performed in which crystals serving as seeds were placed on the surface of a 15% ritonavir HME film, such that the rod-like crystals were similarly oriented with the long axed within the surface plane. Despite the monidispersity in orientation, individual crystals still produced statistically distinct growth rates, suggesting that orientation was not a primary factor for the variance in single particle growth kinetics (Figure S3). This intrinsic variability in growth rates for nominally identical crystal forms suggests heterogeneity in local diffusivity within the surrounding matrix. The growth rate dispersion might result from subtle variation in local density, hydrophobicity, chemical composition, etc. The diversity in growth rates, and correspondingly diversity in local environments is similar between different formulations.

5.4 Conclusions

The CEiST platform developed in this work enabled single particle tracking during accelerated stability testing of ritonavir ASDs by SHG microscopy. The high selectivity of SHG to crystalline content provides high-contrast images over a large dynamic range of crystallinity for kinetics analysis. The advantage of monitoring the same field of view over time facilitated substantial signal to noise improvements for nucleation and growth rate assessments, supported single-particle tracking, and reduced the sample volume requirements by ~50 fold. From the single-particle tracking measurements by SHG microscopy, the heterogeneity in crystal growth

rates within the ASDs suggests subtle but non-negligible local diversity in physical and/or chemical characteristics of the sample.

CHAPTER 6. DISPARITIES IN CRYSTAL GROWTH AND NUCLEATION KINETICS IN EXPOSED VERSUS BURIED CRYSTALS

6.1 Introduction

Solid state forms of active pharmaceutical ingredients (APIs) significantly affect the oral bioavailability in the final dosage form due to low aqueous solubility.[23-24] Amorphous solid dispersions (ASDs) have been used to increase bioavailability of low solubility APIs by casting the API in an amorphous glassy polymer matrix to prevent crystallization at supersaturated states. Intimate mixing in a glassy state with the pharmaceutically accepted excipients traps the API kinetically in an amorphous form, which is typically a metastable state with increased solubility, free energy, and dissolution rate.[93, 107] However, a primary challenge is assuring long-term physical stability in the amorphous state, as the amorphous forms have increased chemical and thermodynamic properties compared to crystalline analogs. Although there is increasing bioavailability, there is crystal formation within the API due to the chemical and physical instability of amorphous solids, leading to crystal growth and crystal nucleation within the API. Crystal formation within the API negatively influences the drug potency and stability, and consequently decreases the shelf life of the final form of the drug.[23, 107] Measurements capable of informing observed crystal growth at the early stages of formation at conditions of ASD storage can reduce the overall timeframe required for evaluating stability, both at the surface of the API and in the bulk.[23]

There are many arguments about the mechanism of crystal growth on the surface of APIs in ASDs in recent studies, with comparisons to crystal growth in the bulk.[101] One is the tension-release model: since the density of crystals are higher than amorphous glass, it results in stress and strain effects in bulk that are much stronger than surface, which causes faster crystal nucleation and growth on the surface.[108] But Tanaka argues that crystal formation in a glassy material induces stress around the crystal, leading to a volume contraction upon the crystal. As the volume of particles of the glassy material surrounding the crystal increases relative to the volume of the crystal, there is an increase in mobility, leading to further crystallization. Based on this theory, crystal growth on surfaces will be slower than in bulk, as there are significantly more glassy material particles surrounding crystals in the bulk than on the surface.[109] Another well-known model is the surface mobility model: The higher crystal growth rate on the surface is due to higher

mobility of surface molecules.[110-111] In addition, the higher mobility of surface molecules also results in a faster nucleation rate. The third model is based on different molecular packing on the surface versus in bulk.[112] Further complicating the analyses, additives can profoundly impact crystallization kinetics, the effects of which have the potential to be distinctly different for surface versus bulk crystallization.[113] Diffusion-limited models for crystal growth kinetics in the presence of additives do not adequately capture the observed trends, with significant increases in surface crystallization rates routinely reported in amorphous molecular glasses.[114-115] Additional measurement tools capable of sensitively and independently interrogation of surface and bulk crystal growth kinetics and mechanisms may help address lingering ambiguities between these two growth conditions.

A diverse suite of tools routinely used for accelerated stability testing of APIs in ASDs has the potential to help address the mechanisms driving surface and bulk crystal formation. However, most accelerated stability tests are performed by using powdered pharmaceutical samples,[107] which only provided average information of the entire sample and makes it difficult to reveal API crystallization at different locations. API crystallization kinetics in the bulk have shown to be different from that on the surface. For example, Zhu, et al. demonstrated that crystal growth rate at the surface of pure amorphous griseofulvin is 10- to 100-fold faster than that in the bulk. Zhu attributed the difference to the fact that the surface crystallization rate was much less temperature dependent than the bulk under the glass transition temperature because of uniformity in particle size distribution in the surface.[115] In addition, Yu et al. reported differences in surface and bulk crystallization rates for amorphous nifedipine (NIF) melted with small relative concentrations of polyvinylpyrrolidone (PVP) of different molecular weights to make a two-component amorphous system.[114] The authors reported strong inhibition of crystallization in the bulk from PVP, with a much weaker effect observed for surface crystallization rates. Many explanations were considered to explain the differences in crystallization kinetics, such as PVP concentration being lower at the surface than in bulk, and the hypothesized higher mobility at the surface resulting in an reduced inhibitory impact of the PVP on crystal growth.[114] As the crystallization for bulk versus surface of the drug is still poorly understood, accelerated stability testing to study the spatial heterogeneity of stability of the ASDs is validated, as assessing and understanding the crystal growth distribution within the final dosage form of the API informs us about physical instability of the drug, and therefore, the bioavailability.[24, 114] Most notably, these previous studies were performed either with

purely or predominantly API, which may not be representative of behaviors arising in amorphous solid dispersions, in which the API is typically the minority species.

Several analytical techniques are commonly used for accelerated stability testing that can potentially be brought to bear for surface versus bulk analysis, including polarized light microscopy (PLM), powder X-ray diffraction (PXRD), Raman spectroscopy, IR spectroscopy, solid-state NMR spectroscopy, etc. Even though PLM has been used to detect crystallinity and determine crystal nucleation rates,[116] the spatial resolution is hindered by diffraction limitation.[99, 106] Although PXRD is hailed as the "gold standard", as it can detect morphology and degree of crystallinity for API characterization and identification, the sample is typically a microcrystalline powder that has gone through meticulous sample preparation in order to get appropriate particle size, orientation, and thickness. In addition, PXRD obtains broader reflections and lower absolute intensities for smaller average crystallite size and for decreased crystal quality.[106, 117] Although spectroscopic methods, like IR[118-119] and Raman[119-120], can obtain raw material crystalline and polymorph identification in a non-destructive manner, these methods are more conducive to investigate crystallinity on the surface, with little studies have being done in the bulk. For example, although Bhatia et al. was able to use high-resolution low frequency Raman in order to analyze short-range structure determine Mo-O stoichiometry for amorphous and crystalline films of molybdenum trioxide, it was unable to analyze bulk and XRD had to be implemented with Raman in order to observe at bulk powder nanocrystal structure.[121] In addition, even though the new spectroscopic improvements concerning ssNMR improved sensitivity in order to give unique insights into microscopic and macroscopic structure of APIs, these studies have been mainly applied to microcrystalline solids from grinded commercial tablets, leading to average ensemble measurements.[122] Similar to the techniques discussed, most other benchtop methods do not have great penetration or high enough sensitivity to measure trace crystallinity within bulk sample. Thakral *et al.* used synchrotron X-ray diffractometry to quantify crystallization from surface to core of a tablet, which enabled investigation of heterogeneous crystallization in a tablet.[123] More recently, Suryanarayanan et al. used synchrotron X-ray diffractometry in order to detect differences in crystallization at surface, and crystallization in the bulk and non-nucleated surfaces using the broadening of the crystallization exotherm for compressed tablets of amorphous sucrose and sucrose-PVP.[124] However, X-ray diffraction patterns cannot provide the information to assess nucleation and crystal growth kinetics. Furthermore, access to a synchrotron X-ray light source is

not commonly available for pharmaceutical formulation development. Overall, the techniques obtain ensemble-average measurements, which lose microscopic information such as crystal nucleation rates and kinetic growth rates, and do not have sensitive detection of crystallinity deep within tablets and powders.[23-24]

Recently, nonlinear optical microscopy has emerged with potential as an analytical tool for quantitative analysis of trace crystallinity within pharmaceutical materials. Nonlinear optical microscopy has been used to probe initial stages of crystal formation, as it provides an advantage for pharmaceutical research with temporal sensitivity, spatial selectivity due to non-destructive nonlinear excitation, and increased imaging speed for dynamic processes.[21, 23, 125] Non-linear optical measurements enable the recovery of crystal growth rates within powders or thin films that have $\leq 1\%$ crystallinity.[23-24, 126] Specifically, second harmonic generation (SHG) is an application of nonlinear optics that results in a frequency doubling of light upon interaction of non-centrosymmetric crystals, where the interactions of the photons lead to resonant enahancement.[24, 125] SHG is able to quantify API crystallization with detection limits in the parts per million regime, in comparison with competing techniques that have detection limits around ~10% crystallinity.[21] The primary advantage of SHG is the increase in signal-to-noise, which arises from the suppression of the background since the disordered, amorphous material of the ASD does not produce coherent signal, leading to chemically selective visualization of the crystallites in the complex mixed system.[23, 28, 125] With the improvement in signal-to-noise, SHG allows for dynamic processes, such as crystallization, to be followed in real time. Therefore, quantitative determination of crystal nucleation, growth kinetics and macroscopic crystallization rates from a single set of measurements can be obtained with improvement in lower limits of detection and greater linear dynamic range,[23] independently supported by Podzemna et al. with measuring crystal growth kinetics and nucleation kinetic rates of germanium disulfide.[127] SHG serves as a sensitive and selective tool for detection and characterization of both surface and bulk materials.[23]

In this work, SHG microscopy was performed within the bulk and at the surface of seeded ritonavir crystals in copovidone for high-contrast quantitative analysis of crystallization kinetics. As SHG is highly selective for crystals of homochiral molecules, quantitative analysis of crystal growth on a per-particle basis can be obtained. As such, growth rates were independently determined from "time-lapsed" image analysis over 48 hours for individual crystals. A controlled environment for in situ stability testing (CEiST) chamber was used, which allowed for continuous

monitoring of the individual crystal over 48 hours under 50ºC and 75% RH, typical of previous ASD analysis, as the sensitive and non-destructive capabilities of SHG were heightened.[19] As SHG microscopy monitored the CEiST in the same fields of view (FoV) over time, the signal-to-noise of crystal growth rate was significantly improved with a lower number of samples.[19] Differences observed in growth rate kinetics from surfaces versus the bulk were interpreted in terms of supersaturation and molecular mobility

6.2 Methods

ASD samples of ritonavir (15%), sorbitan monolaurate (10%), copovidone (74%), and colloidal silicon dioxide (1%) were prepared as hot melt extrudates (HMEs). The extrudates were made using a lab scale Thermo Scientific® Process 11 Hygienic Parallel twin-screw extruder fed gravimetrically at 0.750 kg/h with a screw speed of 250 rpm. Temperatures in the heating zones ranged from 15 ºC to 150 ºC. The extrudates were milled using a Fitzmill L1A at 6000 rpm and a screen size of 0.033 in round hole. Samples without the sorbitan monolaurate were also made, in which the copovidone weight percent was increased to 84%.

The Specac Atlas™ Constant Thickness Film Maker Accessory was implemented in order to make thin films of these ASD powders, which would represent samples with seeded crystals on the surface. A sample of 50-60 mg of the ASD was centered and dispersed between two pieces of aluminum foil, which were previously cut with PunchBunch SlimLock™ Medium Punch – Circle 1 inch. The Film Maker Accessory was then set to a temperature of 115 ºC, using the D spacer (100 micron). After the sample was heated up for 5 minutes, the Film Maker Accessory was then put under a pressure of 4 tons. After 10 minutes under presure, the temperature on the Film Maker Accessary was decreased to 65ºC while the pressure stayed constant at 4 tons. When the Film Maker Accessary reached the 65 ºC, the film was removed from the apparatus and the aluminum foil, creating a single thin ASD film. Single crystals were manually placed under a microscope onto the film.

The thin films containing the seeded crystals could undergo further sample preparation in order to obtain a sample representation for seeded crystals in the bulk. The surface film with seeded crystal was placed back into the Film Maker Accessory, and a film without seeded crystals covered it, depicting a “sandwich” (film-crystal-film), in which the “sandwich” was again placed between two pieces of aluminum foil. The Film Maker Accessory was set to a temperatures of 98

ºC, while using the E spacer (250 micron), and pressurized to a pressure of 1.25 tons. As with a single thin film, the temperature and pressure remained constant for 10 minutes, with the temperature dropping to 65 ºC after the time passed. When the Film Maker Accessary reached the 65 ºC, the film was removed from the apparatus and the aluminum foil, creating a film that contained seeded crystals in bulk. For both surface and bulk, the thin films were carefully cut and placed into the CEiSt, such that the CEiST chamber only contained areas which consisted of crystals. Information on the CEiST's design is described in more detail in previous work.[128]

Accelerated stability testing was performed using a SONICC (Second Order for Non-linear Imaging for Chiral Crystals) microscope from Formulatrix (Bedford, MA) for SHG imaging. The SONICC microscope was modified in-house such that the sample holder was switched for a 3D printed holder modified to mount the CEiST. The relative humidity was held at 75% and the temperature kept at 50°C within the CEiST chamber throughout the duration of the experiment. Samples were then imaged over a course of 48 hours, with data being collected every hour in the same field of view for each well using 200 mW excitation power with an exposure time of 447 ms for every hour. In the first two hours, data were also collected using 350 mW excitation power, with an exposure time of 894 ms for the first two hours.

Data analysis was primarily done using FIJI (FIJI Is Just ImageJ). A crystal was manually tracked through the 48 images (one image collected for every hour the experiment ran), and the area and the perimeter of each monitored crystal were obtained through the plug-in features of FIJI. Using the two known parameters and the equations for area and perimeter, the length was calculated. For columnar crystals, the length of the crystal was then plotted over the course of 48 hours for 20 bulk crystals and 20 single surface crystals. In addition, the length for 20 radiating crystals were calculated by assuming a circular area, and relating single particle growth rate to the fast axis growth along the diameter. Solving for the diameter from the area provided the length and subsequent growth rates for the radially growing crystals.

6.3 Results and Discussion

The CEiST multi-well chamber was used to determine the growth rates of individual ritonavir crystals seeded onto 'open faced' and 'sandwiched' samples. Figure 6.1 shows an example of crystal growth on the open faced samples and the sandwiched samples over a 48-hour time period. Crystal growth can be seen primarily along the long axis of the rod-like crystals in

both cases. However, crystals in open faced samples show a radial growth habit, while sandwiched crystals show a columnar growth habit.

This difference in crystal habit is tentatively attributed to a higher water content at the ASD

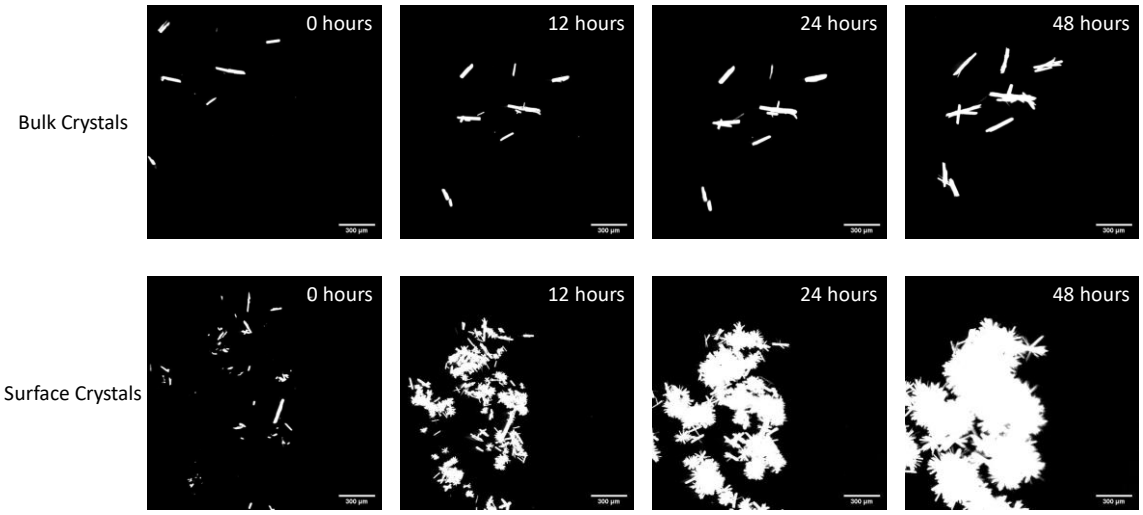

Figure 6.1. Images over time of seeded crystals pressed within bulk pharmaceutical formulation and seeded crystals on top of pressed pharmaceutical formulation.

surface relative to the bulk. Ritonavir is well-known to exhibit low aqueous solubility, suggesting that water adsorption or absorption at high RH would likely increase the supersaturation of ritonavir adjacent to the film surface. Local increases in surface supersaturation would promote a high crystalline defect density, which is a prerequisite for radial growth habits. This phenomenon of increasing nucleation/defect propagation leads to an increase in total crystallinity of the sample at the surface versus within the bulk as a consequence of radial versus columnar growth habits, respectively.

Single-particle trajectories are shown in Figure 6.2, along with uncertainties in the fits. For both the bulk and surface regions, the particle-to-particle variance exceeds the errors of the fits, suggesting statistically significant differences. In the bulk, relatively minor differences were observed, similar in magnitude to these reported previously[128] and attributed to subtle differences in local environments within the glassy matrix producing minor but measurable differences in growth kinetics. In contrast, the differences in the growth rates of individual particles seeded at the surface exhibit clear evidence (Figure 6.2A) of a bimodal distribution of growth rates. Many of the crystals grow slowly (1.3 ± 0.4 μm/hr), while a few grow at a significantly faster rate ($4.8 \pm$

1.8 μm/hr). The faster growing particles tend to nucleate during the experiments rather than emerging from obvious seed crystals.

Additional tests of the measured aspect ratio were performed to determine whether the slower and faster growing particles at the surface were statistically significantly different. The

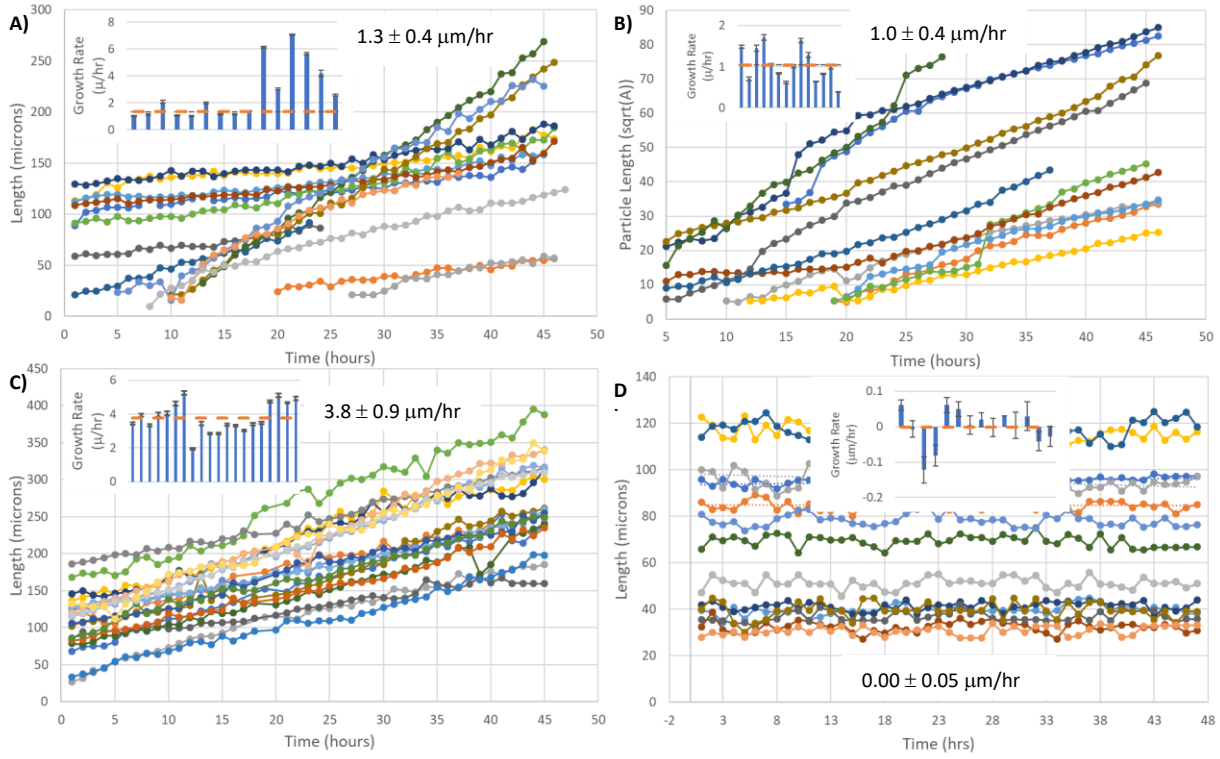

Figure 6.2. Individual crystal growth distributions for A) Single crystals on the surface, B) radiating crystal growth on the surface, C) bulk crystal growth, and D) crystals in a low RH environment. Each plot has 14+ different crystals selected from different fields of view, and the inset in each plot shows the crystal growth rate distributions with the average shown as a dashed line.

aspect ratios were measured to be 4.7 ± 1.5 for the slow particles and 8.8 ± 2.6 for the faster particles. The first of these two aspect ratios is statistically indistinguishable with analogous measurements for the bulk seeded crystals. However the faster particles nucleated during the experiment were statistically distinct from both within a confidence of 90%. Given these collective differences, the faster growing particles are tentatively attributed to a crystal form distinctly different from the crystal seeds used for surface vs. bulk growth rate analysis. As such, these outlying crystal forms were excluded from subsequent analysis of the differences in growth kinetics. It is worth noting the importance of single-particle growth rate analysis in order to enable

this assessment; ensemble averaged results would otherwise produce bias in the growth rates measured from crystals at the surface if the individual outlying particles were not excluded.

Interestingly, individual single-crystal growth rates are notably higher in the bulk than growth rates on the surface. This result is highlighted in Figure 6.2. The crystal growth rates for crystals within the bulk material were roughly three times those of crystals on the surface. The average crystal growth rate within the bulk is 3.8 μm/h with a standard deviation in growth rates from the histogram of ± 0.9 μm/h, while the average growth rate on the surface is 1.3 μm/h with a particle-to-particle standard deviation of μm/h. The apparent increase in crystallinity measured by volume for surface-seeded crystal growth in Figure 6.1 is largely a consequence of the higher volume occupied by radial growth relative to single-crystal columnar growth.

Several possible explanations for the disparity in surface versus bulk growth rates were considered, including being due to the difference in water content at the surface versus in bulk material. Under diffusion limited conditions, a gradient in water content could arise within the polymer matrix, with higher water content closer to the surface of the ASD film. If higher water content correlates with slower diffusion within the polymer, bulk growth rates at lower water contents would be expected to exhibit slower crystal growth rates. In studies of amorphous isomalt with high molecular weight polymeric additives, Carle et al. found that increasing water content led to increasing viscosity at constant (T-Tg).[129] With the polymer excipient serving as being the high molecular additive in this experiment, the explanation of higher water absorption leading to higher viscosity and lower molecular mobility would offer one possible explanation for the higher growth rate of bulk crystals versus surface crystals. However, Carle et al. concluded that evaluation of the effect of water on the viscosity of melts were challenging to isolate, as the changes in the amorphous state can also differ based on the molecular weight of the polymeric substances.[129] In contrast, other studies of ASD materials more closely matched to those investigated herein, higher water absorption was observed to decrease viscosity and increase mobility in the amorphous state with different polymer additives.[130-131] Under these conditions, one would expect significantly faster growth rates for crystals at the surface relative to the bulk.

A control experiment was performed to assess the impact of water content (Figure 6.2D), in which the CEiST chamber was brought to 50°C and 0% RH by use of desiccant. Particles seeded and maintained at low RH showed no significant crystal growth at the surface or within the bulk. As a consequence of this experiment, we conclude that increases in water content are likely to

correlate with increases in crystal growth rate. In this case, surface growth would be significantly faster at the surface than in the bulk in the presence of a gradient in water content, in direct opposition to the trends observed experimentally. Consequently, we concluded that the samples likely exhibit similar water content throughout the ASDs, given the relatively small but statistically significant differences in growth rates at both the surface and in bulk with elevated RH.

Possible differences in surface and bulk growth rates were also considered from geometric effects related to molecular diffusion. As illustrated in Figure 6.3, for sandwiched crystals, each

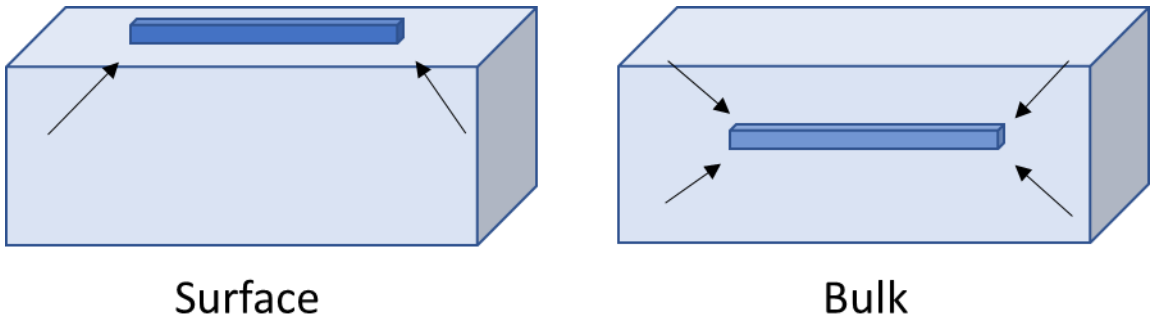

Figure 6.3. Illustration of the geometric effects on diffusion limited crystal growth.

crystal has access to material in all directions around it, while the "open faced" crystals seeded on the ASD surface only have access to material on the lower half that touches the ASD film. Since only half of the surface crystal is touching the ASD film in comparison to bulk crystals, a growth rate correction factor of 2:1 (bulk: surface) is expected.[132] Previous studies have incorporated this correction factor in surface chemical kinetics, as Olander proves when relating the linear velocity profile of a disk surface to the rate of weight loss of the germanium disk.[133] However, since the crystal rod is growing two faces along the fast axis, the growth rate difference should be applied to both ends, resulting in a growth rate correction factor of 4:1 (bulk: surface). This four-fold reduction in crystal growth rate at particle surfaces is in good qualitative agreement with the observed difference of ~3:1 in growth rate as shown in Figure 6.2. The slight but statistically significant deviation for surface growth rate (3:1 measured versus 4:1 predicted) is tentatively attributed to higher water content adsorbed to the surface, consistent with the arguments of the preceding paragraph.

The observations reported here indicating slower growth kinetics at ASD surfaces relative to the bulk is juxtaposed to numerous previous studies demonstrating enhanced crystal growth rates for APIs at surfaces relative to analogous bulk. As detailed in the Introduction, studies of amorphous griseofulvin,[115] amorphous nifedipine doped with small quantities (1-5%) of organic polymer polyvinylpyrrolidone[114] all exhibited faster surface growth relative to analogous bulk values. The notable difference in observed behaviors may arise from the disparity in mass fraction of API. The present studies were performed with only 15% API entrained within a glassy matrix, while previous studies characterized trends in materials with >95% API. These two different composition regimes may result in major differences in interactions driving crystal growth kinetics (e.g., molecular diffusion, internal energy barriers, heat dissipation, etc.). The previous studies with low doping are not representative of practical ASDs used in final dosage forms, as API loadings in the polymer matrix can approach 30-40%.[134] As such, the bulk-to-surface 4-fold difference observed in this study with 15% API is more representative of the kinetics expected in ASDs similar to those currently integrated into commercial final dosage forms.

6.4 Conclusions

We demonstrate single-particle tracking in a CEiST block to monitor crystal growth kinetics within bulk material and on the surface of ASDs. In the ritonavir/copovidone system explored, bulk crystal growth rates were found to be ~3-fold greater than similarly prepared seeded crsytals placed at the ASD film surface, with the bulk of the reduction attributed to an expected 4-fold reduction in growth rates from relatively simple geometric effects under diffusion limited growth conditions. Nevertheless, the radial surface crystal growth habit led to a higher total crystallinity than in the bulk, which exhibited exclusively columnar growth. Single particle tracking also enabled isolation of a second population of surface crystals exhibiting faster growth rates and higher aspect ratios than the seeded crystals, attributed to an alternative ritonavir crystal form. The collective results highlight the advantages of single particle tracking enabled by SHG microscopy of ASD materials; integration over all the individual particles masks the detail of disparities arising within the crystal populations depending on timing and location of crystal formation. Recovery of the single-particle information provides information for improving modeling and simulation of crystal growth rates and particle size distributions within ASD materials expected during storage and handling.

As one interesting example, increasing the surface areas of ASD particles within a formulation could lead to either faster or slower crystal growth depending on the interplay between geometric effect slowing growth and differences in crystal habit and/or crystal form that could encourage increases in overall crystallinity. Improved understanding/modeling of the local differences in API concentration and diffusion arising at the surface and within the bulk can lead to informed decision-making in formulation design. Assuming other ASDs exhibit qualitatively similar richness in particle-to-particle behaviors, SHG-enabled particle tracking in controlled environmental conditions may provide a broadly utilitarian framework for rational optimization of particulate conditions when preparing final dosage forms incorporating milled ASDs.

CHAPTER 7. HIGH THROUGHPUT IN SITU STABILITY TESTING

7.1 Introduction

The efficacy of a drug can be drastically affected by the solid-state form of the active pharmaceutical ingredient (API) within it.[6, 35-36] Pharmaceutical companies are required to conduct stability tests on final dosage forms in order to determine how long the API will be in an efficacious state to assign a shelf life.[30] This is particularly important in formulations where the API is not in its most stable state where the increased chemical and physical properties can lead to a change of state that may be less bioavailable.[11] Amorphous solid dispersions (ASDs) are one example of a formulation where the API is kinetically trapped in an amorphous state by being dispersed into a polymer matrix. The amorphous form of the API leads to a significant increase in bioavailability through an increase in apparent solubility, but also leads to stability concerns since the amorphous form is likely less stable than the crystalline. Stability testing is particularly important in understanding the crystal growth and nucleation kinetics of an ASD formulation and the manufacturing method used to make it. Hot melt extrusion is a common method for generating an ASD through dissolving the API into a melted polymer, but this method can lead to residual crystallinity in the ASD which can significantly impact long term stability.

Traditional stability testing can take months to years to perform at standard temperature and pressure conditions. As a consequence of the requirement to conduct stability tests on a large amount of different formulations and materials, the space requirement and cost associated with storage and performing conventional stability tests are high. Accelerated stability testing is a common way to decrease the time and storage requirements by elevating the temperature and relative humidity (RH) conditions applied to the samples and reducing the time required for stability measurements to be performed. Accelerated stability tests are typically doneby placing many samples into large stability chambers, and periodically taking a sample out and performing analytical tests to determine the changes in the formulation (i.e. crystal growth and nucleation). The most common analytical techniques used for stability tests are polarized light microscopy (PLM)[14], powder X-ray diffraction (PXRD)[15-17], infrared spectroscopy (IR)[19], and Raman spectroscopy[18]. Despite the widespread use of PLM for determining crystal growth and nucleation rates, it is hindered by the requirement of an optically transparent sample, difficulty in

quantification, and interference from occlusions, contaminants, and crystalline excipients. PLM is also difficult to integrate into fully automated analysis of crystallinity. PXRD is commonly considered the "gold standard" for trace crystallinity detection in the pharmaceutical industry but is unable to quantify at low crystallinity and requires significant rigorous sample preparation. In general, the listed analytical techniques have detection limits on the order of 1-5% which could be the entire drug loading of an ASD.[64] A technique which offers a lower detection limit and a large dynamic range would improvestability testing by increasing confidence in recovered kinetics parameters, lowering the sample requirements, and reducing the timeframe required for stability assessment.

Nonlinear optical imaging has the potential for providing the detection limits and dynamic range to fill this gap in crystal growth and nucleation kinetics measurements in stability testing. Nonlinear optics has recently gained traction in the pharmaceutical industry for sensitive detection and quantification of trace crystalline content within amorphous formulations.[21-26] Second harmonic generation (SHG) describes the coherent conversion of light to twice the frequency, which is symmetry-forbidden in centrosymmetric media but allowed in assemblies of lower symmetry, including the large majority of noncentrosymmetric crystals. The symmetry requirements of SHG allow for a near background free measurement of the crystalline fraction of an ASD during stability testing. Recently, SHG has been coupled with a miniaturized stability chamber to allow for *in situ* stability testing by Sarkar et al.[128] The ability to perform the stability testing on the same material over time rather than relying on separate sample aliquots periodically pulled from large stability chambers reduces the amount of material required for the testing proportional to the total amount of time points needed. While this method significantly reduces sample and time requirements for a stability test, the information that can be obtained from a single experiment is still limited by the conditions that can be used at one time.

In this work a high throughput version of the previous *in situ* method is development. The temperature and relative humidity array (TRHA) was designed to allow many different conditions to be explored at the same time while continuing to benefit from the *in situ* measurements. A temperature gradient is achieved across the platform and multiple liquid wells are used to provide an array of different relative humidity conditions at different temperatures. The increase in information that the TRHA provides can significantly decrease the time requirement for stability

assessment of final formulations as well as for new chemical entities (NCE) while providing information to inform predictive modeling.

7.2 Experimental Methods

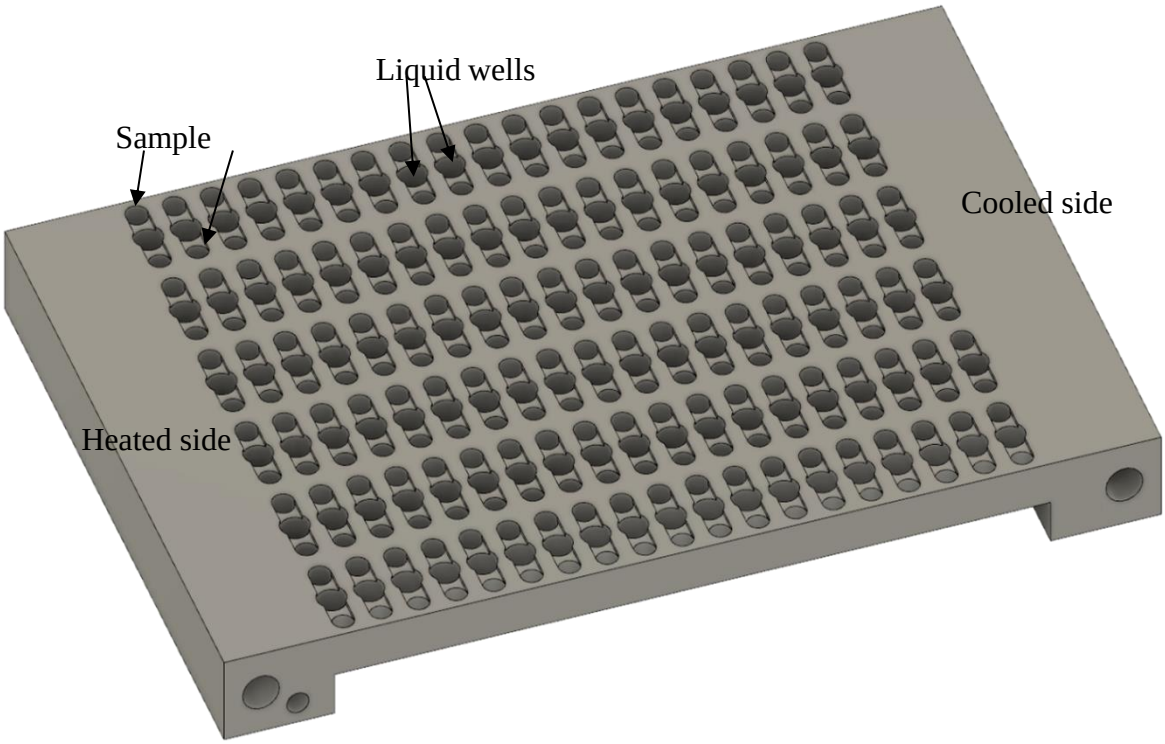

Figure 7.1. Illustration of the TRHA platform.

ASD samples of ritonavir (15%), sorbitan monolaurate (10%), copovidone (74%), and colloidal silicon dioxide (1%) were prepared as hot melt extrudates (HMEs) and spray dried dispersions (SDD). The extrudates were made using a lab scale Thermo Scientific® Process 11 Hygienic Parallel twin-screw extruder fed gravimetrically at 0.750 kg/h with a screw speed of 250 rpm. Temperatures in the heating zones ranged from 15 ºC to 150 ºC. The extrudates were milled using a Fitzmill L1A at 6000 rpm and a screen size of 0.033 in round hole. The ASDs by SDD were made using a Büchi® B-290 spray dryer with an inert loop using methanol as the solvent. The feed solution flow rate into the two-fluid nozzle (1.4 mm diameter) was 20 g/min, with

nitrogen atomizing gas. The nitrogen process gas was set to 30 kg/h. The inlet and outlet temperatures were 90 ºC and ~ 50 ºC, respectively, while the condenser was held at -20 ºC.

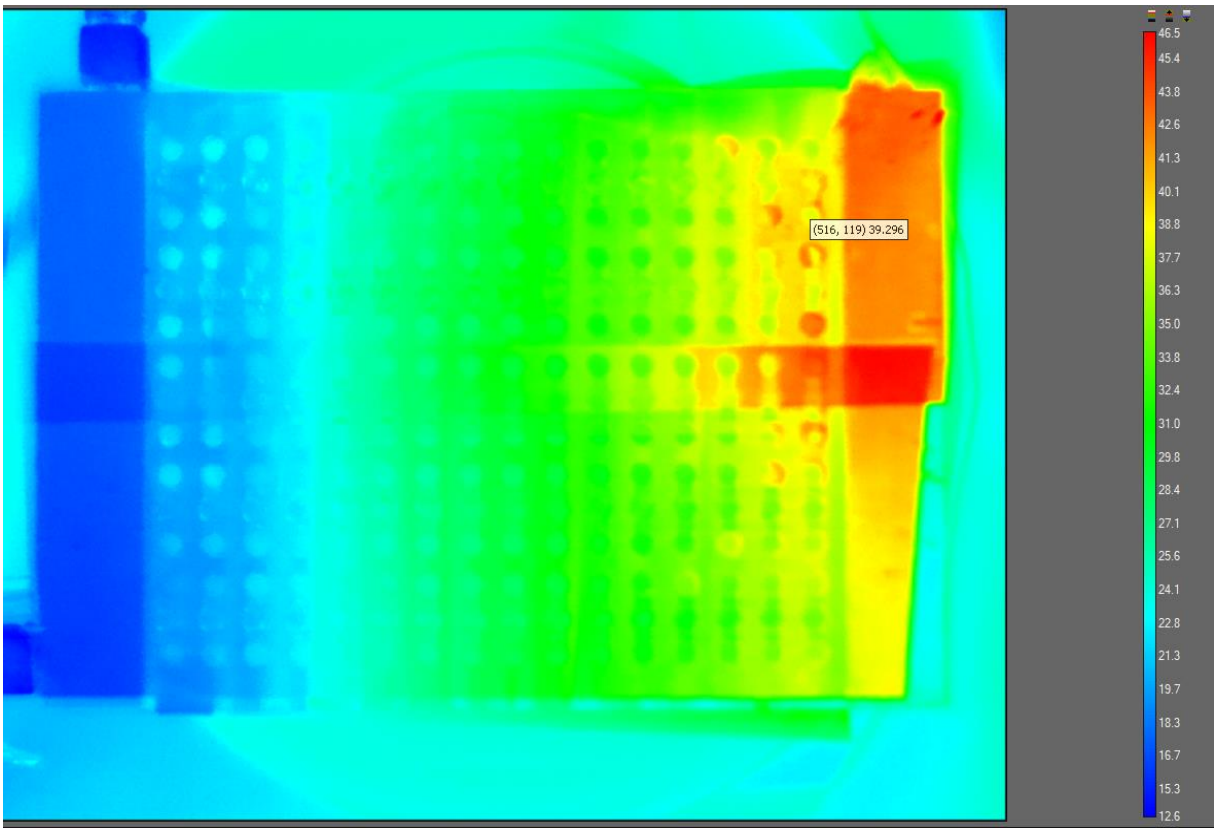

Figure 7.2. Infrared image of the TRHA.

The TRHA's design is shown in Figure 7.1. The TRHA consists of an aluminum block machined to house 80 sample wells and 40 liquid holding wells. Each liquid well is made to provide two sample wells with elevated relative humidity based on the salt solution and temperature within the well. The RH was validated by using reversible humidity test strips (Indigo Instruments, 33813-2080). A temperature gradient is achieved across the length of the TRHA by a Tempco low density cartridge heater (LDC00003) inserted into the metal on one end and chilled water circulated through the opposite end. Figure 7.2 shows the temperature profile of the TRHA when the heat cartridge is set to 50 ºC and the circulated water is chilled to 14 ºC. In this work, every liquid well was filled with a saturated salt solution to achieve a 75% RH at every sample well.

To fill the TRHA with sample, an insert was 3D printed to fit into the sample wells from the top which left ~400 μm of space in the sample well for the powdered sample. The powder was placed onto the bottom of the TRHA and a razor blade was used to spread the powder out to fill each well and clear the metal surface of any residual powder. A plastic cover slip with adhesive on one side was then placed over the bottom of the TRHA and vacuum grease was used around the edges of the cover slip in order to ensure an airtight seal. The insert was then removed, and 10 mL of saturated sodium chloride solution was added into each liquid well. The top of the TRHA was then sealed with a second cover slip and more grease. A 3D printed holder was used inside of a SONICC microscope from Formulatrix (Bedford, MA) to hold the TRHA steady for SHG imaging over 48 hours. A microretarder array was inserted into the beam path before the objective lens in order to increase the depth of field of the microscope. This allowed for fewer planes in the z-scan used to image the sample wells and is discussed in greater detail in a separate manuscript by Ding et. al.[135] Images were collected for each sample well using ~150 mW of excitation laser power at the sample and 890 ms exposure time. Every sample well in the TRHA was imaged every hour (duty cycle of 2.8×10^{-4}) in the transmission direction due to the high RH causing the sample to become transparent after absorbing water. The results from the wells that have the same temperature and humidity wereaveraged together. For this set of experiments, each row is generally the same temperature and has the same humidity aside from the first several rows near the heated end of the TRHA as a side effect of the size of the heat cartridge.

7.3 Results and Discussion

The TRHA was used to determine the crystal growth and nucleation rates of model ritonavir containing ASDs. Figure 7.3 shows preliminary data collected using the TRHA with the elevated conditions being 75% RH and the temperature profile from Figure 7.2. The wells that do not show images were filled with griseofulvin to provide a signal for determining the correct z-plane for imaging in the automated sequence over 48 hours. Initially, as shown in Figure 7.3A, each well shows little signal aside from potential residual crystals within the ASD or contaminants from the sample preparation process. Figure 7.3B shows the rapid crystallization of the API in the wells nearer to the hot side of the TRHA, and 7.3C shows the TRHA after 48 hours at elevated temperature and humidity, where nearly half of the wells within the TRHA show significant crystal nucleation and growth. As is expected, there is qualitatively earlier and quicker crystal nucleation

and growth in the wells with a higher temperature, while the wells with lower temperatures show significantly reduced crystal growth and nucleation. Many wells closer to the cooler side of the TRHA show little difference between images at the initial timepoint versus at 48 hours. The sections of the heated side of the TRHA that show less crystal growth could be due to the heat cartridge being pushed further into the TRHA, resulting in a slightly cooler section. It could also be due to contamination from the griseofulvin used in the wells nearby that tend to be brighter than the signal from the ritonavir crystals. The results Figure 7.3 show are promising for the future work with the TRHA platform since the expected trends can already be seen in preliminary data.

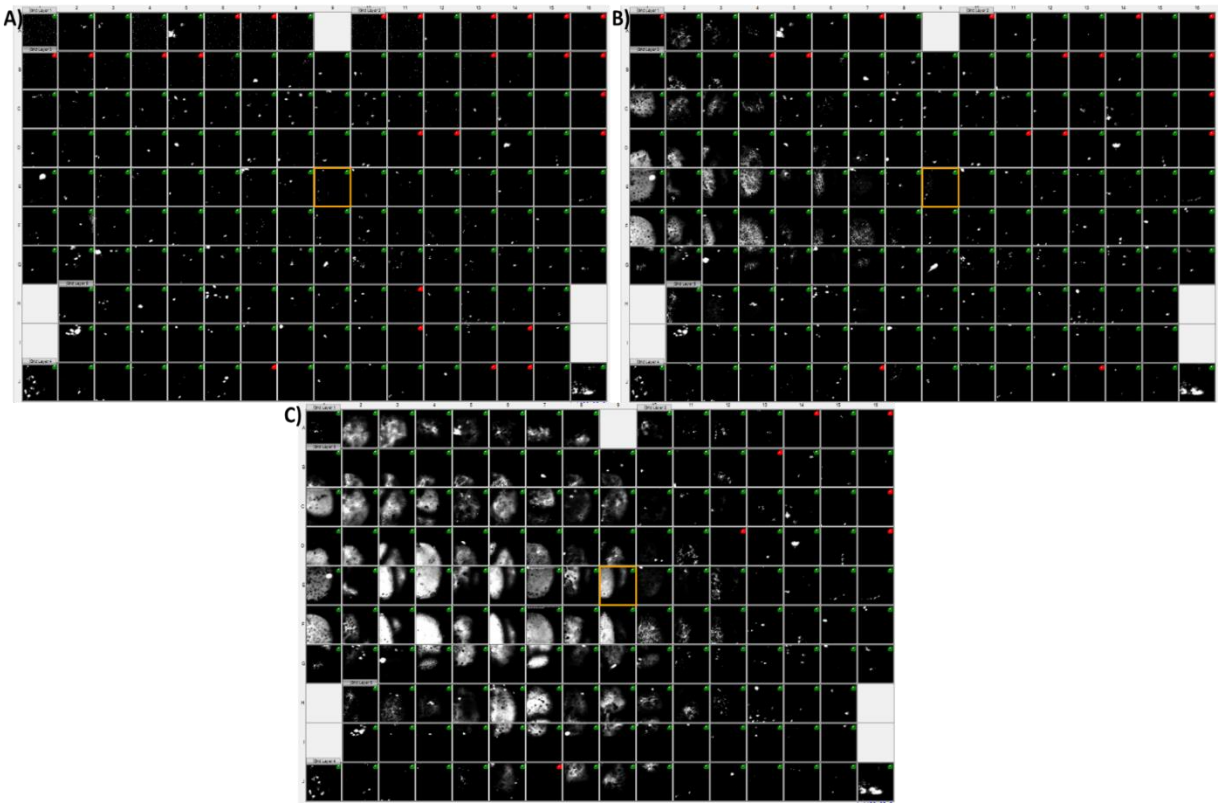

Figure 7.3. Preliminary data collected using the TRHA and model ritonavir containing ASD samples stressed at 75% RH in all wells and using the temperature profile from Figure 7.2. Each image is an extended focus image made by adding multiple z-plane images together. The left side of the images is the hot side and the right is the cool side. The bottom left corner of the images corresponds to the opening where the heat cartridge is inserted into the TRHA. A) Shows the initial time point of the accelerated stability test and the signal observed is expected to be contaminants from sample preparation or residual crystallinity within the ASD. B) Shows the TRHA after 12 hours at elevated conditions. C) Shows the TRHA after 48 hours at elevated conditions.

7.4 Summary

In this work, the TRHA was used to evaluate the temperature dependent effects on crystal growth and nucleation within model ritonavir containing ASDs. The TRHA was filled with the same ASD in order to determine if similar results can be achieved compared to previous studies utilizing the same ritonavir ASD. Preliminary results indicate that similar results are possible at the same temperature and humidity conditions used in the previous studies, and more information content can be generated by using the temperature gradient. Initial results show the expected result of a higher temperature increasing the crystal growth and nucleation rate, while a lower temperature decreases it.

7.5 Future Work

More work is required in optimizing the sample preparation methods. Currently the cover slips used provide complications due to inconsistent thickness throughout the fields of view and overall thickness being too high. New, thinner, and more uniform adhesive films will be used in the future to provide an increase in image quality and a better seal for the individual wells. After the image quality is improved, quantitative analysis will be performed on the images to provide SHG per unit area over time to compare to previous results in order to validate the TRHA methods. With increased image quality, it will also be possible to perform single particle tracking to provide growth and nucleation rates. New samples will also be studied within the TRHA with varying relative humidities to provide an example of the applications that the TRHA can be used for within the pharmaceutical industry.

REFERENCES

[1] J. A. DiMasi, H. G. Grabowski and R. W. Hansen, *Journal of Health Economics* **2016**, *47*, 20-33.

[2] *Aulton's Pharmaceutics: The Design and Manufacture of Medicines*, Churchill Livingstone, **2013**, p.

[3] G. L. Amidon, H. Lennernäs, V. P. Shah and J. R. Crison, *Pharmaceutical Research* **1995**, *12*, 413-420.

[4] S. Baghel, H. Cathcart and N. J. O'Reilly, *Journal of Pharmaceutical Sciences* **2016**, *105*, 2527-2544.

[5] X. Liu and A. Fahr, *Expert opinion on drug delivery.* **2007**, *4*, 403-416.

[6] N. J. Babu and A. Nangia, *Crystal Growth & Design* **2011**, *11*, 2662-2679.

[7] J. W. Steed, *Trends in Pharmacological Sciences* **2013**, *34*, 185-193.

[8] S. Aitipamula, R. Banerjee, A. K. Bansal, K. Biradha, M. L. Cheney, A. R. Choudhury, G. R. Desiraju, A. G. Dikundwar, R. Dubey, N. Duggirala, P. P. Ghogale, S. Ghosh, P. K. Goswami, N. R. Goud, R. R. K. R. Jetti, P. Karpinski, P. Kaushik, D. Kumar, V. Kumar, B. Moulton, A. Mukherjee, G. Mukherjee, A. S. Myerson, V. Puri, A. Ramanan, T. Rajamannar, C. M. Reddy, N. Rodriguez-Hornedo, R. D. Rogers, T. N. G. Row, P. Sanphui, N. Shan, G. Shete, A. Singh, C. Q. C. Sun, J. A. Swift, R. Thaimattam, T. S. Thakur, R. K. Thaper, S. P. Thomas, S. Tothadi, V. R. Vangala, N. Variankaval, P. Vishweshwar, D. R. Weyna and M. J. Zaworotko, *Crystal Growth & Design* **2012**, *12*, 2147-2152.

[9] H. D. Williams, N. L. Trevaskis, S. A. Charman, R. M. Shanker, W. N. Charman, C. W. Pouton and C. J. H. Porter, *Pharmacological Reviews* **2013**, *65*, 315-499.

[10] G. Van den Mooter, M. Wuyts, N. Blaton, R. Busson, P. Grobet, P. Augustijns and R. Kinget, *European Journal of Pharmaceutical Sciences* **2001**, *12*, 261-269.

[11] F. Qian, J. Huang and M. A. Hussain, *Journal of Pharmaceutical Sciences* **2010**, *99*, 2941-2947.

[12] A. A. Ambike, K. R. Mahadik and A. Paradkar, *Pharmaceutical Research* **2005**, *22*, 990-998.

[13] L. Yu, *Advanced Drug Delivery Reviews* **2001**, *48*, 27-42.

[14] P. Gupta, V. K. Kakumanu and A. K. Bansal, *Pharmaceutical Research* **2004**, *21*, 1762-1769.

[15] A. W. Newman and S. R. Byrn, *Drug Discovery Today* **2003**, *8*, 898-905.

[16] M. Yoshioka, B. C. Hancock and G. Zografi, *Journal of Pharmaceutical Sciences* **1995**, *84*, 983-986.

[17] B. Shah, V. K. Kakumanu and A. K. Bansal, *Journal of Pharmaceutical Sciences* **2006**, *95*, 1641-1665.

[18] L. S. Taylor and G. Zografi, *Pharmaceutical Research* **1997**, *14*, 1691-1698.

[19] V. Tantishaiyakul, N. Kaewnopparat and S. Ingkatawornwong, *International Journal of Pharmaceutics* **1999**, *181*, 143-151.

[20] R. K. Harris, *Analyst* **2006**, *131*, 351-373.

[21] A. U. Chowdhury, S. J. Zhang and G. J. Simpson, *Analytical Chemistry* **2016**, *88*, 3853-3863.

[22] A. N. Ghebremeskel, C. Vemavarapu and M. Lodaya, *Pharmaceutical Research* **2006**, *23*, 1928-1936.

[23] D. J. Kissick, D. Wanapun and G. J. Simpson, *Annual Review of Analytical Chemistry, Vol 4* **2011**, *4*, 419-437.

[24] P. D. Schmitt, E. L. DeWalt, X. Y. Dow and G. J. Simpson, *Analytical Chemistry* **2016**, *88*, 5760-5768.

[25] S. J. Toth, J. T. Madden, L. S. Taylor, P. Marsac and G. J. Simpson, *Analytical Chemistry* **2012**, *84*, 5869-5875.

[26] S. J. Toth, P. D. Schmitt, G. R. Snyder, N. S. Trasi, S. Z. Sullivan, I. A. George, L. S. Taylor and G. J. Simpson, *Crystal Growth & Design* **2015**, *15*, 581-586.

[27] J. A. Newman, P. D. Schmitt, S. J. Toth, F. Y. Deng, S. J. Zhang and G. J. Simpson, *Analytical Chemistry* **2015**, *87*, 10950-10955.

[28] D. Wanapun, U. S. Kestur, L. S. Taylor and G. J. Simpson, *Abstracts of Papers of the American Chemical Society* **2011**, *241*.

[29] Z. T. Song, S. Sarkar, A. D. Vogt, G. D. Danzer, C. J. Smith, E. J. Gualtieri and G. J. Simpson, *Analytical Chemistry* **2018**, *90*, 13130-13130.

[30] B. Kommanaboyina and C. T. Rhodes, *Drug Development and Industrial Pharmacy* **1999**, *25*, 857-868.

[31] N. C. Eddingsaas and K. S. Suslick, *Nature* **2006**, *444*, 163-163.

[32] L. M. Sweeting, M. L. Cashel, M. Dott, J. M. Gingerich, J. L. Guido, J. A. Kling, R. F. Pippin, M. M. Rosenblatt, A. M. Rutter and R. A. Spence, *Molecular Crystals and Liquid Crystals* **1992**, *211*, 389-396.

[33] H. Longchambon, *Comptes Rendus Hebdomadaires Des Seances De L Academie Des Sciences* **1922**, *174*, 1633-1634.

[34] C. J. Smith and S. R. Griffin, *Anal. Chem.* **2018**, *90*, 13131.

[35] P. R. R. Byrn SB, Stowell, J.G. , *Solid state chemistry of drugs*, SSCI Inc, West Lafayette, Indiana, **1999**, p.

[36] S. R. Byrn, R. R. Pfeiffer, G. Stephenson, D. J. W. Grant and W. B. Gleason, *Chemistry of Materials* **1994**, *6*, 1148-1158.

[37] Y. He and C. Ho, *Journal of Pharmaceutical Sciences* **2015**, *104*, 3237-3258.

[38] H. Konno and L. S. Taylor, *Journal of Pharmaceutical Sciences* **2006**, *95*, 2692-2705.

[39] G. P. Johari, S. Ram, G. Astl and E. Mayer, *Journal of Non-Crystalline Solids* **1990**, *116*, 282-285.

[40] U. Zimper, J. Aaltonen, C. M. McGoverin, K. C. Gordon, K. Krauel-Goellner and T. Rades, *Pharmaceutics* **2010**, *2*, 30-49.

[41] Z. Y. Yang, K. Nollenberger, J. Albers, J. Moffat, D. Craig and S. Qi, *European Journal of Pharmaceutics and Biopharmaceutics* **2014**, *88*, 897-908.

[42] Y. C. Ng, Z. Y. Yang, W. J. McAuley and S. Qi, *European Journal of Pharmaceutics and Biopharmaceutics* **2013**, *84*, 555-565.

[43] D. J. Berry, C. C. Seaton, W. Clegg, R. W. Harrington, S. J. Coles, P. N. Horton, M. B. Hursthouse, R. Storey, W. Jones, T. Friscic and N. Blagden, *Crystal Growth & Design* **2008**, *8*, 1697-1712.

[44] D. E. Bugay, *Advanced Drug Delivery Reviews* **2001**, *48*, 43-65.

[45] L. S. Taylor and G. Zografi, *Pharmaceutical Research* **1998**, *15*, 755-761.

[46] P. D. Schmitt, N. S. Trasi, L. S. Taylor and G. J. Simpson, *Molecular Pharmaceutics* **2015**, *12*, 2378-2383.

[47] D. T. Reid, C. M. Heyl, R. R. Thomson, R. Trebino, G. Steinmeyer, H. H. Fielding, R. Holzwarth, Z. G. Zhang, P. Del'Haye, T. Sudmeyer, G. Mourou, T. Tajima, D. Faccio, F. J. M. Harren and G. Cerullo, *Journal of Optics* **2016**, *18*.

[48] M. E. Fermann and I. Hartl, *Nature Photonics* **2013**, *7*, 868-874.

[49] M. E. Fermann and I. Hartl, *Ieee Journal of Selected Topics in Quantum Electronics* **2009**, *15*, 191-206.

[50] L. M. Haupert and G. J. Simpson, *Methods* **2011**, *55*, 379-386.

[51] A. R. Selfridge, *Ieee Transactions on Sonics and Ultrasonics* **1985**, *32*, 381-394.

[52] M. A. Repka, S. Bandari, V. Kallakunta, A. Q. Vo, H. McFall, M. Pimparade and A. Bhagurkar, *Melt extrusion with poorly soluble drugs – An integrated review*, **2017**, p.

[53] F. L. Guedes, B. G. de Oliveira, M. Z. Hernandes, C. A. De Simone, F. J. B. Veiga, M. d. C. A. de Lima, I. R. Pitta, S. L. Galdino and P. J. R. Neto, *AAPS PharmSciTech* **2011**, *12*, 401-410.

[54] D. Law, E. A. Schmitt, K. C. Marsh, E. A. Everitt, W. Wang, J. J. Fort, S. L. Krill and Y. Qiu, *Journal of Pharmaceutical Sciences* **2004**, *93*, 563-570.

[55] U. S. Kestur, D. Wanapun, S. J. Toth, L. A. Wegiel, G. J. Simpson and L. S. Taylor, *Journal of Pharmaceutical Sciences* **2012**, *101*, 4201-4213.

[56] Q. Zhu, S. J. Toth, G. J. Simpson, H. Y. Hsu, L. S. Taylor and M. T. Harris, *Journal of Physical Chemistry B* **2013**, *117*, 5393-5393.

[57] E. L. DeWalt, V. J. Begue, J. A. Ronau, S. Z. Sullivan, C. Das and G. J. Simpson, *Acta Crystallographica Section D-Biological Crystallography* **2013**, *69*, 74-81.

[58] E. L. DeWalt, S. Z. Sullivan, P. D. Schmitt, R. D. Muir and G. J. Simpson, *Analytical Chemistry* **2014**, *86*, 8448-8456.

[59] D. Wanapun, U. S. Kestur, D. J. Kissick, G. J. Simpson and L. S. Taylor, *Analytical Chemistry* **2010**, *82*, 5425-5432.

[60] L. M. Sweeting, *Chemistry of Materials* **2001**, *13*, 854-870.

[61] K. O. Meyer, D.; Rossberg, M., *Kristall und Technik* **1970**, *5*, 181-205.

[62] L. M. Haupert, E. L. DeWalt and G. J. Simpson, *Acta Crystallographica Section D-Biological Crystallography* **2012**, *68*, 1513-1521.

[63] Y. Yoshihashi, H. Iijima, E. Yonemochi and K. Terada, *Journal of Thermal Analysis and Calorimetry* **2006**, *85*, 689-692.

[64] T. Govender, S. Stolnik, M. C. Garnett, L. Illum and S. S. Davis, *Journal of Controlled Release* **1999**, *57*, 171-185.

[65] S. R. G. Casey J. Smith, Gregory S. Eakins, Fengyuan Deng, Julia K. White, Satyanarayana Thirunahari, Srividya Ramakrishnan, Atanu Sangupta, Siwei Zhang, Julie Novak, Zhen Liu, Timothy Rhodes, Garth J. Simpson, *Analytical Chemistry* **2018**.

[66] J. I. Zink, G. E. Hardy and J. E. Sutton, *The Journal of Physical Chemistry* **1976**, *80*, 248-249.

[67] D. A. Smith, G. McKenzie, A. C. Jones and T. A. Smith, *Methods Appl Fluoresc* **2017**, *5*, 042001.

[68] N. Wiener, *Extrapolation, Interpolation and Smoothing of Stationary Time Series*, **1949**, p.

[69] W. H. Richardson, *J. Opt. Soc. Am.* **1972**, *62*, 55.

[70] F. N. Madden, K. R. Godfrey and M. J. Chappell, *J. Pharmacokinet. Biopharm.* **1996**, *24*, 283.

[71] S. Vajda, K. R. Godfrey and P. Valko, *J. Pharmacokinet. Biopharm.* **1988**, *16*, 85.

[72] R. Hovorka, M. J. Chappell and P. A. Soons, *Centre for Measurement and Information in Medicine* **1995**, na.

[73] D. Verotta, *J. Pharmacokinet. Biopharm.* **1993**, *21*, 609.

[74] J. Skilling and R. K. Bryan, *Mon. Not. R. Astron. Soc.* **1984**, *211*, 111.

[75] S. Z. Sullivan, P. D. Schmitt, R. D. Muir, E. L. DeWalt and G. J. Simpson, *Analytical Chemistry* **2014**, *86*, 3508-3516.

[76] D. A. Fish, J. G. Walker, A. M. Brinicombe and E. R. Pike, *J. Opt. Soc. Am. A* **1995**, *12*, 58.

[77] J. Li, P. Zhu and Y. Sun, *Phys. Med. Biol.* **2012**, *57*, 2347.

[78] R. H. Hadfield, *Nature Photonics* **2009**, *3*, 696-705.

[79] C. M. Natarajan, M. G. Tanner and R. H. Hadfield, *Supercond. Sci. Technol.* **2012**, *25*, 063001.

[80] D. O'Connor, *Time-Correlated Single Photon Counting*, **2012**, p.

[81] K. B. Chang and B. W. Edwards, *J. Solid State Chem.* **2016**, *236*, 78.

[82] Y. Tsuboi and T. Seto, *J. Phys. Chem. A* **2008**, *112*, 6517.

[83] S. Yuen and M. Schreyer, *Appl. Phys. Lett.* **2006**, *88*, 123901.

[84] A. de Juan, J. Jaumot and R. A. Tauler, *Analytical Methods* **2014**, *6*, 4964-4976.

[85] P. Paatero and U. Tapper, *Environmetrics* **1994**, *5*, 111.

[86] S. H. Wang, T. Xu, Y. H. Yang and Z. Z. Shao, *Acs Applied Materials & Interfaces* **2015**, *7*, 21254-21262.

[87] S. A. Vavasis, *Computing Research Repository* **2007**, abs/0708.4149.

[88] A. Savitzky and M. J. E. Golay, *Anal. Chem.* **1964**, *36*, 1627.

[89] D. J. Kissick, R. D. Muir and G. J. Simpson, *Analytical Chemistry* **2010**, *82*, 10129-10134.

[90] W. W.-S. Wei, *Time series analysis*, Addison-Wesley publ Reading, **1994**, p.

[91] T. N. Piehler, F. C. DeLucia, C. A. Munson, B. E. Homan, A. W. Miziolek and K. L. McNesby, *Applied Optics* **2005**, *44*, 3654-3660.

[92] W. Becker, *Springer Science & Business Media* **2005**, *81*.

[93] M. Kennedy, J. Hu, P. Gao, L. Li, A. Ali-Reynolds, B. Chal, V. Gupta, C. Ma, N. Mahajan, A. Akrami and S. Surapaneni, *Molecular Pharmaceutics* **2008**, *5*, 981-993.

[94] J. P. Lalkshman, Y. Cao, J. Kowalski and A. T. M. Serajuddin, *Molecular Pharmaceutics* **2008**, *5*, 994-1002.

[95] A. T. M. Serajuddin, *Journal of Pharmaceutical Sciences* **1999**, *88*, 1058-1066.

[96] R. O. Williams, A. B. Watts and D. A. Miller, *Formulating Poorly Water Soluble Drugs, 2nd Edition* **2016**, *22*, Vii-Ix.

[97] C. Fang, N. Bhattarai, C. Sun and M. Q. Zhang, *Small* **2009**, *5*, 1637-1641.

[98] T. Neuberger, B. Schopf, H. Hofmann, M. Hofmann and B. von Rechenberg, *Journal of Magnetism and Magnetic Materials* **2005**, *293*, 483-496.

[99] R. A. Carlton, *Pharmaceutical Microscopy* **2011**, 7-64.

[100] J. A. Baird and L. S. Taylor, *Advanced Drug Delivery Reviews* **2012**, *64*, 396-421.

[101] Y. Sun, L. Zhu, T. Wu, T. Cai, E. M. Gunn and L. Yu, *Aaps Journal* **2012**, *14*, 380-388.

[102] L. Li, A. J. Fijneman, J. A. Kaandorp, J. Aizenberg and W. L. Noorduin, *Proceedings of the National Academy of Sciences of the United States of America* **2018**, *115*, 3575-3580.

[103] A. U. Chowdhury, D. H. Ye, Z. T. Song, S. J. Zhang, H. G. Hedderich, B. Mallick, S. Thirunahari, S. Ramakrishnan, A. Sengupta, E. J. Gualtieri, C. A. Bouman and G. J. Simpson, *Analytical Chemistry* **2017**, *89*, 5959-5966.

[104] C. J. Smith, J. Dinh, P. D. Schmitt, P. A. Stroud, J. Hinds, M. J. Johnson and G. J. Simpson, *Applied Spectroscopy* **2018**, *72*, 1594-1605.

[105] P. Mistry, K. K. Amponsah-Efah and R. Suryanarayanan, *Crystal Growth & Design* **2017**, *17*, 2478-2485.

[106] D. E. Moseson, N. A. Mugheirbi, A. A. Stewart and L. S. Taylor, *Crystal Growth & Design* **2018**, *18*, 7633-7640.

[107] I. Ivanisevic, *Journal of Pharmaceutical Sciences* **2010**, *99*, 4005-4012.

[108] J. Schmelzer, R. Pascova, J. Möller and I. Gutzow, *Journal of Non-Crystalline Solids* **1993**, *162*, 26-39.

[109] H. Tanaka, *Physical Review E* **2003**, *68*, 011505.

[110] T. Wu, Y. Sun, N. Li, M. M. de Villiers and L. Yu, *Langmuir* **2007**, *23*, 5148-5153.

[111] T. Wu and L. Yu, *Pharmaceutical Research* **2006**, *23*, 2350-2355.

[112] O. E. Farrance, R. A. L. Jones and J. K. Hobbs, *Polymer* **2009**, *50*, 3730-3738.

[113] Q. Shi, C. Zhang, Y. Su, J. Zhang, D. Zhou and T. Cai, *Molecular Pharmaceutics* **2017**, *14*, 2262-2272.

[114] T. Cai, L. Zhu and L. Yu, *Pharmaceutical Research* **2011**, *28*, 2458-2466.

[115] L. Zhu, J. Jona, K. Nagapudi and T. Wu, *Pharmaceutical Research* **2010**, *27*, 1558-1567.

[116] S.-W. Zhang, L. Yu, J. Huang, M. A. Hussain, L. Derdour, F. Qian and M. M. de Villiers, *AAPS PharmSciTech* **2014**, *15*, 1516-1526.

[117] A. A. Bunaciu, E. G. Udristioiu and H. Y. Aboul-Enein, *Critical Reviews in Analytical Chemistry* **2015**, *45*, 289-299.

[118] H. Chauhan, C. Hui-Gu and E. Atef, *Journal of Pharmaceutical Sciences* **2013**, *102*, 1924-1935.

[119] T. Otaki, Y. Tanabe, T. Kojima, M. Miura, Y. Ikeda, T. Koide and T. Fukami, *International Journal of Pharmaceutics* **2018**, *542*, 56-65.

[120] W. Sinclair, M. Leane, G. Clarke, A. Dennis, M. Tobyn and P. Timmins, *Journal of Pharmaceutical Sciences* **2011**, *100*, 4687-4699.

[121] S. Bhatia, A. Khanna, R. K. Jain and Hirdesh, *Materials Research Express* **2019**, *6*, 086409.

[122] L. Zhao, A. C. Pinon, L. Emsley and A. J. Rossini, *Magnetic Resonance in Chemistry* **2018**, *56*, 583-609.

[123] N. K. Thakral, S. Mohapatra, G. A. Stephenson and R. Suryanarayanan, *Molecular Pharmaceutics* **2015**, *12*, 253-263.

[124] K. r. Bērziņš and R. Suryanarayanan, *Crystal Growth & Design* **2018**, *18*, 839-848.

[125] C. J. Strachan, M. Windbergs and H. L. Offerhaus, *International Journal of Pharmaceutics* **2011**, *417*, 163-172.

[126] C. B. Rawle, C. J. Lee, C. J. Strachan, K. Payne, P. J. Manson and T. Rades, *Journal of Pharmaceutical Sciences* **2006**, *95*, 761-768.

[127] V. Podzemná, J. Barták and J. Málek, *Journal of Thermal Analysis and Calorimetry* **2014**, *118*, 775-781.

[128] S. Sarkar, Z. Song, S. R. Griffin, N. Takanti, A. D. Vogt, A. Ruggles, G. D. Danzer and G. J. Simpson, *Molecular Pharmaceutics* **2020**, *17*, 769-776.

[129] J. Raudonus, J. Bernard, H. Janßen, J. Kowalczyk and R. Carle, *Food Research International* **2000**, *33*, 41-51.

[130] H. Konno and L. S. Taylor, *Pharmaceutical Research* **2008**, *25*, 969-978.

[131] S. L. Shamblin and G. Zografi, *Pharmaceutical Research* **1999**, *16*, 1119-1124.

[132] D. Ben-Amotz, *Self Published* **2019**.

[133] D. R. Olander, *Industrial & Engineering Chemistry Fundamentals* **1967**, *6*, 178-188.

[134] G. Van den Mooter, *Drug Discovery Today: Technologies* **2012**, *9*, 79-85.

[135] C. L. Changqin Ding, Fengyuan Deng, and Garth J. Simpson, *Optics Express* **2019**, *27*, 3837-3850.

VITA

Scott Griffin was born in Fredericksburg, Virginia in 1992. He attended Stafford High School and garnered a love for science from his teachers there. He later attended Bridgewater College and graduate with a dual degree B.S. in Chemistry and Physics. During his last two years at Bridgewater he accepted an internship at Naval Surface Warfare Center Indian Head where he gained a passion for research. He accepted an offer for the Ph.D. chemistry program at Purdue University and was accepted into Garth Simpson's research group for nonlinear optics. Scott graduated with his Ph.D. in Analytical Chemistry from Purdue University in May 2020.